Identification of aerodynamic coefficients from free flight data

Marie Albisser

Ecole doctorale IAEM Lorraine

Identification of aerodynamic coefficients from free flight data

Identification de coefficients aérodynamiques à partir de données de vol libre

Thèse présentée et soutenue publiquement le 10 juillet 2015 pour l'obtention du

Doctorat de l'Université de Lorraine

Mention Automatique, Traitement du Signal et des Images, Génie Informatique

par

Marie Albisser

Composition du jury

Président:	Edouard LAROCHE	Professeur - Université de Strasbourg
Rapporteurs:	Franck CAZAURANG	Professeur - Université de Bordeaux
	Guillaume MERCERE	Maître de Conférences HdR - Université de Poitiers
Examinateur:	Lionel MARRAFFA	Directeur de recherche - Agence Spatiale Européenne
Directeurs:	Hugues GARNIER	Professeur - Université de Lorraine
	Claude BERNER	Directeur de recherche - Institut franco-allemand de recherches de Saint-Louis
Co-directeurs:	Magalie THOMASSIN	Maître de Conférences - Université de Lorraine
	Simona DOBRE	Chargée de recherche - Institut franco-allemand de recherches de Saint-Louis

Centre de Recherche en Automatique de Nancy
UMR 7039 Université de Lorraine - CNRS
2 rue Jean Lamour, F-54519 Vandoeuvre-les-Nancy, France

Remerciements

Les remerciements ne sont jamais chose facile, au risque de ne pouvoir réellement mettre en évidence l'importance de chacun dans ce qui a donné lieu à ce mémoire. Tout d'abord, mes sincères remerciements s'adressent aux membres de mon jury de thèse, qui m'ont fait l'honneur de participer à l'évaluation de ce travail. Guillaume Mercère et Franck Cazaurang pour leur implication en tant que rapporteurs, ainsi que Lionel Marraffa et Edouard Laroche pour avoir assuré la tâche d'examinateurs. Merci pour vos remarques constructives et le temps que vous avez consacré à ce projet.

Je tiens à remercier mes encadrants de l'ISL et du CRAN, Claude Berner, Simona Dobre, Magalie Thomassin et Hugues Garnier, pour l'intérêt qu'ils ont porté à ce travail. Il est essentiel de constituer une équipe complémentaire pour mener à bien tout projet et ces quelques années de collaboration avec vous m'ont réellement permis de me construire professionnellement. J'adresse un merci tout particulier à Simona et Claude pour leur disponibilité, malgré les imprévus, et leurs conseils avisés.

Quand on débute une thèse, on sait toujours ce que l'on cherche mais jamais réellement ce que l'on va trouver. Je peux affirmer avec certitude, des personnes d'exception.

Je souhaite remercier l'ensemble du groupe ABX, pour leur bonne humeur, les délicieuses odeurs de tartes au petit matin et leur gentillesse dès mes premiers jours au sein de l'équipe.

Merci à la petite bande de l'ISL (les actuels et anciens acolytes), pour les discussions improbables du midi, l'humour plus ou moins compréhensible, les perles du net qui nous font toujours esquisser un sourire... Dédicace spéciale à Vincent, avec qui le covoiturage est proposé avec l'option karaoké.

L'annonce d'un séjour en Lorraine n'a pas été accueillie avec joie. Finalement, ce n'est pas le lieu mais les gens qu'on y rencontre qui font la différence. Un grand merci aux "bibis" du CRAN, Christelle, Sam, Vinz, Mag, Hadi, JB, Julien, Simon, ... pour m'avoir intégré dans votre tribu dès mon arrivée, les pauses chokys et phi, les soirées nancéennes, votre franc parler, et surtout, pour m'avoir permis de me sentir comme chez moi ...

Enfin, ces derniers mots de remerciements sont destinés à ceux qui, aussi éloignés de mon monde professionnel soient-ils, ont toujours su être d'un soutien sans faille : la bande d'Hirtzbach, pour toutes ces soirées animées qui m'ont permis de décompresser; les nunus, pour leur amitié et présence depuis toutes ces années; Thibaut, pour cette belle complicité depuis la première année de fac, et qui le dit si bien, a su être d'un "soutien incommensurable".

Tout ça n'aurait pu être possible, ni même envisagé, sans mes parents qui ont été et qui restent des piliers et des supporters sans limite. Enfin, même si les choses ni ne se disent ni ne s'écrivent entre nous, le moment est bien choisi pour souligner l'importance de l'oreille attentive qu'elle a su être, ma *twin* Mylène, dont l'avis m'a toujours guidé dans mes décisions (sauf en sciences).
La gratitude ne s'écrit pas mais se prouve au quotidien, alors à toutes ces personnes, je vous dis à très vite ...

Contents

Notations

ABBREVIATIONS & ACRONYMS

DOF	Degrees Of Freedom
CFD	Computational Fluid Dynamics
ARFDAS	Aeroballistic Research Facility Data Analysis System
CADRA	Comprehensive Automated Data Reduction and Analysis
c.g.	center of gravity
w.r.t.	with respect to

MATHEMATICS, MODELLING & IDENTIFICATION

a	variable
$\mathbf{a}$	vector
$\mathbf{A}$	matrix
$\mathbf{T}^{A\bar{A}}$	transformation matrix from frame $\bar{A}$ to frame A
$\mathcal{M}$	model structure
t	time variable
$\mathbf{x}$	state vector
$\mathbf{x}_0$	initial value of the state vector
$\mathbf{y}$	output vector
$\mathbf{u}$	input signal vector
$\mathbf{p}_a$	aerodynamic coefficient parameter vector/ model parameter vector
$\mathbf{p} = [\mathbf{x}_0, \mathbf{p}_a]$	parameter vector
$\mathbf{p}^*$	true value of parameter vector
$\mathbf{p}_1$	*a priori* identifiable parameter vector
$\mathbf{p}_2$	*a posteriori* identifiable parameter vector
N	number of measurement times
n_x	number of state variables
n_y	number of outputs
n_p	number of parameters
n_s	number of selected free flight test cases
$\mathbb{R}$	set of real numbers
$\mathbb{P}$	set of *a priori* admissible parameters
$\mathbb{T}$	set of measurement times

REFERENCE FRAMES

$\cdot_E$	Earth axes O_{x_E,y_E,z_E}
$\cdot_B$	body axes $O_{x,y,z}$
$\cdot_W$	wind axes O_{x_W,y_W,z_W}

PHYSICAL QUANTITIES & VARIABLES

$\mathbf{F}$	applied forces vector	
$F_{\cdot}$	applied force	(N)
$\mathbf{M}$	applied moment vector about the c.g.	
$M_{\cdot}$	applied moment about the c.g.	(N.m)
g	gravity	(9.8066 m/s^2)
ρ	air density	(kg/m^3)
$\bar{q}$	dynamic pressure	(N/m^3)
a	speed of sound	(m/s)
m	vehicle mass	(kg)
d	vehicle diameter/ projectile caliber	(m)
L	vehicle length	(m)
S	surface reference area	(m^2)
δ	fin cant angle	(deg)
X_{cg}	c.g. position on the x body axis *w.r.t.* the vehicle nose	(m)
$\mathbf{I}$	inertia matrix	
I_x	longitudinal moment of inertia	(kg.m^2)
I_y, I_z	transversal moment of inertia	(kg.m^2)
$\mathbf{V}$	translational velocity vector	
V	translational velocity	(m/s)
v_x	translational velocity about x body axis	(m/s)
v_y	translational velocity about y body axis	(m/s)
v_z	translational velocity about z body axis	(m/s)
M	Mach number	
α	angle of attack	(deg)
β	angle of sideslip	(deg)
α_t	total angle of attack	(deg)
$\boldsymbol{\omega}$	angular velocity vector	
ω_x	roll rate/ spin rate	(deg/s)
ω_y	pitch rate	(deg/s)
ω_z	yaw rate	(deg/s)
ϕ	roll angle	(deg)
θ	pitch angle	(deg)
ψ	yaw angle	(deg)
x_E	x component of the c.g. position *w.r.t.* the Earth frame	(m)
y_E	y component of the c.g. position *w.r.t.* the Earth frame	(m)
z_E	z component of the c.g. position *w.r.t.* the Earth frame	(m)
$M0$	initial launch Mach number	
$\alpha 0$	initial angle of attack	(deg)

AERODYNAMIC COEFFICIENTS $\mathbf{C}(\mathbf{x}(t), \mathbf{p_a})$ (no dimension)

C_X	axial force coefficient	(body frame)
C_Y	sideforce coefficient	(body frame)
$C_N = -C_Z$	normal force coefficient	(body frame)
C_D	drag coefficient	(wind frame)
C_{Yw}	sideforce coefficient	(wind frame)
C_L	lift coefficient	(wind frame)
$C_{L\alpha}$	lift coefficient slope	
$C_{yp\alpha}$	Magnus force coefficient slope	
C_l, C_m, C_n	roll, pitch, yaw moment coefficients	
C_{lp}	roll damping coefficient	
$C_{l\delta}$	roll moment coefficient due to fin cant	
$C_{m\alpha}$	pitch moment coefficient slope or overturning coefficient	
$C_{n\beta}$	yaw moment coefficient slope	
C_{mq}	pitch damping coefficient	
C_{nr}	yaw damping coefficient	
$C_{np\alpha}$	Magnus moment coefficient slope	

Conferences and publications

The main studies perform during the thesis and detailed in this report were submitted and presented at several international congresses and had led to the following publications:

Article in international peer-reviewed journal

Albisser, M., Dobre, S., Berner, C., Thomassin, M. and Garnier, H., Identification of aerodynamic coefficients of a re-entry space vehicle from multiple free flight tests. *AIAA Journal of Spacecraft and Rockets*, 2015, *to be submitted.*

Papers in international peer-reviewed conferences with proceedings

Albisser, M., Dobre, S., Berner, C., Thomassin, M. and Garnier, H., "Identifiability investigation of the aerodynamic coefficients from free flight tests", *AIAA Atmospheric Flight Mechanics Conference, Boston, Massachusetts*, 2013.

Albisser, M., Dobre, S., Berner, C., Thomassin, M. and Garnier, H., "Grey-box identification of the aerodynamic coefficients from free flight tests", *13th ECC European Control Conference, Strasbourg, France*, 2014.

Albisser, M., Berner, C., Dobre, S., Thomassin, M. and Garnier, H., "Aerodynamic coefficients identification procedure of a finned projectile using magnetometers and videos free flight data", *28th ISB International Symposium on Ballistics, Atlanta, Georgia*, 2014.

Dobre, S., Berner, C., **Albisser, M.** and Saada, F., "MarcoPolo-R ERC Dynamic Stability Characterization. Open Range Free Flight Tests", *8th European Symposium on Aerothermodynamics for Space Vehicles, Lisbon, Portugal*, 2015.

Oral presentations in international conferences (without proceedings)

Albisser, M., Dobre, S., Berner, C., Thomassin, M. and Garnier, H., "Identifiability investigation of the aerodynamic coefficients from free flight tests", *ERNSI, Workshop of the European Research Network on System Identification, Nancy, France*, 2013.

Albisser, M., Berner, C. and Dobre, S., "Aerodynamic Coefficient Identification Procedure of a Reference Finned Projectile", *ISL Scientific Symposium, Saint-Louis, France*, 2015.

Oral presentation in a national workshop (without proceedings)

Albisser, M., Dobre, S., Berner, C., Thomassin, M. and Garnier, H., "Aerodynamic parameter identification of vehicles in free flight", *Identification Workshop, Paris, France*, 2014.

Introduction

Tout mettre en œuvre pour atteindre un objectif, dans tous les sens du terme. Parvenir à un but précis, un projectile qui touche une cible, une sonde spatiale mise en orbite ou qui atterrit sur une surface désirée, par exemple une planète, pour étudier un nouvel environnement en est le dénouement souhaité. Cette finalité est dépendante de l'objet lancé et ainsi, la connaissance du comportement en vol de ce dernier reste indispensable à cette réussite. Ce projet aspire, à travers l'identification des coefficients aérodynamiques, à déterminer les caractéristiques aérodynamiques d'un véhicule en vol qu'il soit, un corps de rentrée dans l'atmosphère, un drone ou une munition. L'estimation de ces paramètres est basée sur des données mesurées en vol libre au moyen de différentes techniques de mesure. Ce sujet de recherche a été proposé par l'Institut franco allemand de recherches de Saint-Louis (ISL), plus particulièrement, par le groupe d'Aérodynamique et de Balistique eXtérieure (ABX), s'associant le concours d'un laboratoire universitaire spécialisé dans le domaine de l'identification qu'est le Centre de Recherche en Automatique de Nancy (CRAN). Ainsi, la collaboration avec l'équipe-projet *iModel* du département *CID* (Contrôle, Identification et Diagnostic) traitant l'identification et la modélisation de systèmes dynamiques, a créé une complémentarité des compétences avec les aptitudes de l'ISL.

La *balistique* est la science qui a pour objet d'étudier l'ensemble des phénomènes auxquels est soumis un projectile, du départ du coup jusqu'à la fin de son interaction avec une cible. Elle peut être divisée en 4 catégories : intérieure, intermédiaire, extérieure et terminale [Dorrzapft (2010)] :

- la *balistique intérieure* est dédiée aux études des phénomènes se produisant à l'intérieur du canon, dans le but par exemple, d'améliorer l'efficacité des systèmes de lancement ;
- la *balistique intermédiaire* concerne l'étude des phénomènes liés entre autres aux interactions externes sur l'objet en sortie du canon telles que les gaz de combustion, le saut aérodynamique ou les interférences produites par les sabots maintenant l'objet dans le lanceur. Ce domaine est souvent fusionné avec celui de la balistique extérieure ;
- la *balistique extérieure* est la phase comprise entre le moment où l'objet en vol n'est plus perturbé par les turbulences de la bouche du canon et/ou par les interactions externes comme la séparation des sabots jusqu'à l'impact ;
- en dernier lieu, la *balistique terminale* traite des études liées à l'interaction de l'objet avec la cible.

La présente étude s'inscrit dans le cadre de la balistique extérieure. En fonction des forces agissant sur le véhicule, deux branches de la balistique extérieure se distinguent. D'une part, la *balis-*

tique du vide qui ne considère que la force gravitationnelle comme force agissant sur le véhicule. D'autre part, la *balistique dans le milieu atmosphérique* qui étudie l'attitude en vol caractérisée par l'ensemble des forces et moments qui s'appliquent sur le véhicule. Ces derniers sont directement reliés aux coefficients aérodynamiques. Ils représentent une contribution essentielle à la modélisation de nombreux phénomènes et englobent principalement les aspects de résistance, de portance, mais également de stabilité. Deux types de stabilité peuvent être définis et suscitent un grand nombre d'études, particulièrement en aérodynamique, où on distingue la stabilité statique et la stabilité dynamique. La *stabilité statique* décrit la capacité d'un objet à retrouver sa position d'équilibre après en avoir été écartée alors que la *stabilité dynamique* considère la tendance du mouvement pour retrouver une position d'équilibre.

En balistique extérieure, l'utilisation des coefficients aérodynamiques pour caractériser le comportement d'un objet en vol demeure un sujet de recherche parmi les plus complexes et les plus étudiés. Durant ces dernières décennies, les avancées techniques ont mené au développement de méthodes expérimentales et théoriques permettant de quantifier les propriétés aérodynamiques. Plusieurs outils existent et peuvent être utilisés, à savoir :

- les codes numériques ;
- les essais en soufflerie ;
- les essais en champ de tir.

Chaque technique présente des avantages et inconvénients mais elles peuvent être employées de façon complémentaire, sous forme d'exploration triangulaire, comme présentée dans la Figure 1.

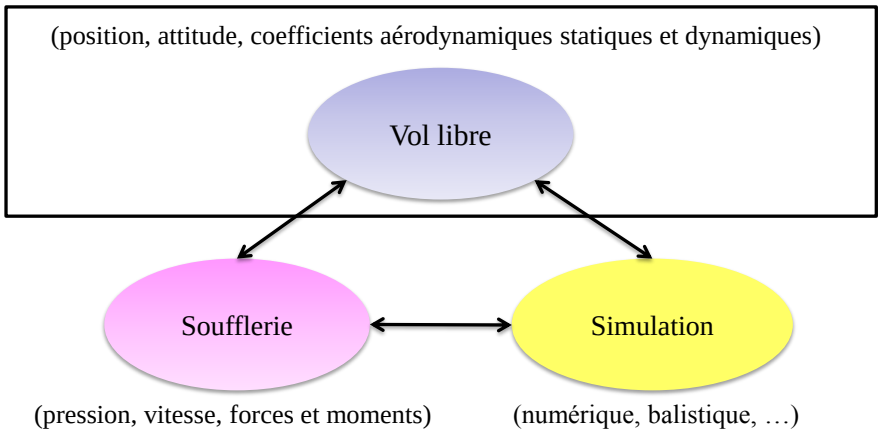

Figure 1: Différentes possibilités pour quantifier les coefficients aérodynamiques

Les outils empiriques et/ou semi-empiriques, tels que PRODAS (PROjectile Design/Analysis System), Missile Datcom ou AeroPrediction, sont des codes généralement adaptés et utilisés dans le cadre d'avant-projet, utile par exemple pour la définition et l'optimisation d'un nouveau concept ou d'une nouvelle architecture. Il faut noter que ces codes s'appuient sur des modèles théoriques et/ou sur des bases de données aérodynamiques, obtenues à partir de résultats de simulation numérique, d'essais en soufflerie ou en tunnel de tir. Ils ont l'avantage d'être applicables à un large éventail

de configurations et permettent d'obtenir rapidement des résultats. Cependant, la détermination des propriétés aérodynamiques à partir de ces codes est dépendante de la qualité de la base de données répertoriée. Afin d'obtenir des estimations suffisamment précises, la configuration étudiée doit être proche de celle qui a permis de peupler la base de données.
La simulation numérique, au moyen de codes de calcul CFD (Computational Fluid Dynamics), permet la prédiction et la compréhension de la structure tridimensionnelle des écoulements autour d'une configuration, par la résolution numérique des équations fondamentales de la dynamique des fluides. Des codes tels que CFX ou Fluent s'appuient sur la résolution des équations de Navier-Stokes et demeurent des outils très puissants. La détermination des coefficients peut être menée sous forme paramétrique pour des nombres de Mach et des incidences fixés. Cependant, les simulations requises pour couvrir l'ensemble de la plage de variation représentative du vol peuvent être très coûteuses en termes de temps de calcul. D'autre part, certains phénomènes, tels que l'amortissement en tangage et/ou en lacet, restent particulièrement complexes à déterminer, en utilisant des prédictions CFD.

Les essais en soufflerie permettent d'effectuer des mesures en maintenant l'objet à étudier dans une veine d'essai au moyen d'un support. L'avantage principal est de pouvoir facilement étudier différents nombres de Mach et incidences par simple déplacement de l'objet au moyen d'un système de mise en incidence. Les essais en soufflerie sont utilisés, par exemple, pour la visualisation de la structure des écoulements, du champ des vitesses, de la distribution des pressions ainsi que des forces et moments pour la détermination des coefficients de stabilité statique. L'inconvénient majeur de cet outil est essentiellement lié à l'interaction entre l'écoulement et le dard permettant de maintenir la maquette, ce qui peut fausser la détermination exacte de certains coefficients. D'autre part, la détermination des coefficients de stabilité dynamique est très limitée par la faible variation des oscillations libres ou forcées de l'objet dans la veine.

La dernière technique de quantification de coefficients aérodynamiques consiste à les déterminer à partir de données de vol libre obtenues lors d'essais en champ de tir. Ces essais permettent d'étudier le comportement en vol dans des conditions expérimentales réelles. Les caractéristiques aérodynamiques n'étant généralement pas directement mesurées, elles sont déterminées à partir de grandeurs mesurées durant le vol au moyen de différentes techniques de mesure. Néanmoins, la précision de leur détermination est souvent influencée par l'expertise et l'appréciation du chercheur en charge du traitement des données.
Les essais en vol libre peuvent être considérés comme référence et sont incontournables pour l'étude du comportement d'un objet en vol et la détermination des coefficients aérodynamiques. La possibilité d'identifier les propriétés aérodynamiques reste tributaire des moyens de mesure disponibles. L'ISL possède de nombreuses compétences en aérodynamique qui s'étendent à la réalisation de prototypes et d'instrumentations permettant les mesures en vol. De plus, l'institut possède son propre champ de tir où des tests en vol libre peuvent être réalisés. Ainsi, l'infrastructure et les techniques disponibles ont permis de mener les travaux liés à ce projet de thèse, qui traite de l'identification des coefficients aérodynamiques à partir de données de vol libre.

Deux cas d'application ont été traités pendant ces travaux de recherche : un corps de rentrée dans l'atmosphère et un projectile stabilisé par empennage. Ce choix, d'analyser deux architectures différentes, est justifié par leurs comportements très distincts en vol.

La première application concerne l'étude d'un corps de rentrée dans l'atmosphère qui s'inscrit dans un programme proposé par l'Agence Spatiale Européenne (ESA) à destination de la planète Mars dont la vocation principale est l'étude de l'environnement martien, son atmosphère et la composition de son sol. La rentrée atmosphérique est une phase délicate et essentielle et par conséquent nécessite une très bonne connaissance du comportement en vol de la sonde, plus particulièrement pendant la phase de descente et d'atterrissage sur Mars. Lors de la descente, la capsule doit être conçue pour ralentir rapidement, de la vitesse hypersonique à quelques centaines de mètres par seconde. Durant la phase de décélération, des études [Sammonds (1970), Winchenbach et al. (2002)] ont démontré que les corps de rentrée dans l'atmosphère sont fréquemment dynamiquement instables pour des nombres de Mach inférieurs à 2,4 et pour des incidences inférieures à 6 degrés. Le cas échéant, des effets indésirables peuvent se manifester, tels que des mouvements de "tumbling" [1] ou des oscillations angulaires trop élevées. Si ces mouvements sont trop importants, cela peut avoir de graves conséquences sur les effets terminaux, comme par exemple le processus de déploiement du parachute ou des angles d'impacts beaucoup trop grands, qui pourraient nuire au succès de la mission. Par conséquent, ces phénomènes peuvent être évités par l'optimisation de la géométrie du corps et par un positionnent correct de son centre de gravité. Des essais en vol libre avec des modèles à échelle réduite ont d'ores et déjà fait leurs preuves, comme étant une méthode efficace pour déterminer les caractéristiques de stabilité dynamique [Schoenenberger et al. (2005)], sous condition de respecter et de tenir compte des effets d'échelle de certains paramètres.
Quant au comportement en vol du projectile stabilisé par empennage, nommé Basic Finner, il a déjà fait l'objet de nombreuses études, menées notamment par le Centre de Recherche et Développement pour la Défense Canada (RDDC) de Valcartier, en vol libre et en soufflerie [Dupuis and Hathaway (1997), Dupuis (2002)]. Des résultats issus de codes de prédictions aérodynamiques tels que PRODAS, Missile Datcom ou AeroPrediction [Shantz and Groves (1960), Dunn (1989), Dupuis (2002), Bhagwandin and Sahu (2013)] ont mené à des conclusions bien établies, particulièrement en termes de stabilité. Statiquement et dynamiquement stable, l'étude de ce projectile vise à comparer et à valider nos résultats et les techniques d'identification utilisées dans le cadre de cette thèse.

Dans la littérature, le sujet de l'identification de systèmes aéronautiques est largement exploré, particulièrement en avionique. Dans ce domaine, l'identification des coefficients aérodynamiques à partir de données en vol a été réalisée avec succès par l'intermède de modèles physiques [Jategaonkar (2006), Klein and Morelli (2006)]. Cependant, pour les applications balistiques, la détermination des coefficients aérodynamiques à partir de mesures en vol libre et des techniques d'identification de systèmes demeure une tâche complexe et ambitieuse. Ceci est particulièrement dû à la structure non linéaire du modèle mathématique décrivant le comportement de l'objet en vol, l'absence de signal d'entrée, les conditions initiales des variables d'état inconnues [2], la dépendance non linéaire des coefficients aérodynamiques en plusieurs variables d'état ou encore les contraintes imposées par les conditions expérimentales. Dans ces conditions, l'estimation de paramètres doit être menée avec rigueur. De plus, la nuance réside dans le comportement en vol caractérisé par des degrés de liberté [3] bien plus variables. Ainsi, une linéarisation des équations d'état autour de points de

1. Le mouvement de "tumbling", de l'anglais *to tumble* signifiant "culbuter", est un phénomène typique des pendulaires qui caractérise un mouvement de bascule de l'objet.

2. Dans le cadre de la balistique extérieure, le temps initial considéré pour le vol libre est différent du temps initial du tir, c'est pourquoi les conditions initiales des variables d'état sont inconnues et doivent être estimées.

3. Les degrés de liberté, nommés en anglais "Degrees Of Freedom" (DOF), expriment la possibilité de mouvement dans l'espace.

fonctionnement ne peut être envisagée comme dans le cas de l'aéronautique.
En raison de la complexité du problème, l'ensemble des connaissances *a priori* du système et de son fonctionnement représente une source d'informations essentielle. Ces connaissances peuvent être issues de la littérature, des résultats de soufflerie, des prédictions CFD et/ou des codes semi-empiriques. Dans ce sens, dû à l'importance d'intégrer des connaissances *a priori* du système et d'avoir une interprétation physique des coefficients aérodynamiques déterminés à partir de données expérimentales, l'utilisation d'un modèle boîte grise est retenue.

L'identification d'un modèle boîte grise d'un véhicule en vol libre peut être définie comme la détermination d'une structure de modèle et l'estimation des paramètres inconnus contenus dans le modèle sélectionné, en intégrant des connaissances *a priori* à différents niveaux de la procédure d'identification [Bohlin (2006)]. Nous sommes confrontés à un problème inverse qui, dû à la complexité du système et aux contraintes imposées par les mesures d'entrées/sorties, peut être impossible à résoudre s'il est mal posé ou difficile à résoudre s'il est mal conditionné [Hadamard (1902)]. Ces deux problèmes inverses - choix de la structure du modèle et estimation de paramètres - correspondent respectivement à deux concepts distincts : la discernabilité et l'identifiabilité. La structure globale du modèle considéré est fixée à partir des principes de la Physique. Néanmoins, une description des coefficients aérodynamiques, judicieusement sélectionnée et adaptée à chaque application traitée, est à intégrer au modèle. Le problème est ainsi réduit à une procédure d'identification des paramètres décrivant les coefficients aérodynamiques.

Ce projet vise à modéliser et développer des techniques d'identification de paramètres les plus adaptées au problème qu'est la détermination des coefficients aérodynamiques à partir de données de vol libre. L'approche du problème est proposée à travers une "fusion" des notions d'aérodynamique et des techniques d'identification, peu explorée mais abordée dans le cas de corps de rentrée [Vitale and Corraro (2012), de Divitiis and Vitale (2010)]. L'objectif est donc une juste conciliation adaptée au contexte expérimental et aux outils et méthodes d'identification spécifiques à ce problème. Le travail de thèse a permis de développer une procédure d'identification adaptée à ce cas d'étude, composée de plusieurs étapes :

- développer un modèle d'état non linéaire à temps continu caractérisant le comportement d'un véhicule en vol libre, par intégration d'une description complète des coefficients aérodynamiques sous forme polynomiale en fonction du nombre de Mach et de l'incidence ;
- évaluer la faisabilité de l'estimation à travers des études d'identifiabilité *a priori* et *a posteriori* des coefficients aérodynamiques et conditions initiales à déterminer ;
- améliorer les résultats d'estimation en considérant le problème à travers une stratégie "multiple fit". Cette approche permet d'estimer les coefficients aérodynamiques à partir de plusieurs séries de mesures analysées simultanément, afin de décrire le spectre le plus complet du mouvement de l'objet.

Actuellement, deux codes développés à l'ISL permettent l'étude d'objets en vol : un code direct et un code inverse. Le ***code direct*** permet de calculer des trajectoires à partir de l'intégration des équations du mouvement, pour des modèles à 6 et 7 degrés de liberté [4]. Ce programme de

4. Le modèle à 7 degrés de liberté (7DOF) permet l'étude de corps composés de deux parties coaxiales découplées en roulis [Wey (2014)].

simulation de trajectoires suppose les conditions initiales, les caractéristiques aérodynamiques et mécaniques connues. A contrario, le ***code inverse*** suppose les conditions de tir connues et vise à déterminer les coefficients aérodynamiques à partir de données de vol libre, pour des structures de modèles à 6 degrés de liberté [Fleck (1998)]. Nos études préliminaires ont été menées à partir du code inverse puisque sa fonction est similaire à notre objectif. Néanmoins, il présente à ce jour certaines limitations. Par exemple, le modèle qui décrit le comportement en vol d'un objet est linéarisé et est basé sur l'approximation de Gauss, également appelée approximation des petits angles. De plus, il ne permet pas une estimation des coefficients autres que de manière tabulaire, pour des valeurs fixes du nombre de Mach ou de l'incidence. Afin de palier ces restrictions et visant à améliorer l'outil existant, la contribution majeure de ce travail a consisté à développer un nouveau code inverse à 6 degrés de liberté, Inv6DoF, avec intégration de techniques d'identification. En particulier, par l'implantation de modèles mathématiques plus complets permettant d'estimer et de maximiser le niveau de confiance des paramètres aérodynamiques obtenus à partir d'un ("single fit") ou de plusieurs ("multiple fit") essais en vol libre. Cet outil a été testé et validé pour les deux applications, un corps de rentrée dans l'atmosphère et un projectile stabilisé par empennage appelé "Basic Finner".

Ce manuscrit relate divers aspects d'ordre expérimental et méthodologique et s'articule autour de quatre chapitres.

Le Chapitre 1 présente le contexte expérimental. Nos choix d'étude concernant la procédure d'identification furent principalement orientés par le cadre expérimental et les données disponibles mesurées en vol libre. Il est essentiel de prendre conscience de l'importance du bon déroulement des essais pour obtenir des données exploitables. Deux types de véhicules ont été étudiés : une sonde spatiale et un projectile de référence. L'optimisation et la conception des maquettes ainsi que des sabots utilisés pour le lancement du modèle étudié au moyen d'un canon seront également détaillées. Pour l'obtention de données en vol libre, les véhicules sont instrumentés de dispositifs électroniques adaptés à chaque application. Indépendamment de la technique utilisée pour l'acquisition de données, les mesures des capteurs embarqués sont de même nature pour les deux cas et sont essentiellement issues des capteurs magnétiques. En plus des données mesurées par les capteurs, deux techniques de mesure complémentaires permettent d'obtenir des informations sur le comportement de l'objet en vol et seront présentées dans ce chapitre. Ainsi, plusieurs essais en vol libre ont été réalisés pour les deux cas d'étude et ont permis l'acquisition de données en vol, indispensable à l'étape d'identification des paramètres aérodynamiques.

Le chapitre 2 est dédié à la première étape de la procédure d'identification qu'est la modélisation mathématique issue des lois de la Physique. Le comportement d'un véhicule en vol libre est décrit par un modèle d'état non linéaire composé de 12 variables d'état. Ces équations différentielles sont directement reliées aux coefficients aérodynamiques à estimer. Une description des coefficients aérodynamiques pour chacune des deux applications traitées est nécessaire pour compléter le modèle aérodynamique. Ces travaux tentent d'améliorer la représentation de ces coefficients dans le code existant. Ainsi, les descriptions proposées ont été judicieusement adaptées à partir de celles existantes dans la littérature et de connaissances *a priori* du système et se formulent en fonction du nombre de Mach et de l'incidence. Le comportement d'un objet en vol libre est caractérisé

par l'absence d'un signal d'entrée mais également par les conditions initiales des variables d'état inconnues, qui sont également à déterminer en plus des coefficients aérodynamiques. Concernant les équations de sortie, elles décrivent les données mesurées durant les essais en vol libre et sont au nombre de quatre, soit la vitesse de l'objet obtenue par le radar Doppler et les trois équations décrivant les signaux des magnétomètres.

Le chapitre 3 introduit la procédure d'identification des coefficients aérodynamiques et détaille l'ensemble des étapes menées. A partir des équations d'évolution et d'observation caractérisant le comportement d'un objet en vol libre et des données disponibles, l'estimation paramétrique peut être réalisée mais reste néanmoins un problème inverse difficile à résoudre. Les paramètres sont identifiés à partir d'un modèle boîte grise dans lequel les coefficients aérodynamiques sont décrits par des fonctions paramétriques interprétables physiquement. Plusieurs analyses sont considérées dans la procédure d'identification pour guider l'estimation des paramètres, en particulier, les analyses liées à la faisabilité de l'estimation. Elles sont menées à travers des études d'identifiabilité *a priori* et *a posteriori*, qui évaluent à différents degrés la possibilité d'estimer les paramètres, à partir de la structure du modèle considéré et/ou des grandeurs mesurées. Des études d'identifiabilité sont effectuées pour le cas de la sonde spatiale. Les résultats obtenus mettent en évidence la complexité des analyses d'identifiabilité des paramètres en présence de dépendances non linéaires entre les variables, mais également l'augmentation du nombre de paramètres identifiables lorsque plusieurs essais sont considérés simultanément. Ce dernier point est révélateur de l'amélioration de l'estimation à partir de plusieurs séries de données analysées simultanément. Par conséquent, l'estimation est proposée à travers deux étapes. Dans un premier temps, les conditions initiales et les paramètres décrivant les coefficients aérodynamiques sont estimés de manière indépendante pour chaque essai en vol libre. Dans un second temps, les paramètres sont ré-affinés à travers une stratégie "multiple fit".

Le chapitre 4 présente les résultats des principales caractéristiques de chacune des deux applications, la sonde spatiale et le projectile. Guidé par les résultats issus des analyses composant la procédure d'identification, les conditions initiales et les paramètres décrivant les coefficients aérodynamiques peuvent être estimés à partir de données de vol libre. L'estimation est menée à partir du code inverse développé, comprenant l'ensemble du modèle à 6 degrés de liberté décrivant le comportement d'un objet en vol libre, les descriptions des coefficients aérodynamiques spécifiques à chaque application traitée, ainsi que les équations de sorties associées à la vitesse obtenues à partir du radar Doppler et aux signaux du magnétomètre tridimensionnel. Différents résultats sont ainsi exposés, tels que les signaux mesurés, l'évolution des variables caractérisant le comportement en vol d'un objet et les coefficients aérodynamiques estimés à travers une stratégie "single" ou "multiple fit". De plus, dans le cas du projectile, les résultats obtenus à partir de différentes techniques de mesure sont comparés. Suite à l'analyse des caractéristiques aérodynamiques, une comparaison entre les deux cas d'application est effectuée, ce qui permet de justifier et de différencier le comportement en vol de chaque véhicule.

Chapter 1

Aerodynamic testing

The purpose of this project is the identification of the aerodynamic coefficients from free flight data. In exterior ballistic domain, these coefficients are used for the characterization of the behaviour of an object in flight. Their determination is directly dependent of the quality and quantity of available measurements obtained during free flight tests. In this sense, the experimental set-up must be handled as a priority and is detailed in the present chapter.
The free flight tests were conducted at the ISL's open range test site with two instrumented architectures: an Earth re-entry vehicle and a Basic Finner projectile. Despite the differences between these two architectures, the experimental procedure is similar. From the vehicle/sabot package conception to the integration of the electronics, several analysis and measures must be done in order to validate the entire model[1]*. This chapter specifies the requirements needed for each experimental step. The available measurement techniques at the ISL to collect free flight data are presented as well as the different data acquisition approaches. Finally, the test conditions and the test cases selected for the undertaken studies are introduced.*

As it was already noted in the Introduction part, there exist several possibilities to quantify the aerodynamic coefficients of vehicles. In terms of experimental methods, one can count wind tunnel and free flight tests. In order to study the behaviour of an object in flight, free flight tests, considered as reference, are conducted to reveal the real aerodynamics of a vehicle. For the free flight trials, several facilities exist:

- ballistic spark range facility, such as that of the Defence Research and Development Canada (DRDC) of Valcartier, was initially employed to characterize the aerodynamics of ammunitions [Murphy (1954, 1963), Dupuis and Hathaway (1997)]. In the last decades, the investigation was extended to space vehicle configurations [Schoenenberger et al. (2009), Winchenbach et al. (2002)];
- ballistic proving grounds, generally used for military purposes, allow to experiment prototypes. Examples of such facilities are that of DGA Techniques Terrestres located at Bourges or that of the army proving ground WTD91 in Meppen, Germany, where tests can be performed on distances up to 30 km. The free flight tests can be carried out with instrumented or non-instrumented models and different experimental conditions. For example, these facil-

1. In this chapter, the term *model* is employed to make reference to the flying vehicle type and not the mathematical model

ities enable to study trajectories at different elevations, over different distances, initial yaws, or velocities.

Before going further, it is important to introduce the notion of the Mach number, often used in the field of exterior ballistic to express the velocity. It is a dimensionless quantity defined as the ratio of the velocity V to the speed of sound a, as follows:

$$M = V/a \tag{1.1}$$

There are many ways to classify flow regimes according to the flow structure, its physical situation or its configuration. The flow regimes can essentially be divided in four groups: subsonic, transonic, supersonic and hypersonic, as presented in Table 1.1. If the velocity is small ($M < 0.8$), the density variations are also small and the flow is said to be either subsonic incompressible ($M < 0.3$) or either subsonic compressible ($0.3 < M < 0.8$). For Mach number values higher than the speed of sound ($1.2 < M < 5.0$), shock waves are present and flow regimes are said to be supersonic. For Mach numbers ranging between 0.8 and 1.2, the flow is called transonic and refers to flight conditions where shock waves start to appear, shows unsteadiness and contains both subsonic and supersonic regions mixed together. For regimes approaching or exceeding $M = 5.0$, dissociation and ionization of airflow will occur and the flow is considered hypersonic. In the present studies, only the transonic and the supersonic flow regimes were considered.

Regime	Mach range
Subsonic	M < 0.8
Transonic	0.8 <M< 1.2
Supersonic	1.2 <M< 5.0
Hypersonic	M > 5.0

Table 1.1: Classification of the main flow regimes as a function of the Mach range

1.1 Architectures

In the frame of the present study, several flight experiments were carried out with two types of vehicles and for different initial experimental conditions, i.e. initial launch Mach numbers $M0$ and initial angles of attack $\alpha 0$. The considered architectures consist of an Earth re-entry space vehicle and a fin stabilized reference projectile.
The physical properties (mass m, center of gravity position X_{cg} and moments of inertia I_x, I_y and I_z) were measured by means of Space Electronics' state-of-the-art equipment. In both applications, models are assumed to be axisymmetric with a center of gravity located along the axial direction of the vehicle. In order to respect the location of the center of gravity and to facilitate the integration of the electronic package, models were manufactured in several parts by use of different non magnetic materials.

1.1.1 Space probe

In the space probe application case, preliminary flight experiments with full size vehicles are not possible due to the tremendous high costs in terms of design, launching and time consumption. For these reasons, the most reliable solution is to consider sub-scale models and to conduct experiments by duplicating as well as possible the dynamic scaling between a full size and the reduced scaled model. For dynamic stability investigations of re-entry space vehicles, the key dynamic flow parameters to take into account are:

- the Reynolds number: it is believed that similarity in terms of flow regime must be achieved, but once a turbulent flow regime is established, the Reynolds number dependency are believed to be minimal for such blunt bodies [Winchenbach et al. (2002)];
- the Mach number M: this parameter, easy to duplicate, is much more important since blunt bodies experience dynamic instabilities at a limited range of Mach number between 0.9 and 3.0;
- the reduced spin rate : $\tilde{\omega}_x = \omega_x d/2V$, where ω_x is the spin rate and d the vehicle diameter;
- the relative density parameter: $m/\rho d^3$, and the relative mass moment of inertia : md^2/I_t, where ρ is the air density and I_t the transversal moment of inertia when the postulate of $I_y = I_z$ is made. These two ratios are contained in the non-dimensionalized equations of motion for a decelerating vehicle [Berner et al. (2012)];
- the reduced frequency parameter $\tilde{f}$ (RFP): this parameter involves the oscillation frequency f which represents the ratio of a characteristic length of the model to the wave-length of the oscillation [Berner et al. (2009), Dobre et al. (2015)].

Consequently, the optimization of the parameters that allows duplicating flow and dynamic scaling, for characterizing the real vehicle in free flight, consists in:

- reducing model diameter to duplicate the Reynolds number,
- reducing the model diameter and increasing the model mass to duplicate the relative density parameter,
- maximizing the transverse inertia moment to improve the reduced frequency, or increase the density. This last solution is not very convenient on ground facilities.

The sub-scale space probe consists of a blunt forebody with an half-angle of 70° and a spherical nose (R20), linked to the afterbody by a shoulder radius (R2) as shown in Figure 1.1. The base geometry consists of a conical afterbody with an half-angle of 47° and three cavities ended by a radome. The reduced scale of the model was 1/30 compared to the real space configuration, resulting in a nominal model diameter d of 80 mm with a length L of 45.69 mm. The model design was bounded by three main criteria: the integration of the electronic package, the center of gravity location and the need for access to the transducers.
The measured physical properties of the space probe models to be fired and selected for this study are summarized in Table 1.2.

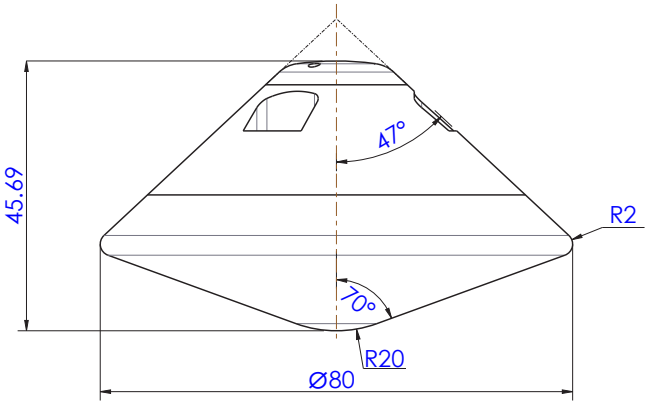

Figure 1.1: Schematic of a space probe configuration

Model #	d (mm)	L (mm)	m (g)	$X_{cg}/nose$ (mm)	X_{cg}/d (%)	I_x $(kg.m^2)$	I_y $(kg.m^2)$	I_z $(kg.m^2)$
A1	80.02	45.74	1246.9	21.22	26.52	$7.6918 \cdot 10^{-4}$	$4.8267 \cdot 10^{-4}$	$4.8206 \cdot 10^{-4}$
B1	80.07	45.75	1246	21.21	26.49	$7.7057 \cdot 10^{-4}$	$4.8367 \cdot 10^{-4}$	$4.8311 \cdot 10^{-4}$
C1	80.01	45.71	1243.9	21.24	26.55	$7.6810 \cdot 10^{-4}$	$4.8121 \cdot 10^{-4}$	$4.8121 \cdot 10^{-4}$
D1	80.00	45.8	1233.3	21.13	26.41	$7.6269 \cdot 10^{-4}$	$4.7398 \cdot 10^{-4}$	$4.7377 \cdot 10^{-4}$

Table 1.2: Measured properties of space probe models

1.1.2 Projectile

The configuration considered in this study was a fin stabilized reference projectile called Basic Finner. It was chosen due to its large collection of data published in the literature, obtained through Computational Fluid Dynamics (CFD) predictions, wind tunnel and/or free flight tests [Dupuis and Hathaway (1997), Dupuis (2002)]. The projectile consists of a 20° nose cone on a cylindrical body equipped with four rectangular fins. The nominal caliber d of the projectile is 28 mm for a total length L/d of 10.0. Fin dimensions are equal to 1 caliber x 1 caliber and have a conical shape with a thickness of 0.08 calibers at the base. A schematic of the projectile is presented in Figure 1.2 where all the dimensions are given in caliber. Fins were canted at $\delta = 0°$ and $\delta = 2°$ to produce the desired roll motion, and two center of gravity positions X_{cg1} and X_{cg2} were studied.
The measured physical properties of four cases characterizing each studied projectile, i.e. $\delta = 0°$ or 2° and the center of gravity position with $X_{cg1}/L \simeq 60\%$ or $X_{cg2}/L \simeq 65\%$, are summarized in Table 1.3.

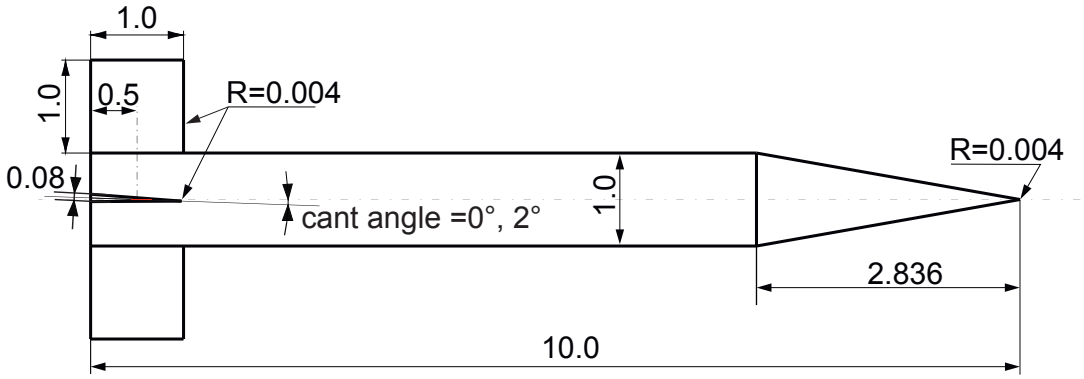

Figure 1.2: Schematic of the Basic Finner projectile

Model #	d (mm)	L (mm)	δ (°)	m (g)	$X_{cg}/nose$ (mm)	X_{cg}/L (%)	I_x $(kg.m^2)$	I_y $(kg.m^2)$	I_z $(kg.m^2)$
A2	28	280.3	0	345.6	169.15	60.35	$4.14 \cdot 10^{-5}$	$1.76 \cdot 10^{-3}$	$1.76 \cdot 10^{-3}$
B2	28	280.3	0	413.4	182.7	65.18	$4.366 \cdot 10^{-5}$	$2.141 \cdot 10^{-3}$	$2.141 \cdot 10^{-3}$
C2	28	279.1	2	345.2	168.18	60.26	$4.167 \cdot 10^{-5}$	$1.756 \cdot 10^{-3}$	$1.757 \cdot 10^{-3}$
D2	28	280.1	2	413.2	182.7	65.23	$4.322 \cdot 10^{-5}$	$2.131 \cdot 10^{-3}$	$2.126 \cdot 10^{-3}$

Table 1.3: Measured properties of projectiles

1.2 Sabot design

Since the sub caliber models have to be launched from a smooth bore powdered gun, special sabots were designed at different initial angles of attack $\alpha 0$. The initial angle of attack characterizes the orientation of the model into the sabot before firing [2]. For the sabot separation without high initial disturbances, the main aspects to consider for the sabot design are the model geometry, the total mass, the muzzle velocity and the gun acceleration. Some of the aspects like separation, acceleration and velocity have to be consistent from one trial to another.

1.2.1 Space probe

For this test campaign, two types of sabots, one with three and one with four petals, were designed to launch the space probe models. All sabots were manufactured with initial angles of attack of 0, 3 and 6°. For non-spinning models, preliminary sabot/model integrity trials have shown that a four-piece petal sabot made in polypropylene separates well within a distance of 5 meters, regardless of the initial angle of attack and Mach number. Figure 1.3a shows an example of a four-piece petal sabot separation. For spinning models, initial disturbances were observed during separation with the four-piece petal sabot. Therefore, a three-piece type petal sabot, also made in polypropylene, was designed, as shown in Figure 1.3b. With this last design, the sabot separation is done without disturbing the model in flight. Furthermore, to induce an initial spin to the model, three driving pins adjusted to the location of each cavity were added into the sabot, as it can be observed on the left of Figure 1.3b. Gas leakage through the sabot body is prevented by use of some gasket located at the end of the sabot. With this design, no pusher plate or base pad seal located at the aft end of the sabot was necessary. The diameter of the sabot is 91 mm with a skirt at the aft end of 97 mm in diameter for a total length of 85.2 mm.

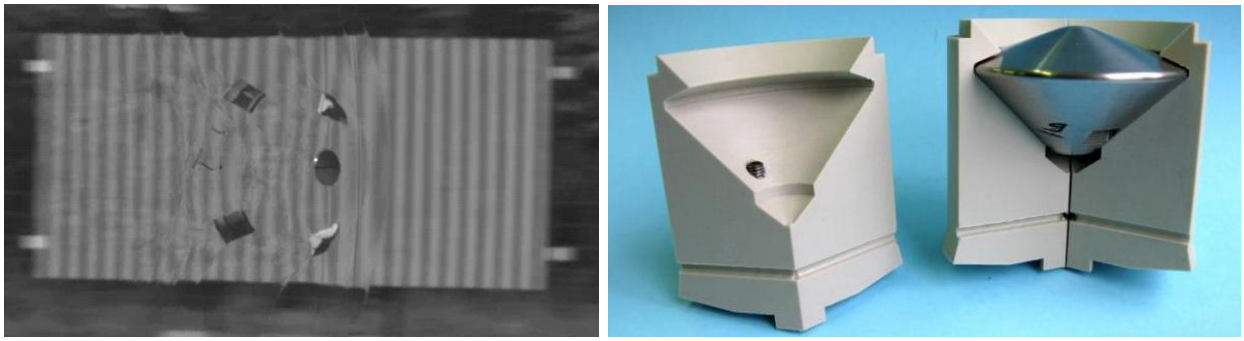

(a) Four-piece petal sabot separation

(b) Space probe model mounted into a three-piece petal sabot for $\alpha 0 = 0°$

Figure 1.3: Sabot for a space probe model

1.2.2 Projectile

For the Basic Finner projectiles, sabots were designed to launch the models at initial angles of attack of 0 and 4°. The sabots consist of a four-piece petal type made of polypropylene. A photograph of the model/sabot package for an initial angle of attack of 4° is presented in Figure 1.4a. The projectile sabot design needs additionally a base pad seal to prevent gas leakage through the sabot body made in aluminium and a pusher plate located at the aft end of the sabot visible in Figure 1.4a. The external diameter of the sabot is 91 mm with a skirt at the aft end of 95 mm in

2. The initial angle of attack $\alpha 0$ considered here is different than the initial condition of the angle of attack α_0 introduced in the next chapter.

diameter for a total length of 96 mm. Trials have shown that the four-piece petal sabot separates well within a distance ranging between 8 to 10 meters depending on the initial Mach number, as shown in Figure 1.4b.

(a) Projectile mounted into the sabot for $\alpha 0 = 4°$

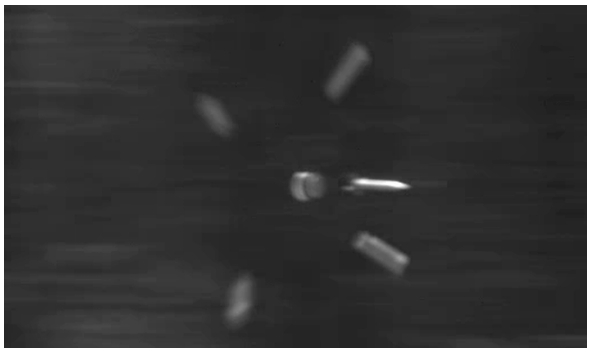

(b) Sabot separation

Figure 1.4: Sabot for a projectile

1.3 Model instrumentation and data acquisition

Aerodynamic characteristics, such as angular motion and aerodynamic coefficients, can be determined from observed motions on photographs obtained from spark-shadowgraph stations [Schoenenberger et al. (2009), Hathaway (1976), Winchenbach (1997)]. This method is accurate but is limited in terms of numbers of measurement instants (equal to the number of spark-shadowgraph stations) and in range. The attitude determination can only be done at each station location. Indeed, a large number of stations is required to increase the result precision and to observe angular motion as continuous as possible. In the last decades, ISL has developed a technique, unique in Europe, for their determination from on-board instrumented vehicles [Fleck (2000)]. Indeed, the three-axis magnetometer embedded in the vehicle measures the projection of the Earth magnetic field on the sensor axes. The reference direction used is the orientation of the Earth magnetic field considered constant and the sensor is aligned with the vehicle's body axes. This allows the determination of the angular position during the flight with an accuracy better than 5 mrad. More recently, embedded accelerometers [3] were employed that could be used for the determination of the forces acting on the vehicle. In this sense, the components of the electronic package equipping both models consist of 3D magnetic sensor, 2D or 3D accelerometer, a power supply and a trigger system.

For the integration into the models, the electronic package requires to have units as small as possible due to the space limitation. In order to prevent damage due to the high launch accelerations and/or impact shocks, each electronic package is potted into the model with resin and is g-hardened. Special attention was paid to the calibration of the sensors represented by the offsets, sensitivities and misalignment angles. Measurement methods developed at ISL are applied before each trial to obtain the calibration factors relative to a perfect orthogonal orientation thanks to a 3D-Helmholtz coil facility [Bieber et al. (2014)].

Unfortunately, access to the measured data is one major problem. Generally, two different approaches can be applied for measurement acquisition:

1. on-board data recording and soft recovery of the vehicle after flight;
2. on-line data transmission via conventional telemetry techniques.

3. These sensors were integrated into the models but accelerometer data will not be processed in this report.

1.3.1 Space probe

Data acquisition for space probes was done through on-board data recording. Due to high velocity decrease during the flight, models were softly recovered without suffering heavy damage of the sensors. This technique allows to proceed to multiple tests with the same model. The space probe electronic package is shown in Figure 1.5a. The additional electronic components that equipped space probe models consist in a flight recorder and a USB interface, as shown in Figure 1.5b. Thus, the communication with a computer can be done via the USB port after the soft model recovery to have access to the data.

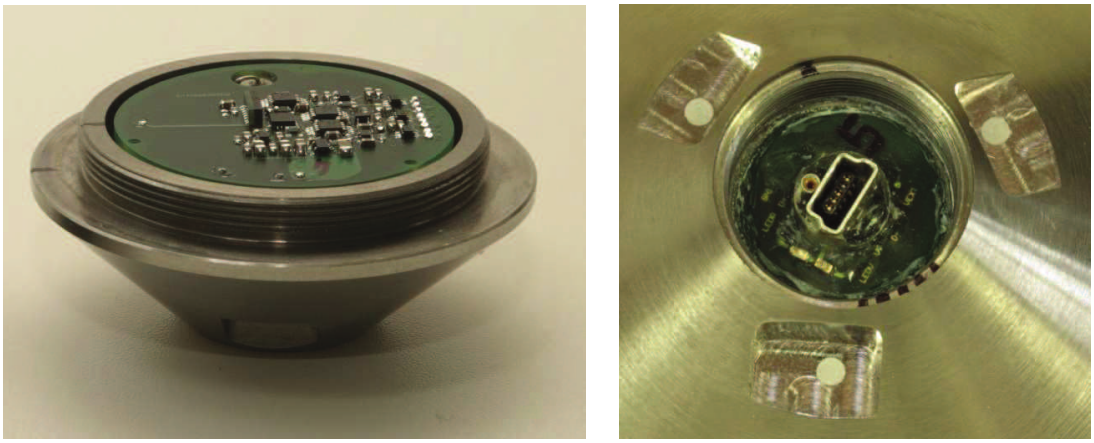

(a) Embedded electronics (b) USB interface

Figure 1.5: Electronic package of the space probe model

1.3.2 Projectile

In the case of the projectile, the velocity decay in flight is small and therefore, the impact velocities at the target remain important. The recording of the sensor data during flight was obtained by telemetry. This procedure has the great advantage that no soft recovery of the model is necessary, and data timing has microsecond accuracy relative to the flight path data. To collect data with this method, a transmitter and an antenna, located in the projectile nose, are added to the electronic package. The full projectile electronic package is presented in Figure 1.6.

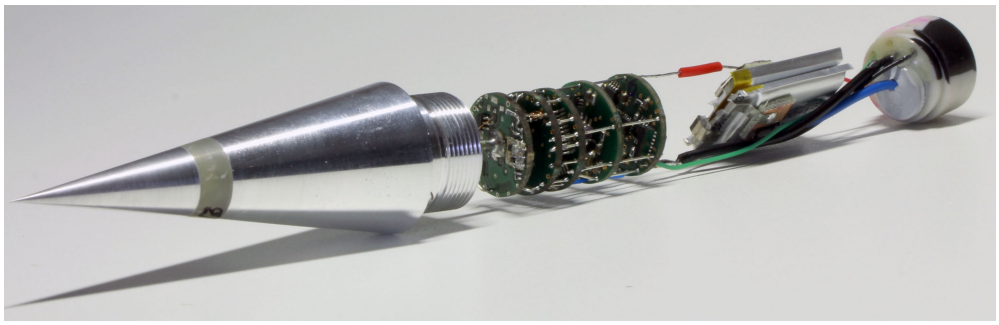

Figure 1.6: Electronic package of the Basic Finner projectile

1.4 Open range test facility and measurement techniques

Free flight experiments performed in the frame of this study were conducted at the open range facility of the ISL proving ground located in Baldersheim about 25km north of Saint-Louis. This range is tailored to meet a wide variety of inert free flight models. Experiments can be carried out over firing distances up to 1000 meters with rifled or smooth bore powder guns with calibers ranging between 20 and 105 mm. Velocity regimes, as a function of the studied configurations, are ranging between Mach 0.6 and 6.0. A top-view of the open range test site including the available measurement techniques is presented in Figure 1.7, in which each device is denoted by a letter. In both cases, models were fired from a classical 91 mm smooth bore gun (**a**) at atmospheric conditions over a flight distance of 235 meters on average and with rectilinear trajectories. Models are launched at known initial velocities and fixed initial angles of attack. After exiting the gun muzzle, sabots separate from the models at a certain distance depending on the initial velocity and the total mass to be fired. Therefore, models can be considered to be in free flight only after a distance (from 5 to 8 meters) where the sabot petals do not interact anymore with the model.
Velocities of the models are measured with a continuous Doppler radar (**b**) with a frequency range of 10.52 GHz, located next to the gun barrel. Radar data are reduced and processed by means of a FFT (Fast Fourier Transform) analyzer.
For the qualitative observation of the model behaviour during flight and the impact at the target, a high speed video trajectory tracker (**c** - position **A**) from Specialized Imaging Ltd. was used, composed of a motorized mirror to follow the vehicle during the flight.
None of these above mentioned measurement techniques allow the determination of the position in space. In free flight, the determination of the position is only possible with tracking radars that are usually used to follow projectiles over a few kilometers. In our case, the acquisition of such a piece of equipment would be a non-sense for distances less than 1000 meters. Therefore, the external instrumentation has been improved with a second high speed trajectory tracker (**c** - position **B**) located at the other side of the fireline. The 3D high-speed video trajectory tracker system was designed to determine the 3D position and the attitude of the vehicle along the flight path, and allows to compare the results to those obtained from on-board 3D magnetic sensor technique. The principle is to simultaneously capture sequences of images from both trackers, treated afterwards by image processing [Portier (2014)].
In order to properly follow the models, two sky screens (**d**) were used for the correction of the motorized mirror scanning speed of the trajectory trackers. Triggering of the experiments was obtained by means of a flash muzzle detector (**e**).
In the case of the space probe models, multiple soft recovery units (**f**), composed of recycled rugs and/or hemp, were placed at the end of the trajectory to softly recover the models without suffering heavy damage of the sensors. In the case of projectile, as data are collected by telemetry, no soft recovery is necessary and models end into the sand bay (**g**). Further details about the open range test site, experimental set-up and test conditions are given in [Berner et al. (2012)].

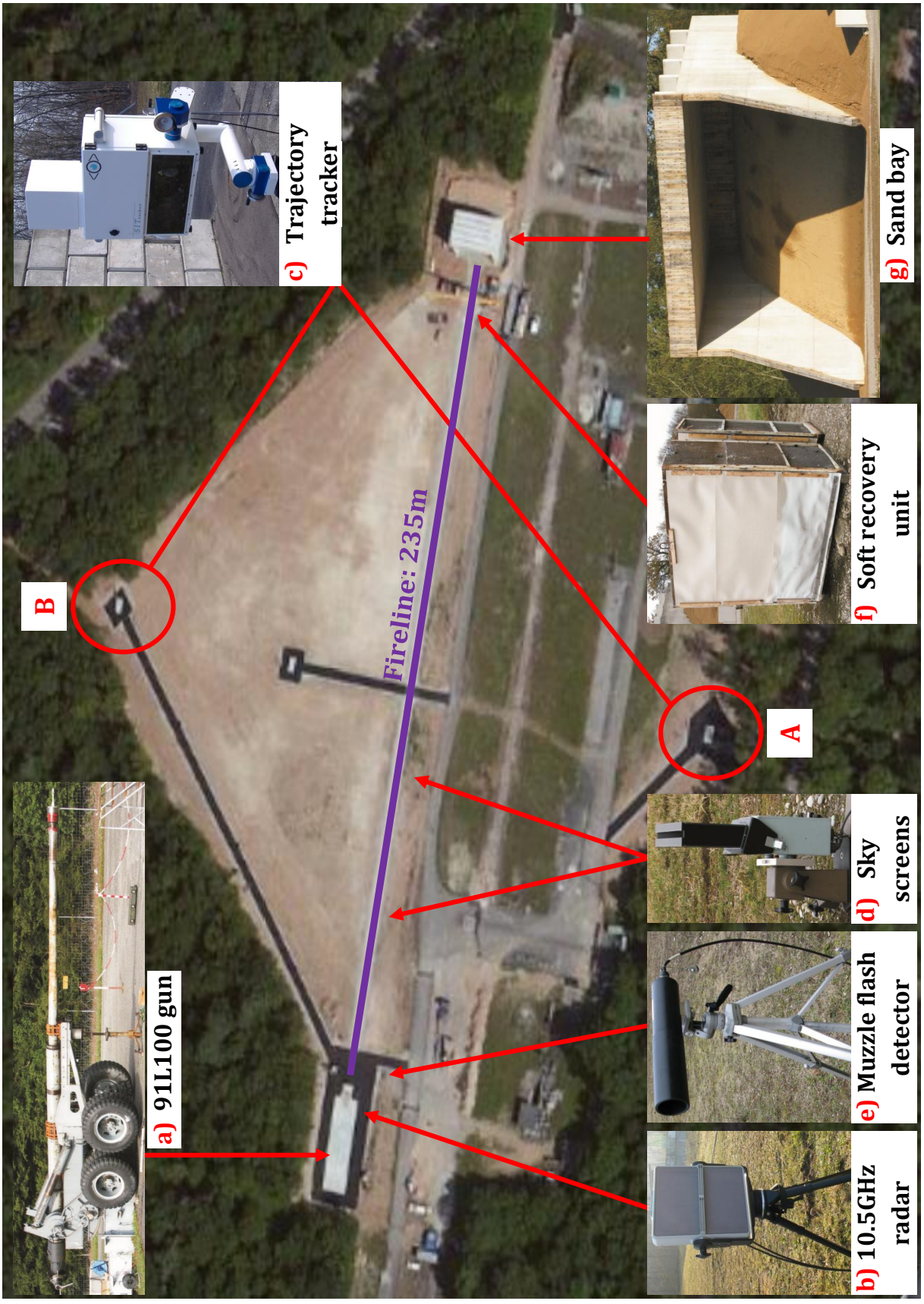

Figure 1.7: Top-view of the open range test site

1.5 Test conditions

Free flight experiments were carried out for electronically instrumented configurations. Only two criteria define the constraints imposed by the experimental conditions, the initial Mach number $M0$ and initial angle of attack $\alpha 0$.

1.5.1 Space probe

Within the context of a third party contract with ESA (European Space Agency), two test campaigns were conducted with a space probe at different initial Mach numbers $M0$ ranging between 2.0 and 3.0, for initial angles of attack $\alpha 0$ of 0, 3 and 6° and for two different center of gravity positions X_{cg1} and X_{cg2}. For this study, five non-contractual spinning free flight tests having the same center of gravity position X_{cg1} were selected and are summarized in Table 1.4. The corresponding models used for each test case are specified in the test matrix. Due to the soft recovery, the model #B1 was fired twice which explains why the same model was used for test cases 2 and 3.

	$M0 = 2.0$	$M0 = 3.0$
$\alpha 0 = 0°$	test case 1 (model #A1) test case 2 (model #B1)	test case 4 (model #C1) test case 5 (model #D1)
$\alpha 0 = 3°$	test case 3 (model #B1)	

Table 1.4: Test matrix for the space probe models

Spinning of the model was obtained by fixing a special rifled adapter at the gun muzzle as shown in Figure 1.8a. It consists of an adapter made of steel with a length of 240 mm and twelve straight grooves of 1 mm thick canted at an angle of 0.6° and manufactured by EDM (Electrical Discharge Machining). A close view of the adapter is presented in Figure 1.8b.

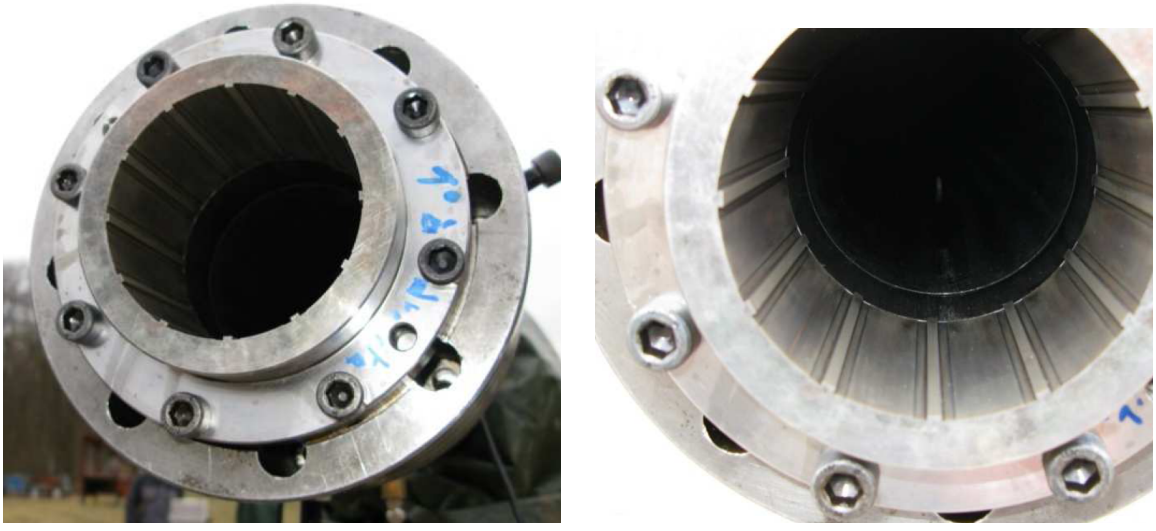

(a) (b)

Figure 1.8: Spin adapter

1.5.2 Projectile

A total of 16 free flight tests were conducted with instrumented configurations at different initial conditions as summarized in Table 1.5. Models with two center of gravity positions X_{cg1} and X_{cg2} were launched for initial Mach numbers of 1.3, 1.8 and 2.6, for initial angles of attack $\alpha 0$ of 0 and 4° and for two fin cant angles δ of 0 and 2°. However for a small number of tests, and due to unexplained electronic failures, signals were only transmitted and registered over a few percent of the full trajectory. This makes, of course, the parameter estimation impossible. Therefore, only the most relevant tests in terms of data quantity and quality were selected to proceed to the parameter estimation step. The four selected models characterizing each projectile configuration (models #A2,#B2, #C2 and #D2) are specified in the test matrix.

	$M0 = 1.3$		$M0 = 1.8$		$M0 = 2.6$	
X_{cg1}	$\delta = 0°$	$\delta = 2°$	$\delta = 0°$ (model #A2)	$\delta = 2°$ (model #C2)	$\delta = 0°$	$\delta = 2°$
X_{cg2}	$\delta = 0°$	$\delta = 2°$	$\delta = 0°$ (model #B2)	$\delta = 2°$ (model #D2)	$\delta = 0°$	$\delta = 2°$

Table 1.5: Test matrix for the Basic Finner projectiles

1.6 Concluding remarks

Several steps are needed to proceed to free flight experiments such as the model/sabot conception, the integration of the electronic package, the calibration of the sensors, the experimental design, and the free flight data acquisition from embedded sensors and ground measurement techniques. Each aspect of the experiment must be perfectly mastered by the experts in charge of these works. However, these technical steps are highly sensitive and can have irremediable consequences on the quality and quantity of collected data. For both applications, free flight measurements were obtained from two measurement techniques: Doppler radar and 3D magnetometer. From these data, the aerodynamic parameters can be now estimated. However, in order to proceed to their determination, the behaviour of a vehicle in free flight must be modelled, where the obtained measurements are described by the observation equations. This is the aim of the next chapter.

Chapter 2

Modelling of a vehicle in free flight

Experiments make it possible to access the data obtained by means of different measurement techniques. This data is essential to conduct parameter estimation. In order to reach this objective, an identification procedure composed of several steps must be defined. This chapter presents the first step of the proposed aerodynamic coefficient identification procedure, the physical modelling, namely the construction of mathematical models of dynamical systems. To have a physical interpretation of the state variables, the model describing the behaviour of a vehicle in free flight is constructed based on Newton's and Euler's laws. This mathematical model includes both the vehicle equations of motion and the aerodynamic coefficient descriptions. The state equations are formulated as ordinary differential equations and observation equations for the measured outputs. It is a nonlinear state-space model composed of 12 state equations and 4 output measurement equations. The equations of motion are valid for several types of vehicle in flight like space probes, Unmanned Aerial Vehicles, ammunition or airplane, and depend on the considered coordinate frame. Furthermore, it is assumed that the vehicle is a rigid body. The proposed aerodynamic coefficient model equations are described using polynomials and polynomial splines with time-invariant parameters, which are precisely the parameters to be estimated, and depend on several state variables. The presented aerodynamic model is valid only for space probe and ammunition architectures.

2.1 Coordinate systems

Before developing the vehicle equations of motion, a description of the coordinate systems and sign conventions is mandatory. All these reference frames are right handed and have orthogonal axes. Generally, three main frames are taken into account:

- **Earth frame** O_{x_E,y_E,z_E}, commonly used to determine the vehicle motion with respect to (*w.r.t.*) fixed axes, is defined about the Earth. Its origin is an arbitrary point on the Earth surface, where the positive O_{x_E} axis points toward the geographic North, the positive O_{y_E} axis points to the East, and the positive O_{z_E} axis points to the center of the Earth.

- **Body frame** $O_{x,y,z}$ is fixed *w.r.t.* the studied vehicle and is moving with it. The origin of this reference frame is situated at the vehicle center of gravity, with positive O_x pointing downrange through the vehicle nose, positive O_y axis in the horizontal plane and pointing to the right looking downrange, and positive O_z axis pointing down *w.r.t.* the body. In this study it can be assumed that O_{xz} plane is a plane of symmetry of the vehicle.

- **Wind frame** O_{x_W,y_W,z_W}, also called aerodynamic or stability frame, is relative to the vehicle trajectory through the air. Its origin is located at the vehicle center of gravity, with positive

O_{x_W} axis aligned with the velocity vector, positive O_{y_W} axis pointing out the right side, and positive O_{z_W} axis pointing down.

These reference frames are illustrated in Figure 2.1 and their descriptions are summarized in Table 2.1, more details can be found in [Zipfel (2000), Klein and Morelli (2006), Cook (2012)].

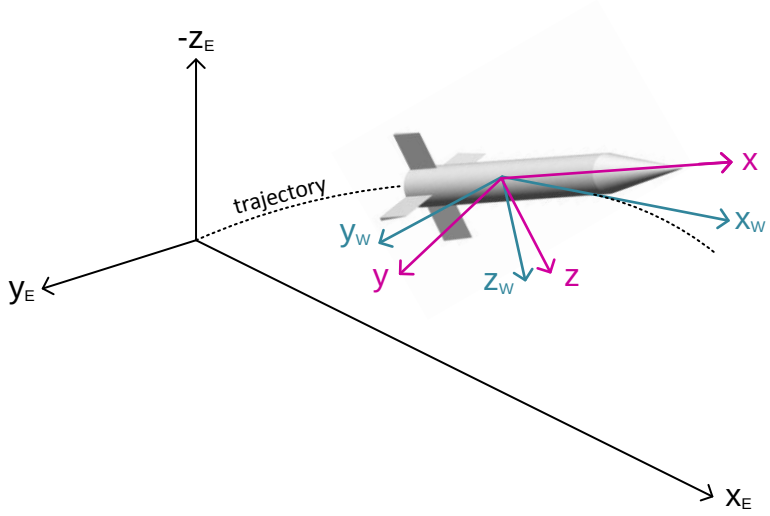

Figure 2.1: Earth, body and wind frames

Earth Frame O_{x_E,y_E,z_E} Origin: arbitrary point on the Earth surface		
O_{x_E} toward geographic North	O_{y_E} toward geographic East	O_{z_E} toward the center of the Earth
Body Frame $O_{x,y,z}$ Origin: vehicle center of gravity		
O_x downrange through the vehicle nose	O_y out the right side	O_z down
Wind Frame O_{x_W,y_W,z_W} Origin: vehicle center of gravity		
O_{x_W} aligned with the velocity vector	O_{y_W} out the right side	O_{z_W} down

Table 2.1: Reference frames

2.2 General structure of the model

Mathematical modelling is the process aiming at developing an adequate mathematical representation of certain physical systems. Generally, to reveal most of the observed phenomena, a dynamic model is preferred. Such models appear under multiple representation forms: linear or nonlinear models described as differential or difference equations, in a state-space or input-output form, in continuous or discrete time, considered as deterministic or stochastic, see e.g. [Ljung and Glad (1994)].

The mathematical model describing the behaviour of a vehicle in free flight, based on Newton's and Euler's laws of a rigid-body motion, is represented by a continuous-time nonlinear state-space

model [Fleck (1998), Zipfel (2000)]. Knowing that in our case the input signal $u(t) = 0$, it has the following general structure

$$\mathcal{M} : \begin{cases} \dot{\mathbf{x}}(t) = f(\mathbf{x}(t), \mathbf{C}(\mathbf{x}(t), \mathbf{p}_a)) & \mathbf{x}(0) = \mathbf{x}_0 \\ \mathbf{y}(t) = g(\mathbf{x}(t)) \end{cases} \tag{2.1}$$

where $t \in \mathbb{T} \subset \mathbb{R}^+$ is the time variable and the vectors $\mathbf{x} \subset \mathbb{R}^{n_x}$, $\mathbf{x}_0 \subset \mathbb{R}^{n_x}$ and $\mathbf{y} \subset \mathbb{R}^{n_y}$ denote the state variables, their initial conditions and the output variables, respectively. The aerodynamic coefficients $\mathbf{C}$ depend of the state variables and the vector $\mathbf{p}_a \in \mathbb{P} \subset \mathbb{R}^{n_p}$, composed of model parameters describing the aerodynamic coefficients. The system dynamics are governed by f and g, which are nonlinear functions of the state variables and model parameters. To simplify the notations, the time dependence of the variables is omitted in the following sections.

2.3 State equations

2.3.1 Force and moment equations

For the development of the equations of motion of a vehicle in free flight, several assumptions are usually made:

- the vehicle is a rigid body with constant mass and fixed mass distribution;
- the air is considered at rest, relative to the Earth;
- the Earth is fixed in inertial space;
- the Earth surface can be approximated as flat;
- the gravity is uniform.

Force and moment equations represent the dynamic motion governing the behaviour of a vehicle in free flight and are directly relied to the aerodynamic coefficients. By definition, the force changes the translational motion of a vehicle whereas a moment reflects the aptitude of a force to make an object rotate about a vector or a point. Under the rigid body assumption, the behaviour of a vehicle in flight is described by Newton's second law of motion in translational and in rotational forms:

$$\mathbf{F} = \frac{d}{dt}(m\mathbf{V}) \tag{2.2}$$

$$\mathbf{M} = \frac{d}{dt}(\mathbf{I}\boldsymbol{\omega}) \tag{2.3}$$

where the quantities represent the applied force $\mathbf{F}$, the mass m, the translational velocity $\mathbf{V}$, the applied moment about the center of gravity $\mathbf{M}$, the angular velocity $\boldsymbol{\omega}$ and the inertia matrix $\mathbf{I}$. Equations (2.2) and (2.3) describe the translational and rotational equations of motion, where each vector is composed of three equations *w.r.t.* body axes. The vehicle motion is then described by six equations for six degrees of freedom. These vectors are given as follows

$$\mathbf{F} = \begin{bmatrix} F_x \\ F_y \\ F_z \end{bmatrix}, \qquad \mathbf{M} = \begin{bmatrix} M_x \\ M_y \\ M_z \end{bmatrix} \tag{2.4}$$

The translational and angular velocity vectors $\mathbf{V}$ and $\boldsymbol{\omega}$ respectively are defined by

$$\mathbf{V} = \begin{bmatrix} v_x & v_y & v_z \end{bmatrix}^T \tag{2.5}$$

$$\boldsymbol{\omega} = \begin{bmatrix} \omega_x & \omega_y & \omega_z \end{bmatrix}^T \tag{2.6}$$

and their components are represented in Figure 2.2 in body axes.

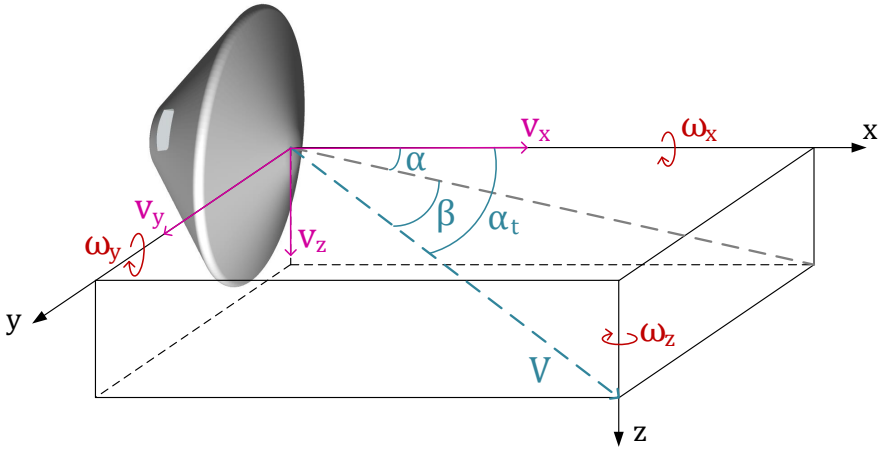

Figure 2.2: Representation of state variables of a space probe model

An assumption often used is that the inertia matrix $\mathbf{I}$ is considered to be diagonal [1]. The considered inertia matrix is then

$$\mathbf{I} = \begin{bmatrix} I_x & 0 & 0 \\ 0 & I_y & 0 \\ 0 & 0 & I_z \end{bmatrix} \tag{2.7}$$

where I_x, I_y and I_z are the longitudinal and lateral moments of inertia.
Equations (2.2) and (2.3) are valid in an Earth reference frame. However, it is generally recommended to express the variables of both previous equations in a body reference frame, which will translate and rotate relative to the Earth frame. For rotating body axes system, the derivative operator considered the rate of change of the vector components expressed in the body frame and the axis system rotation, formulate by the following equation:

$$\frac{d}{dt}(.) = \frac{\delta}{\delta t}(.) + \boldsymbol{\omega} \times (.) \tag{2.8}$$

By considering equations (2.2), (2.3) and (2.8), the force and moment equations in body axes are described by

$$\mathbf{F} = m\dot{\mathbf{V}} + \boldsymbol{\omega} \times m\mathbf{V} \tag{2.9}$$

$$\mathbf{M} = \boldsymbol{I}\dot{\boldsymbol{\omega}} + \boldsymbol{\omega} \times \boldsymbol{I}\boldsymbol{\omega} \tag{2.10}$$

The applied forces and moments contain aerodynamic, thrust and gravity components. In this application, the absence of propulsion allows to set the thrust force and moment to zero. Moreover, due to the rigid-body assumption made on the uniformity of the gravity applied through the vehicle center of gravity, there is no gravity moment acting on the vehicle. Consequently, the forces and moments equations can be written as

$$\mathbf{F}_A + \mathbf{F}_G = m\dot{\mathbf{V}} + \boldsymbol{\omega} \times m\mathbf{V} \tag{2.11}$$

$$\mathbf{M}_A = \boldsymbol{I}\dot{\boldsymbol{\omega}} + \boldsymbol{\omega} \times \boldsymbol{I}\boldsymbol{\omega} \tag{2.12}$$

1. For the model description with the complete inertia matrix, see e.g. [Klein and Morelli (2006)].

where $\mathbf{F}_A$ and $\mathbf{F}_G$ represent the aerodynamic and gravity forces respectively, and $\mathbf{M}_A$ the aerodynamic moment. These vectors are defined as

$$\mathbf{F}_A = \bar{q}S \begin{bmatrix} C_X \\ C_Y \\ C_Z \end{bmatrix}_B, \qquad \mathbf{F}_G = m \begin{bmatrix} -g\sin\theta \\ g\sin\phi\cos\theta \\ g\cos\phi\cos\theta \end{bmatrix}_B \tag{2.13}$$

$$\mathbf{M}_A = \bar{q}Sd \begin{bmatrix} C_l \\ C_m \\ C_n \end{bmatrix}_B \tag{2.14}$$

where the physical properties are the reference diameter d, the reference surface area $S = (\pi d^2)/4$ and the dynamic pressure $\bar{q} = \frac{1}{2}\rho V^2$, where ρ represents the air density. The global force and moment aerodynamic coefficients *w.r.t.* body axes are C_X, C_Y, C_Z and C_l, C_m, C_n, respectively, as illustrated in Figure 2.3. The gravity force vector is generally defined in the Earth frame. Herein, it is expressed in a body frame in relation to Euler angles (ϕ, θ), and its transformation from Earth to body axes is detailed in Appendix A.1 (subsection A.1.1).

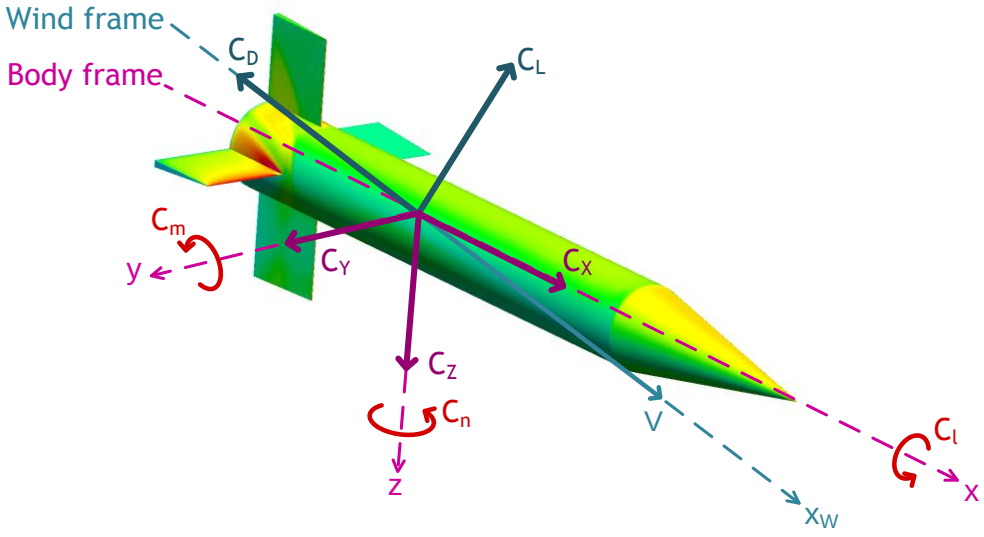

Figure 2.3: Global aerodynamic coefficients relied to forces and moments acting on a projectile

Thus, based on equation (2.11), the velocity vectors in (2.5-2.6) and the forces acting on the vehicle in (2.13), the body-axes force equations are expressed as

$$\dot{v}_x = (\omega_z v_y - \omega_y v_z) - g\sin\theta + \frac{\bar{q}S}{m}C_X \tag{2.15a}$$

$$\dot{v}_y = (\omega_x v_z - \omega_z v_x) + g\sin\phi\cos\theta + \frac{\bar{q}S}{m}C_Y \tag{2.15b}$$

$$\dot{v}_z = (\omega_y v_x - \omega_x v_y) + g\cos\phi\cos\theta + \frac{\bar{q}S}{m}C_Z \tag{2.15c}$$

Generally, the nondimensional aerodynamic force and moment coefficients are characterized as function of the velocity V, the angle of attack α and the angle of sideslip β, illustrated in Figure 2.2 [Klein and Morelli (2006)]. Therefore, it is often useful to write the force equations in terms of V, α and β instead of v_x, v_y and v_z. Their relations are defined as follows

$$v_x = V\cos\alpha\cos\beta; \qquad v_y = V\sin\beta; \qquad v_z = V\sin\alpha\cos\beta \tag{2.16}$$

and the reverse transformations

$$V = \sqrt{v_x^2 + v_y^2 + v_z^2}; \quad \alpha = \arctan(v_z/v_x); \quad \beta = \arcsin(v_y/V) \tag{2.17}$$

The wind axis force equations are obtained by differentiating *w.r.t.* time the equations (2.17)

$$\dot{V} = \frac{v_x\dot{v}_x + v_y\dot{v}_y + v_z\dot{v}_z}{V} \tag{2.18a}$$

$$\dot{\alpha} = \frac{v_x\dot{v}_z - v_z\dot{v}_x}{v_x^2 + v_z^2} \tag{2.18b}$$

$$\dot{\beta} = \frac{-v_x v_y\dot{v}_x + (v_x^2 + v_z^2)\dot{v}_y - v_y v_z\dot{v}_z}{V^2\sqrt{v_x^2 + v_z^2}} \tag{2.18c}$$

The above equations can be transformed, by replacing v_x, v_y, v_z by the relations in (2.16) and $\dot{v}_x, \dot{v}_y, \dot{v}_z$ by the body force equations in (2.15). The force equations in wind axes are finally described as

$$\dot{V} = -\frac{\bar{q}S}{m}C_D + g(\cos\theta\cos\phi\sin\alpha\cos\beta + \cos\theta\sin\phi\sin\beta - \sin\theta\cos\alpha\cos\beta) \tag{2.19a}$$

$$\dot{\alpha} = -\frac{\bar{q}S}{mV\cos\beta}C_L + \omega_y - \tan\beta(\omega_x\cos\alpha + \omega_z\sin\alpha) + \frac{g}{V\cos\beta}(\cos\theta\cos\phi\cos\alpha + \sin\theta\sin\alpha) \tag{2.19b}$$

$$\dot{\beta} = \frac{\bar{q}S}{mV}C_{Yw} + \omega_x\sin\alpha - \omega_z\cos\alpha + \frac{g}{V}(\cos\theta\sin\phi\cos\beta + \sin\theta\cos\alpha\sin\beta - \cos\phi\cos\theta\sin\alpha\sin\beta) \tag{2.19c}$$

where

$$C_D = -C_X\cos\alpha\cos\beta - C_Y\sin\beta - C_Z\sin\alpha\cos\beta \tag{2.20a}$$

$$C_L = C_X\sin\alpha - C_Z\cos\alpha \tag{2.20b}$$

$$C_{Yw} = -C_X\cos\alpha\sin\beta + C_Y\cos\beta - C_Z\sin\alpha\sin\beta \tag{2.20c}$$

represent the drag, the lift and the sideforce coefficients along the wind axes, respectively. The drag and the lift coefficients acting on a projectile are represented in Figure 2.3.
In an equivalent manner, based on equation (2.12), on the angular velocity vector in (2.6), on the aerodynamic moment vector in (2.14) and on the inertia matrix defined in (2.7), the moment equations are expressed as

$$\dot{\omega_x} = \frac{1}{I_x}(\bar{q}SdC_l - \omega_y\omega_z(I_z - I_y)) \tag{2.21a}$$

$$\dot{\omega_y} = \frac{1}{I_y}(\bar{q}SdC_m - \omega_x\omega_z(I_x - I_z)) \tag{2.21b}$$

$$\dot{\omega_z} = \frac{1}{I_z}(\bar{q}SdC_n - \omega_x\omega_y(I_y - I_x)) \tag{2.21c}$$

The force and moment equations depend on several physical properties like the mass of the vehicle m, the reference diameter d, the reference surface area S, the longitudinal and lateral moments of inertia I_x, I_y and I_z and the gravitational acceleration g. These quantities are measured with good accuracy before the experiment.

2.3.2 Kinematic equations

The attitude of a vehicle in flight is defined as the angular orientation of the body *w.r.t.* Earth fixed axes. There exist several approaches to characterize the attitude, for example Euler angles (ϕ, θ, ψ), represented in Figure 2.4 [Cook (2012)], or quaternions. As in our case we deal with nearly rectilinear or parabolic trajectories, it is reasonable to express the kinematic equations using Euler angles. The rotational kinematic equations express the link between the Euler angle rates (time derivative of Euler angles) and the angular velocity of the vehicle. The detailed relationships of this transformation are presented in Appendix A.2 and have led to the following equations

$$\dot{\phi} = \omega_x + \tan\theta(\omega_y \sin\phi + \omega_z \cos\phi) \tag{2.22a}$$

$$\dot{\theta} = \omega_y \cos\phi - \omega_z \sin\phi \tag{2.22b}$$

$$\dot{\psi} = \frac{\omega_y \sin\phi + \omega_z \cos\phi}{\cos\theta} \tag{2.22c}$$

In some cases, employing the quaternions instead of Euler angles is more appropriate [2]. The relationships between the Euler angles and quaternions are presented in Appendix A.3.

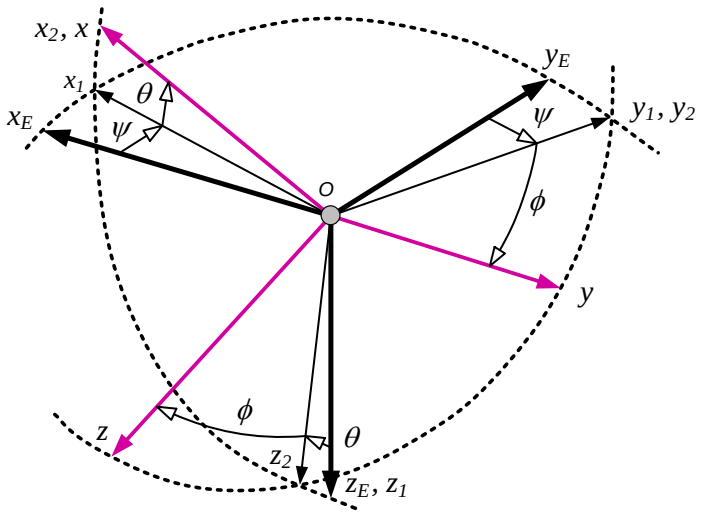

Figure 2.4: Euler angles

Let $(x_E,\ y_E,\ z_E)$ be the coordinates of the center of gravity position of the vehicle *w.r.t.* Earth axes, where $-z_E$ represents the altitude h_E (height above the ground) and $[\dot{x}_E \quad \dot{y}_E \quad \dot{z}_E]_E^T$ be the corresponding velocity vector.
A direction cosine matrix $\mathbf{T}^{EB}$ defines the transformation of the velocity vector from body to Earth axes, parametrized by the attitude angles and given as

$$\mathbf{T}^{EB}(\phi,\theta,\psi) = \begin{bmatrix} \cos\theta\cos\psi & \sin\phi\sin\theta\cos\psi - \sin\psi\cos\phi & \cos\phi\sin\theta\cos\psi + \sin\phi\sin\psi \\ \cos\theta\sin\psi & \sin\phi\sin\theta\sin\psi + \cos\phi\cos\psi & \cos\phi\sin\theta\sin\psi - \sin\phi\cos\psi \\ -\sin\theta & \sin\phi\cos\theta & \cos\phi\cos\theta \end{bmatrix} \tag{2.23}$$

Further information about the construction of the direction cosine matrix can be found in Appendix A.1. Based on this transformation matrix and by writing the translational velocities in body axes

2. The quaternions are used in order to avoid the singularity of the solution. Singularities arise generally when vehicles are fired vertically, which is not the case in the present study.

as in equations (2.16), the translational kinematic equations can be written as

$$\begin{bmatrix} \dot{x}_E \\ \dot{y}_E \\ \dot{z}_E \end{bmatrix}_E = \mathbf{T}^{EB}(\psi,\theta,\phi) \cdot \begin{bmatrix} V\cos\alpha\cos\beta \\ V\sin\beta \\ V\sin\alpha\cos\beta \end{bmatrix}_B$$

and the resulting equations are,

$$\begin{aligned} \dot{x}_E =& V\cos\alpha\cos\beta\cos\theta\cos\psi + V\sin\beta(\sin\phi\sin\theta\cos\psi - \cos\phi\sin\psi) + \\ & V\sin\alpha\cos\beta(\cos\phi\sin\theta\cos\psi + \sin\phi\sin\psi) \qquad (2.24a) \\ \dot{y}_E =& V\cos\alpha\cos\beta\cos\theta\sin\psi + V\sin\beta(\sin\phi\sin\theta\sin\psi + \cos\phi\cos\psi) + \\ & V\sin\alpha\cos\beta(\cos\phi\sin\theta\sin\psi - \sin\phi\cos\psi) \qquad (2.24b) \\ \dot{z}_E =& -V\cos\alpha\cos\beta\sin\theta + V\sin\beta\sin\phi\cos\theta + V\sin\alpha\cos\beta\cos\phi\cos\theta \qquad (2.24c) \end{aligned}$$

2.4 Aerodynamic coefficients

In the case of a vehicle in flight, its behaviour is directly influenced by initial and exterior conditions, such as temperature, pressure, presence of wind, as well as the physical properties of the body (in terms of mass, center of gravity and inertia). All these conditions have an effect on the aerodynamic coefficients. The importance of estimating them lies in the representation of aerodynamic characteristics of a vehicle. Aerodynamic coefficients are the parameters describing and connecting forces and moments acting on the vehicle to angles (α, β) and velocities ($\mathbf{V}$ and $\boldsymbol{\omega}$). Generally, they depend of the flight condition variables such as the velocity, incidence angles, angular rates or accelerations. The incidence angles α and β can be defined as function of the total angle of attack α_t, represented in Figure 2.2, given by

$$\alpha_t(\alpha,\beta) = \arccos(\cos\alpha\cos\beta) \qquad (2.25)$$

It is also important to represent the aerodynamic phenomena as adimensional coefficients. This facilitates the comparison of aerodynamic data between distinct vehicle configurations and allows to interpret its values independently of the vehicle's architecture or experimental conditions. In that respect, the global coefficients for rigid vehicles in flight can be characterized as a function of nondimensional quantities as follows

$$C_i(M,\alpha,\beta,\boldsymbol{\omega},...)$$

where $i = X,Y,Z,l,m,n$ in body frame and $i = D,Yw,L,l,m,n$ in wind frame.
These global aerodynamic coefficients are nonlinear functions of the Mach number, the incidence angles and angular velocities. They also depend on stability derivatives, representing the change in forces and moments *w.r.t.* a variable variation. They are divided in three groups [Klein and Morelli (2006)], associated to velocity quantities (V, α or β), to angular velocities (ω_x, ω_y or ω_z) and unsteady dynamics. In this study, the first two groups are considered and are commonly named the static and dynamic stability derivatives, respectively. Furthermore, in our case, the stability derivatives are assumed to be dependent of the Mach number and the incidence angles.

2.4.1 Force coefficients

The decomposition of the force coefficients depends on the context and on the chosen reference frame. In a wind related reference frame, generally employed in ballistic studies, the drag coefficient

C_D, the lift coefficient C_L and the Magnus force coefficient slope $C_{yp\alpha}$ are considered [3]. The force coefficients relative to a body reference frame are the axial force C_X, the sideforce C_Y and the normal force $C_N = -C_Z$ coefficients.
The wind coordinates in ballistic, also named *aeroballistic wind coordinates*, are different than for aircraft. Since the equations are expressed in the body frame, a transformation matrix dependent on the angle of attack α and the angle of sideslip β from the aeroballistic wind coordinate system to the body coordinate system is used as defined in [Zipfel (2000)] and allows to obtain the following relations:

$$C_X(M,\alpha,\beta) = -C_D(M,\alpha,\beta)\cos\alpha\cos\beta + C_{L\alpha}(M,\alpha,\beta)\,(1-\cos^2\alpha\cos^2\beta) \tag{2.26a}$$

$$C_Y(M,\alpha,\beta) = -C_D(M,\alpha,\beta)\sin\beta - C_{L\alpha}(M,\alpha,\beta)\cos\alpha\cos\beta\sin\beta \tag{2.26b}$$

$$C_N(M,\alpha,\beta) = C_D(M,\alpha,\beta)\sin\alpha\cos\beta + C_{L\alpha}(M,\alpha,\beta)\cos\alpha\sin\alpha\cos^2\beta \tag{2.26c}$$

where $C_{L\alpha} = \dfrac{C_L}{\sin\alpha}$ corresponds to the lift force coefficient slope.
A brief description of two of the main force coefficients can be given as follows [McCoy (1999), Fleck (1998), Stengel (2004)]:

- the **drag coefficient C_D** corresponds to the aerodynamic resistance and is relied to the force which is opposed to the body motion in a fluid. Mathematically, it is the component along the tangent to the trajectory in the opposite direction of the relative body velocity *w.r.t.* the fluid.
- the **lift coefficient C_L** is representative of the force perpendicular to the trajectory induced by the pressure distribution around the vehicle when the angle of attack α is different of zero. In that respect, it is more common to quantify the **lift force coefficient slope** $C_{L\alpha}$ representing the derivative of the lift force coefficient *w.r.t.* the angle of attack α.

2.4.2 Moment coefficients

The vehicle external moment $\mathbf{M}_A$ given in (2.14) can be represented as the sum of the aerodynamic relative to the body (B), the fins (F) and the damping effect (D), as follows [4]

$$\mathbf{M}_A = \mathbf{M}_B + \mathbf{M}_F + \mathbf{M}_D \tag{2.27}$$

This implies that the global moment coefficients, more precisely the roll, pitch and yaw moment coefficients C_l, C_m and C_n in (2.21) can be further developed as function of stability derivatives as

$$\begin{bmatrix} C_l \\ C_m \\ C_n \end{bmatrix} = \begin{bmatrix} 0 \\ C_{m\alpha}\sin\alpha\cos\beta \\ C_{n\beta}\sin\beta \end{bmatrix} + \begin{bmatrix} C_{l\delta}\ \delta \\ 0 \\ 0 \end{bmatrix} + \frac{d}{2V}\begin{bmatrix} C_{lp}\ \omega_x \\ C_{mq}\ \omega_y \\ C_{nr}\ \omega_z \end{bmatrix} \tag{2.28}$$

and can be expressed as

$$C_l(M,\alpha,\beta,\omega_x) = \frac{d}{2V}C_{lp}(M,\alpha,\beta)\ \omega_x + C_{l\delta}(M,\alpha,\beta)\ \delta \tag{2.29a}$$

$$C_m(M,\alpha,\beta,\omega_y) = C_{m\alpha}(M,\alpha,\beta)\sin\alpha\cos\beta + \frac{d}{2V}C_{mq}(M,\alpha,\beta)\ \omega_y \tag{2.29b}$$

$$C_n(M,\alpha,\beta,\omega_z) = C_{n\beta}(M,\alpha,\beta)\sin\beta + \frac{d}{2V}C_{nr}(M,\alpha,\beta)\ \omega_z \tag{2.29c}$$

3. The Magnus force coefficient slope $C_{yp\alpha}$ characterizes the transversal force induced by frictional forces between the flow and the boundary layer produced by unequal pressures on opposite sides of a spinning vehicle under incidence. In these application cases, it can be neglected and the full model is presented in [Theodoulis et al. (2013)].

4. In this study case, only the non negligible aerodynamic coefficients are considered. The global moment descriptions with all the aerodynamic coefficients, such as the Magnus moment coefficient slope $C_{np\alpha}$, are detailed in [Winchenbach et al. (1998)].

In the case of axisymmetric bodies, the following equalities can be applied in a fixed plane coordinate system [Winchenbach (1997)]:

$$\begin{aligned} C_{n\beta}(M,\alpha,\beta) &= -C_{m\alpha}(M,\alpha,\beta) \\ C_{nr}(M,\alpha,\beta) &= \quad C_{mq}(M,\alpha,\beta) \end{aligned} \tag{2.30}$$

The main static and dynamic stability derivatives describing the global moment coefficients are defined below.

- the **roll damping coefficient C_{lp}** can be characterized by a motion generated by frictional or viscosity forces which damps the rotation of a vehicle around its longitudinal axis.
- In the case of a finned vehicle, a rolling moment can be induced if the fin cant angle is not null. In the case of canted fins, the **roll moment coefficient due to fin cant $C_{l\delta}$** produces an increasing spin whereas the roll damping coefficient C_{lp} tends to reduced it. The model characterized by the absence of fins, such as the space probes, it is reasonable to consider that $C_{l\delta}$ is null in this case.
- the **pitch moment coefficient slope $C_{m\alpha}$** or overturning coefficient is the aerodynamic moment coefficient associated with the lift or normal force coefficient. It is representative of the static stability of a vehicle in flight: positive values indicate a statically unstable vehicle while negative values imply a statically stable vehicle.
- the **pitch damping coefficient C_{mq}** arises with the projectile motion damping around a transversal axis. It gives an indication on the dynamic stability of a vehicle in flight: positive values indicate a dynamically unstable vehicle while negative values imply a dynamically stable vehicle. In the present studies, C_{mq} is the pitch damping coefficient sum of two damping moments C_{mq} and $C_{m\dot{\alpha}}$, that produce moments due to transverse angular velocity and due to angular rate of angle of attack $\dot{\alpha}$, respectively. For nearly rectilinear trajectories, the angular rate $\dot{\alpha}$ and ω_y will be equal and the moments can be simplified by combining C_{mq} and $C_{m\dot{\alpha}}$ into a single coefficient sum [McCoy (1999)].

Further details about the static and dynamic stability and their relation with the stability of an automatic control system are given in Appendix B.

2.4.3 Aerodynamic coefficient assumptions

As it was observed, the mathematical model described in equations (2.19, 2.21, 2.22, 2.24) depends on six global aerodynamic coefficients: the drag coefficient C_D, the lift coefficient C_L, the sideforce coefficient C_{Yw}, the roll, pitch and yaw moment coefficients C_l, C_m and C_n.
This model is valid for both applications: an Earth re-entry space probe and a fin stabilized projectile. These global coefficients can be described as function of stability derivatives, as seen in equations (2.26) and (2.29). For the present study, we deal with rectilinear and short flight paths, this implies that some simplifying hypotheses can be applied, as :

- in both applications, the sideforce coefficient C_{Yw} is fixed to zero due to its negligible effects, and the relations defined in (2.30) are considered;
- in the frame of the studied Earth re-entry space vehicle, based on previous studies [Schoenenberger et al. (2009), Winchenbach et al. (2002)], it is well-known that the global coefficients C_L and C_l can be neglected, and therefore, also their stability derivatives.

By taking these assumptions into account, the remaining aerodynamic coefficient vector to be considered for the Earth re-entry space vehicle case (denoted by the superscript $\{\mathbf{sv}\}$) can be defined as

$$\mathbf{C}^{\{\mathbf{sv}\}} = [C_D, C_{m\alpha}, C_{mq}]^T \tag{2.31}$$

In the case of the second application concerning the fin stabilized projectile, all the remaining aerodynamic coefficients will be considered. Therefore, the parameter vector for the Basic Finner projectile (denoted with the superscript $\{\mathbf{bf}\}$) can be defined as

$$\mathbf{C}^{\{\mathbf{bf}\}} = [C_D, C_{L\alpha}, C_{lp}, C_{l\delta}, C_{m\alpha}, C_{mq}]^T \tag{2.32}$$

2.4.4 Descriptions of aerodynamic coefficients

The use of aerodynamic coefficients for the characterization of the behaviour of an object in flight remains one of the oldest and most emergent research project in the fields of exterior ballistic and flight mechanics. Identifying and quantifying these coefficients is a complex and challenging task in the frame of aerodynamic modelling. To be able to estimate all the parameters, the complexity of their descriptions must be coherent with the application but also with the available data. In that respect and depending on the studied vehicle, several aerodynamic model descriptions have been proposed. Some are quite complex, with coupled or decoupled dependencies in variables (Mach number and total angle of attack). However, one must choose the adequate description for each coefficient by considering several constraints:

- the time-invariant parameters describing the coefficient must be of limited number and have a physical interpretation;
- the appropriate use of *a priori* knowledge, coming from the literature, from wind tunnel measurements, aerodynamic predictions codes or a combinaison of these.

The focus lies in the aerodynamic coefficient model.The descriptions must be simple enough for the use but also complete and thus complex to reveal enough information about the system behaviour. For this reason, a balance must be found to obtain a physically interpretable and exploitable model. Thus, the grey box approach is entirely adapted to overcome the limitations of the white and black-box modelling. Grey-box models are established on physical first principles depending on parameters to estimate from measured data [Worden et al. (2007)].

2.4.4.1 Space probe

In the literature, recent studies investigated the aerodynamic coefficient determination of a re-entry space vehicle and by applying system identification techniques [de Divitiis and Vitale (2010), Vitale and Corraro (2012)]. However, the proposed aerodynamic model - described by nonlinear functions of several variables - is valid only for a specific vehicle database obtained by means of wind tunnel tests and CFD predictions. Examples of such descriptions are as follows

$$C_j = \sum_{i=1}^{8} C_i(M, \mathbf{p}_i^{sub}, \mathbf{p}_i^{sup}) g_i(\alpha, \beta, \boldsymbol{\omega})$$

with $j = D, Yw, L, l, m, n$, and depend on multiple stability derivatives C_i. These derivatives are functions of the Mach number and constant aerodynamic parameters $\mathbf{p}_i^{sub} = [K_i^{sub}, m_i, \varepsilon_i, h_{1i}, h_{2i}, \xi_i]$ and $\mathbf{p}_i^{sup} = [K_i^{sup}, a_i, b_i, d_i, e_i]$ which represent the parameters to determine in subsonic and supersonic regimes respectively. Their structure was defined as

$$C_i(M, \mathbf{p}_i^{sub}, \mathbf{p}_i^{sup}) = K_i^{sub} H^{sub}(M) \frac{\sqrt{m_i+\varepsilon_i}(1+h_{1i}M^2+h_{2i}M^3)}{\sqrt{\varepsilon_i+m_i\left|1-M^{\xi_i}\right|^2}} + K_i^{\sup} H^{\sup}(M) \frac{1+a_i M^{d_i}}{1+b_i M^{e_i}} \tag{2.33}$$

where

$$H^{sub}(M) = \frac{\tanh 50(1-M)+1}{2}; \quad H^{\sup}(M) = \frac{\tanh 50(M-1)+1}{2}$$

As it can be noted, the stability derivatives C_i are only functions of the Mach number and without any physical interpretation of the model parameters. Moreover, the aerodynamic model expressed in the previous equation is too complex to be estimated based on free flight data [5].
For these reasons, in the case of a space probe, description of the aerodynamic coefficients was obtained by use of polynomials and polynomial splines, as proposed below.

- The drag coefficient C_D can be represented as a function of the Mach number and the incidence angles (α, β) as follows

$$\begin{aligned} C_D(M,\alpha,\beta) = \; & C_{D0} + C_{D1}\ M + C_{D2}\ M^2 + C_{D3}\ \sin^2\alpha_t + C_{D4}\ \sin^4\alpha_t + \\ & C_{D5}\ M\ \sin\alpha_t \end{aligned} \tag{2.34}$$

  where α_t is defined in equation (2.25).
  This description was constructed based on an equation existing in the literature [Dutta et al. (2008), Winchenbach et al. (1998)] and by adapting the model to the considered application. Indeed, the last term, $C_{D5}\ M \sin\alpha_t$, in equation (2.34) was added in order to respect the *a priori* knowledge of the drag coefficient, obtained through CFD predictions.

As it can be noted in equations (2.29b-2.29c), the coefficients $C_{m\alpha}$ and C_{mq} can be represented as a function of the Mach number and the incidence angles (α and β).

- The pitch moment coefficient slope $C_{m\alpha}$ can be given as

$$C_{m\alpha}(M,\alpha,\beta) = C_{m\alpha 0} + C_{m\alpha 1}\ M + C_{m\alpha 2}\ M^2 + C_{m\alpha 3}\ \sin^2\alpha_t + C_{m\alpha 4}\ \sin^4\alpha_t \tag{2.35}$$

- The description of the pitch damping coefficient C_{mq} can be expressed as [Schoenenberger et al. (2009)]

$$C_{mq}(M,\alpha,\beta) = C_{mq0} + C_{mq1}\ M^* + C_{mq2}\ M^{*2} + C_{mq3}\ \sin^2\alpha_t + C_{mq4}\ \sin^4\alpha_t \tag{2.36}$$

  where $M^* = M - M_{ref}$ with $M_{ref} = 2.5$ a constant representing a reference Mach number.

  However, the polynomial description of the pitch damping coefficient in (2.36) was better adapted for total angles of attack α_t less than 10 degrees. In the case of larger α_t, it has been noticed that this coefficient was highly nonlinear and a polynomial representation was not suitable enough. To avoid this drawback, the following description of the pitch damping coefficient is proposed:

$$\begin{aligned} C_{mq}(M,\alpha,\beta) = \; & C_{mq0} + C_{mq1}\ M^* + C_{mq2}\ M^{*2} + C_{mq3}\ \sin^2\alpha_t + C_{mq4}\ \sin^4\alpha_t \\ & + D_\alpha\ (\alpha_t - \bar{\alpha}_t)_+^2 \end{aligned} \tag{2.37}$$

  where

$$(\alpha_t - \bar{\alpha}_t)_+^2 = \begin{cases} (\alpha_t - \bar{\alpha}_t)^2 & \alpha_t \geq \bar{\alpha}_t \\ 0 & \alpha_t < \bar{\alpha}_t \end{cases}.$$

  The last term in (2.37) represents the inclusion of a spline function defined for total angles of attack superior to $\bar{\alpha}_t = 10$ degrees and D_α is a constant parameter quantifying the spline contribution [Klein and Morelli (2006)]. Indeed, spline functions are expressed as piecewise polynomials of a given degree defined only on selected intervals.

5. In the mentioned papers, the model parameters were quantified by means of CFD predictions and wind tunnel tests. It is well-known in exterior ballistic domain, that it is very difficult to characterize the dynamic stability, for example, through these tools.

2.4.4.2 Projectile

The aerodynamic coefficient descriptions must be chosen carefully as it depends on the vehicle architecture, the velocity regime, etc. For the projectile, the descriptions existing in the literature seem less complex than in the case of re-entry space vehicle. Indeed, they are usually represented by second degree polynomials as a function of incidence angles [Hathaway (1976), McCoy (1999)] or only as a function of the Mach number [Dutta et al. (2008)]. Complete descriptions, as functions of Mach number and incidence angles, can be found in [Winchenbach et al. (1998)] and expressed as

$$C_D(M,\alpha,\beta) = C_{D0} + C_{D1}\ M + C_{D2}\ M^2 + C_{D3}\ \sin^2\alpha_t + C_{D4}\ \sin^4\alpha_t \tag{2.38}$$

$$C_{L\alpha}(M,\alpha,\beta) = C_{L\alpha0} + C_{L\alpha1}\ M + C_{L\alpha3}\ \sin^2\alpha_t + C_{L\alpha4}\ \sin^4\alpha_t \tag{2.39}$$

$$C_{lp}(M,\alpha,\beta) = C_{lp0} + C_{lp1}\ M + C_{lp3}\ \sin^2\alpha_t \tag{2.40}$$

$$C_{l\delta}(M,\alpha,\beta) = C_{l\delta0} + C_{l\delta1}\ M + C_{l\delta3}\ \sin^2\alpha_t \tag{2.41}$$

$$C_{m\alpha}(M,\alpha,\beta) = C_{m\alpha0} + C_{m\alpha1}\ M + C_{m\alpha2}\ M^2 + C_{m\alpha3}\ \sin^2\alpha_t + C_{m\alpha4}\ \sin^4\alpha_t \tag{2.42}$$

$$C_{mq}(M,\alpha,\beta) = C_{mq0} + C_{mq1}\ M + C_{mq3}\ \sin^2\alpha_t + C_{mq4}\ \sin^4\alpha_t \tag{2.43}$$

2.5 Output equations

The output variables considered herein correspond to measurements obtained during a free flight test and more precisely to radar and 3D magnetometer data, as mentioned in Chapter 1. The first output variable corresponds to the velocity of the vehicle in flight, directly obtained from the Doppler radar.
Concerning the magnetometers, the three-axis sensor measures the projection of the Earth magnetic field on the sensor axes. The output equations relative to the 3D magnetometer signals are given as follows [Titterton (2004)]

$$\mathbf{H}_m = \mathbf{S}\cdot\mathbf{D}\cdot\mathbf{T}^{BE}(\phi,\theta,\psi)\cdot\mathbf{H}_E + \mathbf{offset} \tag{2.44}$$

where

$$\mathbf{S} = \begin{bmatrix} S_x & 0 & 0 \\ 0 & S_y & 0 \\ 0 & 0 & S_z \end{bmatrix},\quad \mathbf{D} = \begin{bmatrix} D_{xx} & D_{xy} & D_{xz} \\ D_{yx} & D_{yy} & D_{yz} \\ D_{zx} & D_{zy} & D_{zz} \end{bmatrix},\quad \mathbf{offset} = \begin{bmatrix} off_x \\ off_y \\ off_z \end{bmatrix} \tag{2.45}$$

As it can be observed, equation (2.44) is given in a sensor relative reference frame which can be non-orthogonal. Indeed, the transformation between the sensor related frame to the orthogonal body reference frame is accomplished through the use of the matrices **S** and **D**, and the **offset** vector. These matrices and vector represent the sensor calibration factors, measured before each free flight test. As this can be considered as known quantities and for simplification reasons, we will express the magnetometer measurements in the body reference frame as follows

$$\mathbf{H}_{body} = \mathbf{T}^{BE}(\phi,\theta,\psi)\cdot\mathbf{H}_E \tag{2.46}$$

with

$$\mathbf{H}_{body} = (\mathbf{S}\cdot\mathbf{D})^{-1}\cdot(\mathbf{H}_m - \mathbf{offset}) \tag{2.47}$$

The transformation matrix $\mathbf{T}^{BE}$ from Earth to body axes is the inverse matrix of $\mathbf{T}^{EB}$ defined in (2.23). The three-dimensional vector $\mathbf{H}_E = \left(H_x^E, H_y^E, H_z^E\right)$, expressed in an Earth reference frame, corresponds to the Earth magnetic field values, supposed herein to be known and constant,

at the experimental test location. Therefore, the magnetometer measurements in body axes are given by

$$H_{x,body}(t_k) = \cos\theta_k \cos\psi_k \; H_x^E + \cos\theta_k \sin\psi_k \; H_y^E - \sin\theta_k \; H_z^E + v_2(t_k) \tag{2.48a}$$

$$H_{y,body}(t_k) = (\sin\phi_k \sin\theta_k \cos\psi_k - \cos\phi_k \sin\psi_k) \; H_x^E + (\sin\phi_k \sin\theta_k \sin\psi_k + \cos\phi_k \cos\psi_k) \; H_y^E + \sin\phi_k \cos\theta_k \; H_z^E + v_3(t_k) \tag{2.48b}$$

$$H_{z,body}(t_k) = (\cos\phi_k \sin\theta_k \cos\psi_k + \sin\phi_k \sin\psi_k) \; H_x^E + (\cos\phi_k \sin\theta_k \sin\psi_k - \sin\phi_k \cos\psi_k) \; H_y^E + \cos\phi_k \cos\theta_k \; H_z^E + v_4(t_k) \tag{2.48c}$$

where ϕ_k, θ_k, and ψ_k represent the values of the Euler angles at the measurement time t_k, with $k \in 1..., N$, and the measurement noises $v_j(t_k), j = 1, \ldots, 4$.

2.6 Concluding remarks

In this study, the behaviour of a vehicle in flight can be expressed through twelve nonlinear differential equations, while the system output equations correspond to radar and magnetometer measurements recorded during a free flight test. The state and output equations are summarized below.

Wind axes force equations:

$$\dot{V} = -\frac{\bar{q}S}{m} C_D + g(\cos\theta\cos\phi\sin\alpha\cos\beta + \cos\theta\sin\phi\sin\beta - \sin\theta\cos\alpha\cos\beta) \tag{2.49a}$$

$$\dot{\alpha} = -\frac{\bar{q}S}{mV\cos\beta} C_L + \omega_y - \tan\beta(\omega_x\cos\alpha + \omega_z\sin\alpha) + \frac{g}{V\cos\beta}(\cos\theta\cos\phi\cos\alpha + \sin\theta\sin\alpha) \tag{2.49b}$$

$$\dot{\beta} = \frac{\bar{q}S}{mV} C_{Yw} + \omega_x\sin\alpha - \omega_z\cos\alpha + \frac{g}{V}(\cos\theta\sin\phi\cos\beta + \sin\theta\cos\alpha\sin\beta - \cos\phi\cos\theta\sin\alpha\sin\beta) \tag{2.49c}$$

Moment equations:

$$\dot{\omega_x} = \frac{1}{I_x}(\bar{q}SdC_l - \omega_y\omega_z(I_z - I_y)) \tag{2.50a}$$

$$\dot{\omega_y} = \frac{1}{I_y}(\bar{q}SdC_m - \omega_x\omega_z(I_x - I_z)) \tag{2.50b}$$

$$\dot{\omega_z} = \frac{1}{I_z}(\bar{q}SdC_n - \omega_x\omega_y(I_y - I_x)) \tag{2.50c}$$

Rotational kinematic equations:

$$\dot{\phi} = \omega_x + \tan\theta(\omega_y\sin\phi + \omega_z\cos\phi) \tag{2.51a}$$

$$\dot{\theta} = \omega_y\cos\phi - \omega_z\sin\phi \tag{2.51b}$$

$$\dot{\psi} = \frac{\omega_y\sin\phi + \omega_z\cos\phi}{\cos\theta} \tag{2.51c}$$

Translational kinematic equations:

$$\dot{x}_E = V\cos\alpha\cos\beta\cos\theta\cos\psi + V\sin\beta(\sin\phi\sin\theta\cos\psi - \cos\phi\sin\psi) + V\sin\alpha\cos\beta(\cos\phi\sin\theta\cos\psi + \sin\phi\sin\psi) \tag{2.52a}$$

$$\dot{y}_E = V\cos\alpha\cos\beta\cos\theta\sin\psi + V\sin\beta(\sin\phi\sin\theta\sin\psi + \cos\phi\cos\psi) + V\sin\alpha\cos\beta(\cos\phi\sin\theta\sin\psi - \sin\phi\cos\psi) \tag{2.52b}$$

$$\dot{z}_E = -V\cos\alpha\cos\beta\sin\theta + V\sin\beta\sin\phi\cos\theta + V\sin\alpha\cos\beta\cos\phi\cos\theta \tag{2.52c}$$

Radar output equation:

$$y_1(t_k) \;=\; V(t_k) + v_1(t_k) \tag{2.53}$$

Body axes 3D magnetometer equations:

$$y_2(t_k) \;= H_{x,body}(t_k) = \cos\theta_k \cos\psi_k \;H_x^E + \cos\theta_k \sin\psi_k \;H_y^E - \sin\theta_k \;H_z^E + v_2(t_k) \tag{2.54a}$$

$$y_3(t_k) \;= H_{y,body}(t_k) = (\sin\phi_k \sin\theta_k \cos\psi_k - \cos\phi_k \sin\psi_k) \;H_x^E + (\sin\phi_k \sin\theta_k \sin\psi_k + \cos\phi_k \cos\psi_k) \;H_y^E + \sin\phi_k \cos\theta_k \;H_z^E + v_3(t_k) \tag{2.54b}$$

$$y_4(t_k) \;= H_{z,body}(t_k) = (\cos\phi_k \sin\theta_k \cos\psi_k + \sin\phi_k \sin\psi_k) \;H_x^E + (\cos\phi_k \sin\theta_k \sin\psi_k - \sin\phi_k \cos\psi_k) \;H_y^E + \cos\phi_k \cos\theta_k \;H_z^E + v_4(t_k) \tag{2.54c}$$

Let us suppose that we have access to a series of free flight measurements ${}^i\mathbf{y}$, $i = 1, ..., n_s$, with n_s the number of experimental tests. Based on this data, we intend to estimate the aerodynamic coefficients. As already seen in equations (2.34, 2.35, 2.37) or (2.38-2.43), these coefficients are dependent on several unknown parameters. The parameter sets to be estimated, $\mathbf{p}^{\{sv\}}$ and $\mathbf{p}^{\{bf\}}$ for the space vehicle and the Basic Finner projectile cases respectively, are defined as

$$\mathbf{p}^{\{sv\}} = \begin{bmatrix} \mathbf{x}_0, \\ \mathbf{p}_D, \\ \mathbf{p}_{m\alpha}, \\ \mathbf{p}_{mq} \end{bmatrix} = \begin{bmatrix} V_0, \alpha_0, \beta_0, \omega_{x0}, \omega_{y0}, \omega_{z0}, \phi_0, \theta_0, \psi_0, \\ C_{D0}, C_{D1}, C_{D2}, C_{D3}, C_{D4}, C_{D5}, \\ C_{m\alpha 0}, C_{m\alpha 1}, C_{m\alpha 2}, C_{m\alpha 3}, C_{m\alpha 4}, \\ C_{mq0}, C_{mq1}, C_{mq2}, C_{mq3}, C_{mq4}, D_\alpha \end{bmatrix} \tag{2.55}$$

where $\mathbf{p}_D$, $\mathbf{p}_{m\alpha}$ and $\mathbf{p}_{mq}$ correspond to the unknown parameter vectors for the proposed drag, overturning and pitch damping coefficient descriptions of the space probe model in equations (2.34, 2.35, 2.37) respectively, and

$$\mathbf{p}^{\{bf\}} = \begin{bmatrix} \mathbf{x}_0, \\ \mathbf{p}_D, \\ \mathbf{p}_{L\alpha} \\ \mathbf{p}_{lp} \\ \mathbf{p}_{l\delta} \\ \mathbf{p}_{m\alpha} \\ \mathbf{p}_{mq} \end{bmatrix} = \begin{bmatrix} V_0, \alpha_0, \beta_0, \omega_{x0}, \omega_{y0}, \omega_{z0}, \phi_0, \theta_0, \psi_0, \\ C_{D0}, C_{D1}, C_{D2}, C_{D3}, C_{D4}, \\ C_{L\alpha 0}, C_{L\alpha 1}, C_{L\alpha 3}, C_{L\alpha 4}, \\ C_{lp0}, C_{lp1}, C_{lp3}, \\ C_{l\delta 0}, C_{l\delta 1}, C_{l\delta 3}, \\ C_{m\alpha 0}, C_{m\alpha 1}, C_{m\alpha 2}, C_{m\alpha 3}, C_{m\alpha 4}, \\ C_{mq0}, C_{mq1}, C_{mq3}, C_{mq4} \end{bmatrix} \tag{2.56}$$

where $\mathbf{p}_D$, $\mathbf{p}_{L\alpha}$, $\mathbf{p}_{lp}$, $\mathbf{p}_{l\delta}$, $\mathbf{p}_{m\alpha}$ and $\mathbf{p}_{mq}$ correspond to the unknown parameter vectors for the proposed aerodynamic coefficient descriptions of the projectile in equations (2.38-2.43) respectively.

The vehicle is considered in free flight only at the position or time where the model is flying without anymore interaction with the sabot petals. For this reason and with the exception of the center of gravity positions, the initial conditions of the state variables $\mathbf{x}_0$ are considered to be unknown and must be equally estimated. Indeed, x_{E0} is determined from radar data and $y_{E0} = z_{E0}$ are fixed to zero due to the nearly rectilinear trajectory hypothesis. Figure 2.5 shows an example of the velocity and magnetometer signals evolution of a spinning projectile and indicates the initial time to consider for assuming that the vehicle is in free flight.

Table 2.2 summarizes the main components of the mathematical model, i.e. the time-dependent state and output variables, as well as the considered aerodynamic coefficients and parameters to estimate.

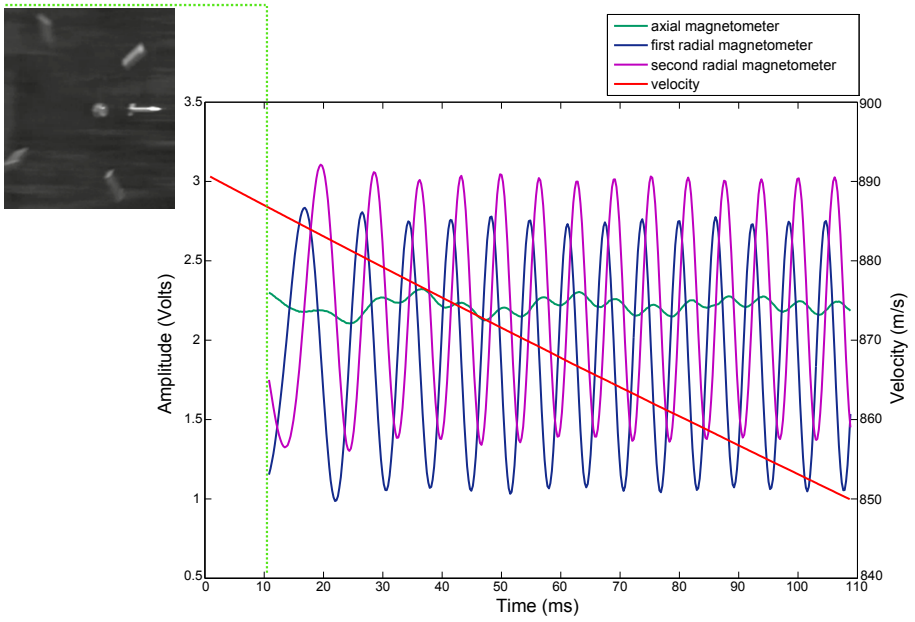

Figure 2.5: Free-flight measurements of a spinning projectile ($M0 = 2.63$, $\alpha 0 = 4°$, $\delta = 2°$)

state variables	$\mathbf{x}(t)$	$V, \alpha, \beta, \omega_x, \omega_y, \omega_z, \phi, \theta, \psi, x_E, y_E, z_E$	
initial state variables to estimate	$\mathbf{x}_0$	$V_0, \alpha_0, \beta_0, \omega_{x0}, \omega_{y0}, \omega_{z0}, \phi_0, \theta_0, \psi_0$	
output variables	$\mathbf{y}(t)$	$V, H_{x,body}, H_{y,body}, H_{z,body}$	
aerodynamic coefficients	$\mathbf{C}(\mathbf{x}(t), \mathbf{p}_a)$	$C_D, C_{m\alpha}, C_{mq}$	$C_D, C_{L\alpha}, C_{lp}, C_{l\delta}, C_{m\alpha}, C_{mq}$
parameters to be estimated	$\mathbf{p}$	$\mathbf{x}_0, \mathbf{p}_D, \mathbf{p}_{m\alpha}, \mathbf{p}_{mq}$	$\mathbf{x}_0, \mathbf{p}_D, \mathbf{p}_{L\alpha}, \mathbf{p}_{lp}, \mathbf{p}_{l\delta}, \mathbf{p}_{m\alpha}, \mathbf{p}_{mq}$
		Space probe	**Projectile**

Table 2.2: Considered variables and parameters in the mathematical model

The system identification problem is challenging mainly due to the followings aspects:

- the nonlinear model structure describing the behaviour of the vehicle in flight and expressed in (2.49-2.54);
- the nonlinear dependency of the aerodynamic coefficients on several state variables (V, α, β) as seen in equations (2.34, 2.35, 2.37) or (2.38-2.43);
- the constraints imposed by the experimental conditions in terms of initial Mach number $M0$ and initial angle of attack $\alpha 0$, as it was observed in Chapter 1;
- the additional estimation of the initial state variables $\mathbf{x}_0$, along with the aerodynamic coefficient parameters;
- the applications presented herein are characterized by the absence of an input signal ($u(t) = 0$) and then, the identification has to be performed without any signal excitation.

Under all these conditions, the parameter estimation step must be processed with caution.
In the present study, the model structure describing the behaviour of a vehicle in free flight is defined by Newton's and Euler's laws and can be compared to a knowledge-based model. It is based on flight mechanic equations and contains aerodynamic coefficients with a physical meaning. These latter are described in polynomial forms depending on state variables and aerodynamic

parameters. Aerodynamic coefficient descriptions are available in the literature, however from the expertise in the field and after testing different descriptions, a modified model structure was proposed.
These representations were adapted from existing descriptions in the literature and *a priori* knowledge of the system. With the integration of parametrized functions of the aerodynamic coefficients, which must be determined from free flight measurements, it is more convenient to considered the model as a semi-physical model [Sjöberg et al. (1995), Oussar and Dreyfus (2001)]. The model was then obtained via a grey-box model approach. Because grey-box approach can be used for different objectives, like for diagnostic or control [Defranoux (2001)], the study to be undertaken concerned the improvement of the physical parameters knowledge of the system.
To estimate the unknown parameters from free flight data, an identification procedure adapted to the study case was proposed and presented in the following chapter. This problem is then associated to an inverse problem and as it remains difficult to solve, the defined procedure is composed of several analysis to guide the estimation step, particularly identifiability analysis to evaluate the feasibility of the estimation.

Chapter 3

Aerodynamic parameter identification

The determination of the aerodynamic coefficients from free flight data can be formulated as a system identification problem. It is an inverse problem which depends on the chosen model structure, but equally on the quantity and quality of the measured data. Thus, taking into account the proposed model structure, presented in Chapter 2, the question is whether or not the measured data is sufficient for the estimation of the unknown model parameters. The underlying question is then the identifiability of these parameters.
The identification procedure, employed in this research project, is composed of several steps from the construction of the mathematical model to the estimation of the unknown parameters. An intermediary step is the identifiability analysis and covers the a priori and a posteriori identifiability analyses of the parameters. The current chapter presents the main details about the identification procedure, the a priori knowledge integrated into the study, the implementation of the mathematical model in a simulation environment. Afterwards it focuses on the identifiability of the unknown parameter set. As mentioned previously, the unknown parameter set is composed herein of the time-invariant model parameters describing the aerodynamic coefficients and the initial conditions of the state variables. The estimation process employed for the aerodynamic parameter determination is composed of several steps and is detailed at the end of the chapter.

3.1 Inverse problem

The notion of inverse problem appears when unknown physical parameters $\mathbf{p}$ cannot be directly measured. For this reason, it is generally convenient to proceed to the measurement of other variables linked to the unknown parameters, $\mathbf{y} = f(\mathbf{p})$. The complexity of the inverse problem depends thus on the model structure, but also on the quantity and quality of the measured data. In practice, the mathematical resolution of such problems can be difficult and requests a rigorous analysis, as they may be ill-posed [Hadamard (1902)]. By definition, the problem $\mathbf{y} = f(\mathbf{p})$ is well-posed, in the Hadamard sense, if it satisfies the following three conditions:

- **Existence of the solution:** there exists a solution $\mathbf{p} \in \mathbb{P}$ for each $\mathbf{y} \in \mathbb{R}^{n_y}$;
- **Uniqueness of the solution:** the solution is unique in $\mathbb{P}$;
- **Continuity of the solution:** the dependency of $\mathbf{p}$ with respect to $\mathbf{y}$ is continuous, i.e. when the observation error $\delta\mathbf{y}$ tends toward zero, the induced solution error $\delta\mathbf{p}$ also tends toward zero.

The first condition expresses the consistency of the mathematical model, while the second condition formulates a coherent context characterising the system. Indeed, if this latter condition is not satisfied, it means that several parameter sets can reproduce the same observations. Concerning the third condition, it corresponds to a necessary but not sufficient condition to obtain the stability of the solution. It is important to mention the conditions of a well-posed inverse problem, as these conditions are directly related to the identifiability analyses.
Grey-box model identification of a vehicle in free flight can be defined as the determination of a model structure and the estimation of the unknown parameters contained in the chosen model structure by integrating at different levels of the identification procedure *a priori* knowledge of the system [Bohlin (2006)]. In both steps, we deal with an inverse problem which, due to the system complexity and the constraints imposed by the input/output measurements, can be impossible to solve if it is ill-posed or difficult to solve if it is ill-conditioned. These two inverse problems – choice of model structure and parameter estimation – correspond respectively to two distinct concepts: distinguishability and identifiability [Walter and Pronzato (1997)]. As herein the model structure is derived from basic physical principles and assumed known, the problem is then reduced to the parameter identification of a grey-box model.

3.2 Identification procedure

The grey-box identification procedure proposed herein and presented in Figure 3.1 was adapted from [Franceschini and Macchietto (2008), Bohlin (2006), Walter and Pronzato (1997), Dobre et al. (2008)] and intends the determination of the unknown parameter set. This procedure is composed of several steps introduced below:

1. Defining the model structure and assessing its theoretical or *a priori* identifiability [Walter and Pronzato (1997)] deals with the possibility to give a unique value to each parameter of the chosen model structure. This analysis investigates the question of existence and uniqueness of a solution to the parameter estimation problem, in an idealized framework, where the system and model have identical structure (no characterization error), data are noise-free, and input signals and measurement times can be chosen at will. This is only a necessary condition which cannot guarantee successful parameter estimation from real data, but allows to define a new parameter set $\mathbf{p}_1$ including the locally theoretically identifiable parameters.

2. A prior analysis, generally based on literature, must be carried out in order to provide initial guess of the model parameters $\mathbf{p}_1$.

3. Model implementation into a simulation environment.

4. When the model is found to be *a priori* identifiable, an admissible experiment has to be selected in order to collect the experimental data. In that direction, optimal input design algorithms can be applied in order to choose the best input signal for the parameter estimation step.

5. The *a posteriori* identifiability is a particular case of output distinguishability for a finite collection of noise-free observations and a given input signal. Taking into account experimental conditions, the sensitivity of output variables with respect to each parameter in the parameter set $\mathbf{p}_1$ is computed. Based on the sensitivity of the output variables and numerical properties of the empirical Fisher Information matrix, we can select *a posteriori* identifiable parameter subset $\mathbf{p}_2$.

6. The last step deals with the parameter estimation. The estimation criterion, defined for the selected data series i, is given as follows:

$$\mathrm{J}_i(\mathbf{p}_2) = \sum_{k=1}^{N_i} \sum_{j=1}^{n_y} e_{i,j}(t_k, \mathbf{p}_2)^T \cdot e_{i,j}(t_k, \mathbf{p}_2) \tag{3.1}$$

with $e_{i,j}(t_k, \mathbf{p}_2)$ the output error defined as

$$e_{i,j}(t_k, \mathbf{p}_2) = y_{i,j}(t_k) - \hat{y}_{i,j}(t_k, \mathbf{p}_2) \tag{3.2}$$

where t_k is a specific measurement time-instant, with $k \in 1, ..., N$, $y_{i,j}(t_k)$, $i = 1, ..., n_s$ and $j = 1, ...n_y$, represents the data measured during the i^{th} free flight experiment, $\hat{y}_{i,j}(t_k, \mathbf{p}_2)$ the corresponding simulated model output signals and $e_{i,j}(t_k, \mathbf{p}_2)|k = 1, ..., N$, is the output error.

3.3 Prior knowledge and model implementation

The use of knowledge about the process makes it possible to improve the identification of the unknown parameter set. Depending on the nature of the available knowledge, this information can be integrated into several steps of the system identification procedure. Three types of knowledge can be distinguished and are explained herein, and more widely detailed in the literature, see e.g. [Defranoux (2001)]:

- the *structural knowledge*, based on physical laws describing the behaviour of the vehicle in flight, namely the Newton's and Euler's laws to construct the mathematical model.
- the *behavioural knowledge*, which is related to the vehicle behaviour such as the spin rate, the position of vehicle in space and the vehicle stability. Examples of such knowledge are the rectilinear trajectories in the projectile case (meaning that the coordinates of the center of gravity of the vehicle y_E and z_E will be close to zero) or the roll motion of the projectile induced by the fin cant angle. Of course, this information is dependent on the studied vehicle and is linked to the expertise in the ballistic/aerodynamic domains.
- the *parametric knowledge*, reflecting the possibility to give an initial guess to the unknown parameter set of the considered model. The parameter initialisation of the aerodynamic coefficient models can be crucial. It is based on literature results, CFD predictions, empirical or semi-empirical codes and/or wind tunnel tests or a combination of these. All these studies can give preliminary information in terms of order of magnitude and tendency of the aerodynamic coefficients.

While the structural knowledge is mainly involved in the first step of the identification procedure, the parametric knowledge gives an initialisation of the model parameters and will thus be utilized in all the other steps (from step two to six) of the above mentioned procedure. The behavioural knowledge allows to check if the simulated evolution of the state variables (through the use of the mathematical model implemented into a simulation environment) is coherent with the knowledge of the system, and is exploited in the last three steps of the identification procedure.

The mathematical model describing the behaviour of a vehicle in free flight defined in Chapter 2 was implemented into a simulation environment, more precisely under Matlab/Simulink© [1]. The kernel

1. Simulink builds upon Matlab©, MathWorks, Inc

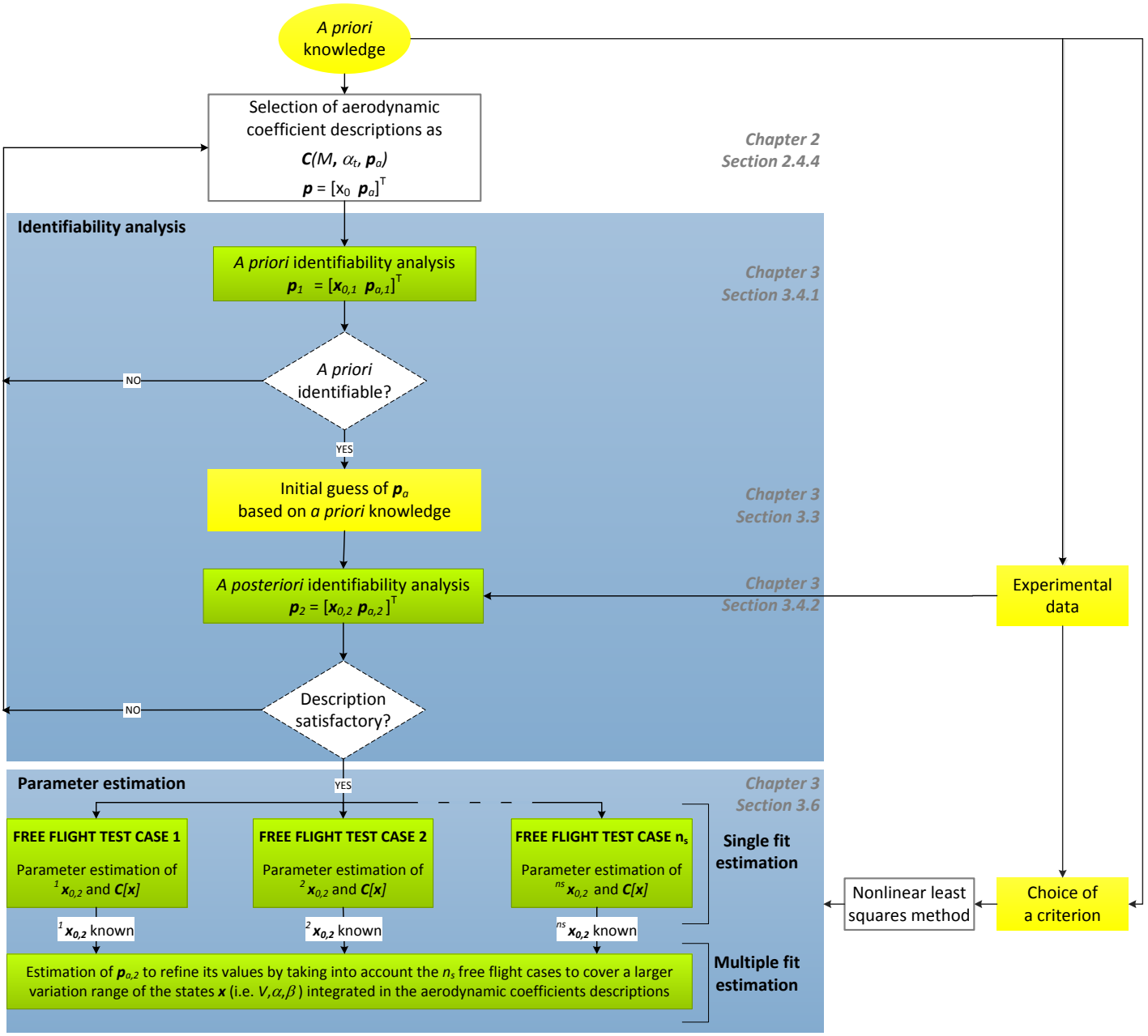

Figure 3.1: Identification procedure

of the developed code is the 6 Degrees of Freedom (6DOF) model presented in equations (2.49-2.52), integrating equally the aerodynamic coefficient descriptions *w.r.t.* the studied vehicles. The model output variables correspond to free flight measurement signals, as defined in equations (2.53) and (2.54). The Matlab/Simulink block diagram is presented in Figure 3.2 and the description of each block is detailed in Table 3.1. The selected start and stop times in the simulator, as well as time-instants are equivalent to those of the magnetometer measurements.

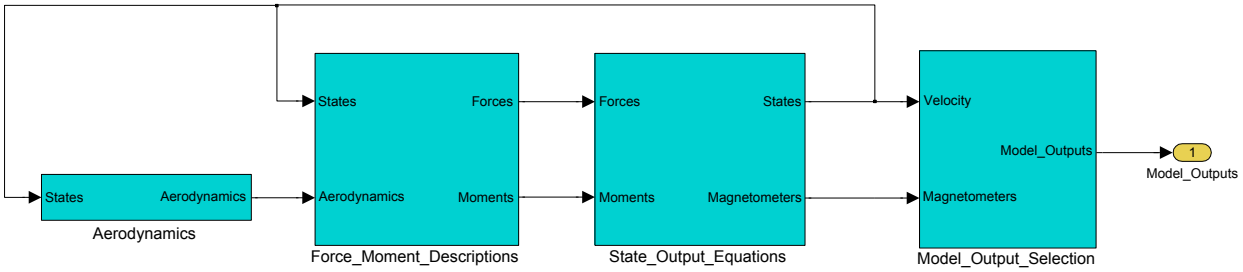

Figure 3.2: Matlab/ Simulink block diagram

Blocks	Functions	Equations
Aerodynamics	- Define the state variables $(V, \alpha, \beta, \omega_x, \omega_y, \omega_z, \phi, \theta, \psi, x_E, y_E, z_E)$	
	- Calculate the main physical variables (M, α_t)	(1.1, 2.25)
	- Describe the aerodynamic coefficients as functions of the M and α_t for:	
	$*$ the space vehicle model	(2.34, 2.35, 2.37)
	or	
	$*$ the Basic Finner projectile	(2.38-2.43)
Force_Moment_Descriptions	- Express the global force and moment coefficients	(2.26, 2.29)
State_Output_Equations	- Describe the state equations	(2.49-2.52)
	- Write the magnetometer equations	(2.54)
Model_Output_Selection	- Selection of the considered model outputs:	
	$*$ velocity	(2.53)
	$*$ 3D magnetometer	(2.54)

Table 3.1: Functions associated to Simulink blocks

3.4 Identifiability analysis

In many applications, model parameters are not directly measurable and can only be evaluated by means of their influences on the measured data. A prerequisite of the parameter identification from measured data is to know if the unknown parameters can be estimated from the defined model structure and observations. This question can be evaluated at different levels through parameter identifiability analysis. In the literature, several classifications of identifiability exist, having often similar terminologies with different definitions as indexed in [Thomassin (2005), Dobre (2010)]. We refer herein to three classes as described in Figure 3.3: *a priori* identifiability, *a posteriori* identifiability and practical identifiability.
Depending on the model structure, one can have local or global results [2] [Walter and Pronzato (1997)]. Furthermore, *a priori* identifiability is defined in a qualitative manner, by knowing if the model structure is identifiable or not, while *a posteriori* and practical identifiabilities allow to

2. Local and global analyses are defined *w.r.t.* the parameter space.

quantify it with a degree of identifiability [Bastogne (2008)]. For the present study, two classes are analyzed, namely the *a priori* and *a posteriori* identifiability. The last class, practical identifiability, takes into account the noise factor but is generally established for a given estimation criterion [Dochain et al. (1995), Vanrolleghem et al. (1995)]. For that reason, this class of identifiability is often linked to the theory of optimization in mathematics. More details about identifiability analysis can be found in [Dobre (2010)].

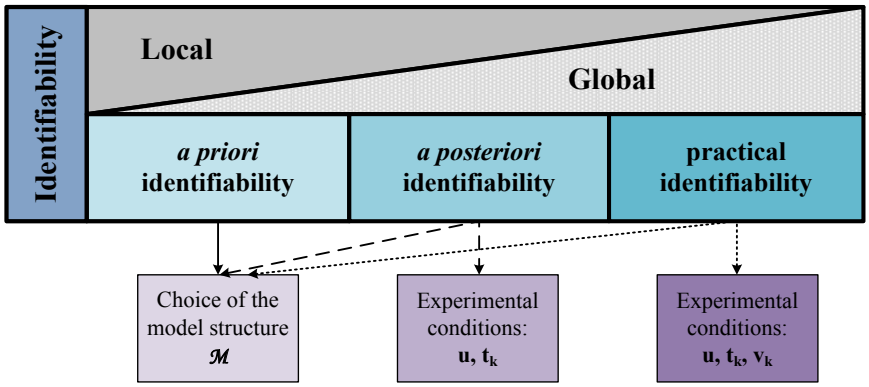

Figure 3.3: Classification of identifiability definitions, where $\mathcal{M}$ denotes the model structure, $\mathbf{u}$ the input signals, t_k the measurement times and v_k the output noise

3.4.1 *A priori* identifiability analysis

The first identifiability class, also known as the theoretical or structural identifiability of model parameters, analyzes the model structure $\mathcal{M}$ in an idealized framework where:

1. the system and model have identical structure (no characterization error);
2. data are noise-free;
3. input signals and measurement times can be chosen at will.

It examines the question of existence of the solution to the parameter estimation problem [Walter and Pronzato (1997)], notion directly related to the first condition of a Hadamard well-posed inverse problem. However, this is only a necessary condition which cannot guarantee successful parameter estimation based on real data.
The *a priori* identifiability condition is defined as follows: given a model structure $\mathcal{M}$, a parameter p_l is *a priori* globally identifiable in $\mathbf{p}^* \in \mathbb{P}$ if $\exists(\mathbf{u}, \mathbf{x}_0) \in \mathbb{U} \times \mathbb{R}^{n_x}$ satisfying [Walter and Pronzato (1997)]:

$$y_{\mathcal{M}}(t_k, \mathbf{p}, \mathbf{u}) = y_{\mathcal{M}}(t_k, \mathbf{p}^*, \mathbf{u}) \ \forall t_k \in \mathbb{T} \Longrightarrow p_l = p_l^* \tag{3.3}$$

with $l \in 1, \ldots, n_p$ and for all $\mathbf{p}^* \in \mathbb{P} \subset \mathbb{R}^{n_p}$.
Respectively, the local *a priori* identifiability tests this condition in a neighbourhood of $\mathbf{p}^*$ for $\mathbf{p}^* \in V(\mathbf{p}^*) \subset \mathbb{R}^{n_p}$. As the *a priori* identifiability is analyzed before experiment, no quantitative values can be associated to $\mathbf{p}^*$, and it is then studied for all the possible values $\mathbf{p}^*$ in $\mathbb{P}$.

Several methods for linear or nonlinear model structures exist to analyze the *a priori* or theoretical identifiability of model parameters and/or initial conditions [Perasso (2009)]. They are based on analytical of algebraic approaches such as state isomorphisms [Peeters and Hanzon (2005)], power series expansions [Walter and Pronzato (1997)] or differential algebra [Audoly et al. (2001), Ljung and Glad (1994), Saccomani et al. (2003)]. By considering that the parameters $\mathbf{p}$ of the model

are a special kind of state variables satisfying $\dot{\mathbf{p}} = 0$, the local theoretical identifiability problem is defined as a particular case of observability. In this sense, Sedoglavic has developed an algorithm for testing local observability, relied on the differential algebra and it is based on the existence of algebraic relations between state variables and successive derivations of the inputs and the outputs [Sedoglavic (2002)]. It was implemented under the symbolic computation software MAPLE and returns the number of non-identifiable parameters and that means that the remaining parameters $\mathbf{p}_1$ are locally theoretically identifiable. A description of this tool as well as an example of the observability test is presented in Appendix C.

3.4.2 *A posteriori* identifiability analysis

The input design and experimental conditions are often subject to technical and/or economical constraints. In such restrictive experimental frameworks, even if a parameter is *a priori* identifiable, it may not be so in practice, due to a lack of information in the available observations. The existence of the solution must then be verified from available data. The second class of identifiability, namely the *a posteriori* identifiability is a particular case of the output distinguishability for a finite collection of noise-free observations and given time instants, input signals and initial conditions, imposed by the experiments. The working assumptions are then defined as:

1. the system and model have identical structure (no characterization error);
2. data are noise-free;
3. input signals, initial conditions and measurement times are imposed by the experimental conditions.

The *a posteriori* identifiability condition can be stated in a general manner as follows: given a model structure $\mathcal{M}$ with given input signals $\mathbf{u}$ and initial conditions $\mathbf{x}_0$, a parameter p_l is *a posteriori* identifiable, if the following condition is satisfied [Walter and Pronzato (1997)]:

$$y_{\mathcal{M}}(t_k, \mathbf{p}, \mathbf{u}) = y_{\mathcal{M}}(t_k, \mathbf{p}^*, \mathbf{u}) \ \forall t_k \in \mathbb{T} \Longrightarrow p_l = p_l^* \tag{3.4}$$

with $l \in 1, \ldots, n_p$ and for almost all $\mathbf{p}^* \in \mathbb{P} \subset \mathbb{R}^{n_p}$. In other words, the objective is to know whether this identical input-output behaviour implies that the parameters $\mathbf{p}$ of the model equal those of the physical process $\mathbf{p}^*$. For nonlinear models, this *a posteriori* identifiability condition is valid only locally in a neighborhood $V(\mathbf{p}^*)$ of the true parameter values. The previous condition can also be expressed as

$$\sum_{l=1}^{n_p} \underbrace{\left.\frac{\partial y(t_k, \mathbf{p}, \mathbf{u})}{\partial p_l}\right|_{\mathbf{p}^*}}_{s_{y/p_l}(t_k, \mathbf{p}^*, \mathbf{u})} \cdot \mathrm{d}p_l = 0 \Longrightarrow \mathrm{d}\mathbf{p} = 0 \tag{3.5}$$

where $s_{y/p_l}(t_k, \mathbf{p}^*, \mathbf{u})$ is the sensitivity function of the output variable $y(t_k, \mathbf{p}^*, \mathbf{u})$ *w.r.t.* the parameter p_l, for fixed input signals $\mathbf{u}$ and at a specific time instant t_k. The difference is denoted by $\mathrm{d}\mathbf{p} = \mathbf{p} - \mathbf{p}_0$, where $\mathbf{p}_0$ is the nominal value vector. As this application is characterized by the absence of an input signal, for simplification reasons, the variables $\mathbf{u}$ will be omitted in the following equations.

The sensitivity analysis is an approach commonly used to assess the identifiability of the parameters from experimental conditions. It is employed in order to define if data contain enough information to identify the parameters. As the sensitivity functions are defined by partial derivatives, dependent

of the time range or the nominal parameter values for example, sensitivity results will be local only.

The parameters and output variables may have different measurement units and/or orders of magnitude. Generally, it is recommended to normalize the sensitivity functions $s_{y/p_l}(t_k, \mathbf{p}^*)$ *w.r.t.* the parameters, the outputs, or both variables. In the present study, it is normalized *w.r.t.* both variables defined as

$$\tilde{s}_{y/p_l}(t_k, \mathbf{p}^*) = s_{y/p_l}(t_k, \mathbf{p}^*) \cdot \frac{p_l^*}{|y\,(t_k, \mathbf{p}^*)\,|_1} \tag{3.6}$$

with $|.|_1$ the L_1 norm.
Taking into account the two previous equations, the parameters $\mathbf{p}_2$ are considered to be locally *a posteriori* identifiable if the empirical Fisher Information Matrix $\mathbf{F}$ is full rank, where $\mathbf{F}$ is defined as

$$\mathbf{F} = \tilde{\mathbf{S}}_y\,(\mathbf{p}^*)^T \cdot \tilde{\mathbf{S}}_y\,(\mathbf{p}^*) \tag{3.7}$$

with $\tilde{\mathbf{S}}_y\,(\mathbf{p}^*) \in \mathbb{R}^{N \times n_p}$ the sensitivity matrix defined as

$$\tilde{\mathbf{S}}_y\,(\mathbf{p}^*) = \begin{bmatrix} \tilde{s}_{y/p_1}\,(t_1, \mathbf{p}^*) & \tilde{s}_{y/p_2}\,(t_1, \mathbf{p}^*) & \dots & \tilde{s}_{y/p_{n_p}}\,(t_1, \mathbf{p}^*) \\ \tilde{s}_{y/p_1}\,(t_2, \mathbf{p}^*) & \tilde{s}_{y/p_2}\,(t_2, \mathbf{p}^*) & \dots & \tilde{s}_{y/p_{n_p}}\,(t_2, \mathbf{p}^*) \\ \vdots & \vdots & \ddots & \vdots \\ \tilde{s}_{y/p_1}\,(t_N, \mathbf{p}^*) & \tilde{s}_{y/p_2}\,(t_N, \mathbf{p}^*) & \dots & \tilde{s}_{y/p_{n_p}}\,(t_N, \mathbf{p}^*) \end{bmatrix} \tag{3.8}$$

For multiple system outputs, the matrix $\mathbf{F}$ is computed based on a global sensitivity matrix $\tilde{\mathbf{S}}_\mathbf{y}$ given by

$$\tilde{\mathbf{S}}_\mathbf{y} = \begin{bmatrix} \tilde{\mathbf{S}}_{y_1}(\mathbf{p}^*) & \tilde{\mathbf{S}}_{y_2}(\mathbf{p}^*) & \dots & \tilde{\mathbf{S}}_{y_{n_y}}(\mathbf{p}^*) \end{bmatrix}^T \tag{3.9}$$

where $\tilde{\mathbf{S}}_{y_j}(\mathbf{p}^*)$ represents the normalised sensitivity matrix of the output variable y_j, $j = 1, \cdots, n_y$, *w.r.t.* the parameters $\mathbf{p}^*$ and n_y corresponds to the number of output variables.
However, if the rank of the empirical Fisher Information Matrix $\mathbf{F}$ is not full, one must select the *a posteriori* identifiable parameters. In that direction, several procedures exist in the literature [Weijers and Vanrolleghem (1997), Yao et al. (2003), Banks et al. (2013)] and are based on two conditions that must be satisfied:

(C1) the output variables have to be sufficiently sensitive to individual changes in each parameter of $\mathbf{p}_2$;

(C2) the sensitivity functions must be linearly independent, as changes in the model output due to a parameter variation may be compensated by appropriate changes in other parameters.

Several sensitivity measures allow to quantify the condition **C1** [Brun et al. (2002), Li et al. (2004)], as for example:

$$\delta_l^{msqr} = \sqrt{\frac{1}{N}\ \tilde{\mathbf{s}}_{y/p_l}^T\ \tilde{\mathbf{s}}_{y/p_l}} = \frac{1}{\sqrt{N}} \cdot |\tilde{\mathbf{s}}_{y/p_l}|_2 \tag{3.10}$$

$$\delta_l^{mabs} = \frac{1}{N} \sum_{k=1}^{N}\ |\tilde{s}_{y/p_l}(t_k, \mathbf{p}^*)| = \frac{1}{N} \cdot |\tilde{\mathbf{s}}_{y/p_l}|_1 \tag{3.11}$$

$$\delta_l^{mean} = \frac{1}{N} \sum_{k=1}^{N}\ \tilde{s}_y(t_k, p_l) \tag{3.12}$$

$$\delta_l^{max} = \max_k \tilde{s}_y(t_k, p_l) \tag{3.13}$$

$$\delta_l^{min} = \min_k \tilde{s}_y(t_k, p_l) \tag{3.14}$$

As this first condition takes into consideration only the individual change of a parameter on the output variables, the identifiability analysis must be completed with the evaluation of the collinearity effects between sensitivity functions. The second condition **C2** corresponds to a hybrid classification criterion by considering a collinearity index γ_K, computed for all the parameter subsets. The classification can be based on the minimisation of the J_E criterion (also known as the Modified E criterion), defined as

$$J_E(K) = cond\left(\mathbf{F}\right) = cond(\tilde{\mathbf{S}}_{\mathbf{y}}\left(\mathbf{p}_K\right)^T \cdot \tilde{\mathbf{S}}_{\mathbf{y}}\left(\mathbf{p}_K\right)) \tag{3.15}$$

where $cond(\mathbf{F})$ represents the condition number of the Fisher Information Matrix. The condition number evaluates the dependency of the solutions *w.r.t.* observations. An important condition number reveals a sensitivity of the solution to measurement uncertainties. In this case, the problem can be well-posed but ill-conditioned, that makes the problem resolution more complex. In an equivalent manner, the collinearity index γ_K can be defined as the condition number of the global sensitivity matrix instead of the Fisher Information matrix, as follows

$$\gamma_K = cond\left(\tilde{\mathbf{S}}_{\mathbf{y}}\left(\mathbf{p}_K\right)\right) \tag{3.16}$$

This index is computed for all possible parameter subsets $\mathbf{p}_K$ with $K \leq n_p$, and it characterizes the degree of linear dependency between the sensitivity functions of the output variables *w.r.t.* the parameters in $\mathbf{p}_K$.
The parameter set $\mathbf{p}_K$ is considered to be *a posteriori* identifiable if it presents low to moderate collinearity index γ_K and indicative thresholds are given below [Belsley et al. (2005)]:

$$\begin{cases} 5 \leq \gamma_K < 10 & \text{low collinearity} \\ 30 \leq \gamma_K \leq 100 & \text{moderate collinearity} \\ \gamma_K \geq 100 & \text{strong collinearity} \end{cases} \tag{3.17}$$

The individual and global sensitivity matrices, expressed respectively in equations (3.8) and (3.9), can be computed *w.r.t.* model parameters $\mathbf{p}_a$ and/or initial conditions of the state variables $\mathbf{x}_0$. For sufficiently simple models, the *a posteriori* identifiability analysis can combine model parameters $\mathbf{p}_a$ and initial conditions $\mathbf{x}_0$. However, for complex models, it is recommended [Banks et al. (2007)] to split the investigation in two stages:

1. the analysis of the output sensitivity *w.r.t.* initial conditions $\mathbf{x}_0$, for fixed model parameters;
2. the analysis of the output sensitivity *w.r.t.* the model parameters $\mathbf{p}_a$, for fixed initial conditions.

The second step investigates only the identifiability of the model parameters $\mathbf{p}_a$. Compared with the initial conditions $\mathbf{x}_0$ which are specific for each trial, model parameters must be representative of all the experimental cases. The experimental conditions are however different from one test to another, and then, the relevance of model parameters can vary, depending on the selected case. Therefore, identifiability of $\mathbf{p}_a$ can be performed by considering several experimental cases together to increase the number of identifiable parameters [Yao et al. (2003)]. The main advantage of the proposed approach is to reveal the parameter sensitivity on a larger envelope of the experimental conditions. In this case, the global sensitivity matrix is defined as

$${}^{n_s}\tilde{\mathbf{S}}_{\mathbf{y}} = \left[\begin{array}{cccccccccc} {}^1\tilde{\mathbf{S}}_{y_1}(\mathbf{p}_a^*) & {}^1\tilde{\mathbf{S}}_{y_2}(\mathbf{p}_a^*) & \dots & {}^1\tilde{\mathbf{S}}_{y_{n_y}}(\mathbf{p}_a^*) & {}^2\tilde{\mathbf{S}}_{y_1}(\mathbf{p}_a^*) & \dots & {}^2\tilde{\mathbf{S}}_{y_{n_y}}(\mathbf{p}_a^*) & \dots & {}^{n_s}\tilde{\mathbf{S}}_{y_{n_y}}(\mathbf{p}_a^*) \end{array} \right]^T \tag{3.18}$$

where ${}^i.$, $i =, ..., n_s$, represents a selected free flight test case.
In practice, a second approach can be used as mentioned in [Yao et al. (2003)], based on *a priori* knowledge of the system. The goal is to work with pre-selected parameters, defined as key parameters to be estimated from an output. However, we should ensure that the parameters can be determined from the data.

3.4.3 Identifiability analysis - application to space probe models

This section is dedicated to the local identifiability evaluated at $\mathbf{p}_0$ of the model structure describing the behaviour of a re-entry space vehicle in free flight, presented in Chapter 2, through the techniques introduced in Section 3.4. Three aerodynamic coefficients are considered, the drag coefficient C_D, the pitch moment coefficient slope $C_{m\alpha}$ and the pitch damping coefficient C_{mq}. The pitch moment coefficient slope $C_{m\alpha}$ was not studied in the present work, however it can be obtained through CFD predictions.
As a reminder, the proposed drag and the pitch damping coefficient descriptions, presented in Section 2.4.4.1, are functions of the Mach number and the total angle of attack α_t, as

$$C_D\left(M,\alpha_t\right) = C_{D0} + C_{D1}\ M + C_{D2}\ M^2 + C_{D3}\ \sin^2\alpha_t + C_{D4}\ \sin^4\alpha_t + C_{D5}\ M\ \sin\alpha_t \tag{3.19}$$

$$C_{mq}\left(M,\alpha_t\right) = C_{mq0} + C_{mq1}\ M^* + C_{mq2}\ M^{*2} + C_{mq3}\ \sin^2\alpha_t + C_{mq4}\ \sin^4\alpha_t + D_\alpha\ \left(\alpha_t - \bar{\alpha}_t\right)_+^2 \tag{3.20}$$

The parameter set to identify is then

$$\mathbf{p} = \mathbf{p}^{\{sv\}}/\mathbf{p}_{m\alpha} = \left[\begin{array}{c} \mathbf{x}_0, \\ \mathbf{p}_D, \\ \mathbf{p}_{mq} \end{array}\right] = \left[\begin{array}{c} V_0, \alpha_0, \beta_0, \omega_{x0}, \omega_{y0}, \omega_{z0}, \phi_0, \theta_0, \psi_0, \\ C_{D0}, C_{D1}, C_{D2}, C_{D3}, C_{D4}, C_{D5}, \\ C_{mq0}, C_{mq1}, C_{mq2}, C_{mq3}, C_{mq4}, D_\alpha \end{array}\right] \tag{3.21}$$

and is composed of the initial conditions of the state variables $\mathbf{x}_0$ and the model parameters $\mathbf{p}_a = [\mathbf{p}_D, \mathbf{p}_{mq}]$ describing the drag and the pitch damping coefficients.

For example, it is well-known that the drag coefficient can be directly obtained from the Doppler radar data due to its strong dependency on the velocity [Lieske and al. (1972), Chen et al. (1997)]. In this sense, it is mainly determined for fixed Mach numbers or as a function of the Mach number only [Dutta et al. (2008)]. However, in studies where the incidence angles can reach high values during the flight, their effects on aerodynamic coefficients are no longer negligible. In such cases, all the influential variables must be considered to describe the coefficients for obtaining accurate and interpretable values. Moreover, it has been noticed that the estimation of the pitch damping coefficient C_{mq}, characterizing the dynamic stability of a flying vehicle, encounters difficulties. Indeed, several studies illustrate the shortcomings of the CFD simulation and/or wind tunnel experimental results in determining this coefficient [Murman and Aftosmis (2007), Gülhan et al. (2011)], generally possible only for small angles of attack. Previous studies on the determination of C_{mq} based on experimental data and using two existing parameter identification codes ARFDAS and CADRA (Comprehensive Automated Data Reduction and Analysis) have shown disagreements [Schoenenberger et al. (2009)]. Thus, the pitch damping coefficient identification from free flight data is a challenging problem to solve.
For these reasons, identifiability studies must be carefully investigated before applying the estimation step.

The four considered output variables $y_j(t_k)$, $j = 1, \ldots, 4$, correspond to radar and 3D magnetometer signals described in equations (2.53) and (2.54), respectively.

3.4.3.1 *A priori* identifiability results

By considering the mathematical model, namely the state equations (2.49-2.52), the output equations (2.53-2.54) and the aerodynamic coefficient descriptions recalled in (3.19) and (3.20), we applied the Sedoglavic's algorithm for testing local *a priori* identifiability [Sedoglavic (2002)]. It

returns the number of non-identifiable parameters which, in this case, was null. This means that all the considered parameters $\mathbf{p}$ are locally theoretically identifiable and thus,

$$\mathbf{p}_1 = \mathbf{p} = \left[\mathbf{x}_0,\, \mathbf{p}_D,\, \mathbf{p}_{mq} \right] \tag{3.22}$$

3.4.3.2 *A posteriori* identifiability results

Let us detail now the *a posteriori* identifiability results obtained for the space probe application case. As already mentioned, this analysis allows to take into account the experimental conditions and is able to quantify the identifiability of the unknown parameters. The local sensitivity functions of the output variables *w.r.t.* the parameters $\mathbf{p}_1$ were symbolically computed and further integrated in the Simulink model. For the computation of the individual and global sensitivity matrices, the five free flight experimental conditions presented in Table 1.4 have been used. As seen in equation (3.22), the parameter set $\mathbf{p}_1$ is composed of the model parameters $\mathbf{p}_a = [\mathbf{p}_D, \mathbf{p}_{mq}]$ and initial conditions of the state variables $\mathbf{x}_0$.
The computation of the empirical Fisher Information Matrix (for individual and global sensitivity matrices) concluded in a rank-deficient matrix. For example, for test case 5, considering a combined (model parameters and initial conditions) analysis leads to a condition number of the $\mathbf{F}$ matrix varying from $8.66 \cdot 10^{14}$ to $2.21 \cdot 10^{34}$ for the $\mathbf{F}_i$ matrices, with $i = 1, \cdots, 4$, while the global matrix has a condition number of $1.31 \cdot 10^{13}$. This means that all the parameters included in $\mathbf{p}_1$ cannot be estimated at the same time. In the next sub-sections, the analysis will consider separately the sensitivity *w.r.t.* model parameters and initial conditions.

Sensitivity analysis *w.r.t.* initial conditions

In order to check the *a posteriori* identifiability of the initial conditions $\mathbf{x}_0$, the model parameters have to be considered fixed, and were initialized based on literature and aerodynamic coefficient database existing at ISL. As a reminder, the initial condition vector is defined as

$$\mathbf{x}_0 = [V_0, \alpha_0, \beta_0, \omega_{x0}, \omega_{y0}, \omega_{z0}, \phi_0, \theta_0, \psi_0] \tag{3.23}$$

Testing the *a posteriori* identifiability for nonlinear model is not an easy task, hence the requirement of having a physical representation of the behaviour of a vehicle in free flight and *a priori* knowledge. Such information allows to know nonlinear functional relations between parameters, to impose initial guess of the parameters and interpret the obtain results. We have computed the sensitivity measure δ_l^{msqr} expressed in equation (3.10) for each output variable y_i, $i = 1, \cdots, 4$ and *w.r.t.* the unknown initial conditions $\mathbf{x}_0$. However, in the case of nonlinear models, the obtained results for the condition **C1** must be carefully interpreted. This is due to the nonlinear relations between parameters which affect also the sensitivity functions and thus, the results of the condition **C1** analysis. Based on *a priori* knowledge, the main comments are the following:

- the most influential parameter on the radar output is the initial velocity V_0;
- the radial magnetometer signals, $H_{y,body}$ and $H_{z,body}$, are mainly sensitive to the initial roll rate ω_{x0} and roll angle ϕ_0.

Distinct approaches can be used to determine the identifiability of initial conditions $\mathbf{x}_0$ from condition **C2**, and results are given for test case 5 as an example:

- without *a priori* knowledge: by considering four output variables expressed in equations (2.53-2.54), the initial conditions $\mathbf{x}_0$ and the identifiability condition **C2** presented in the previous section, we have concluded to six linearly independent parameters $[V_0, \alpha_0, \omega_{x0}, \omega_{y0}, \omega_{z0}, \phi_0]$ with a collinearity index γ_K equal to 124. To increase the number of

identifiable parameters, additional outputs were considered. One can note that by using the 3D high speed trajectory tracker system, the lateral positions y_E and z_E can be determined. By considering y_E as additional output, we obtain seven linearly independent parameters $[V_0, \alpha_0, \beta_0, \omega_{x0}, \omega_{y0}, \omega_{z0}, \phi_0]$, giving one parameter more, with a collinearity index γ_K of 158. The remaining initial conditions θ_0 and ψ_0 are determined using the nearly rectilinear trajectory hypothesis. Indeed, the translational kinematic equations $\dot{y}_E$ and $\dot{z}_E$ are considered equal to zero. By resolving these equations at the initial time, θ and ψ can be described *w.r.t.* the incidence angles α, β and the roll angle ϕ [Stengel (2004), Cook (2012)] and then, a relationship between their initial conditions can also be defined.

- with *a priori* knowledge: by considering the *a priori* knowledge of the system to analyze condition **C2**, we considered in a first step only the radar and the radial magnetometer signals V, $H_{y,body}$ and $H_{z,body}$, as outputs. With pre-selected parameters, three linearly independent parameters $[V_0, \omega_{x0}, \phi_0]$ can be defined with a collinearity index γ_K of 50. These parameters are considered known and the remaining initial conditions are analyzed in a second step by considering the four outputs. We concluded to six linearly independent parameters $[\alpha_0, \beta_0, \omega_{y0}, \omega_{z0}, \theta_0, \psi_0]$ with a collinearity index γ_K of 18.

Sensitivity analysis *w.r.t.* model parameters

Concerning the identifiability of model parameters, condition **C1** was analyzed and here again concluded to coherent results with the *a priori* knowledge in the domain. It was detected that the parameter $\mathbf{p}_D$ describing the drag coefficient C_D are mainly influencing the first output signal y_1, namely the radar signal, whereas the pitch damping parameters $\mathbf{p}_{mq}$ have a most relevant effect on the output signals y_2, y_3, y_4, namely the magnetometer signals. One of our previous study on the pitch damping coefficient [Albisser et al. (2013)] has shown that the term in $\sin^4 \alpha_t$ related to the parameter C_{mq4} is not identifiable from magnetometer signals, and the same conclusion was made for the drag coefficient parameter C_{D4} on the radar signal.

The individual radar sensitivity matrix have been computed *w.r.t.* the model parameter $\mathbf{p}_D$ describing the drag coefficient C_D. Depending on the considered test case, the collinearity index of the output variable y_1 *w.r.t.* model parameters $\mathbf{p}_D$ varies from $1.29 \cdot 10^4$ to $7.53 \cdot 10^4$. Furthermore, it was noticed that the condition number is improved by considering several experimental tests. Figures 3.4 illustrate the collinearity index γ_K of the velocity signal for each dimension of subsets contained in $\mathbf{p}_D$ in a logarithm (log10) scale, by considering the five test cases in Figure 3.4a and by considering only the test case 3 as an example in Figure 3.4b. The minimal γ_K is represented by square markers and the dotted lines represent the thresholds defined in (3.17). One can note that the condition number, calculated based on the global sensitivity matrix in equation (3.18), is smaller by taking into account multiple tests for evaluating the sensitivity function collinearity. This study concludes that the largest *a posteriori* identifiable subset from radar data is composed of $[C_{D0}, C_{D1}, C_{D2}]$ with a collinearity index of 158 by taking into account all the experimental conditions.

The global magnetometer sensitivity matrices have been computed *w.r.t.* the model parameter $\mathbf{p}_{mq}$ describing the pitch damping coefficient C_{mq}. Depending on the considered test case, the collinearity index is varying between $1.70 \cdot 10^3$ and $4.83 \cdot 10^3$.
For the same reasons as previously, multiple data series were considered for the sensitivity analysis and thus, the global sensitivity matrix in equation (3.18) was employed to calculate the collinearity index. Figures 3.5 illustrate the collinearity index γ_K of the magnetometer signals for each dimension of subsets contained in $\mathbf{p}_{mq}$ in a logarithm (log10) scale, by considering the five test cases in Figure 3.5a and by considering only the test case 3 in Figure 3.5b. The minimal γ_K is represented

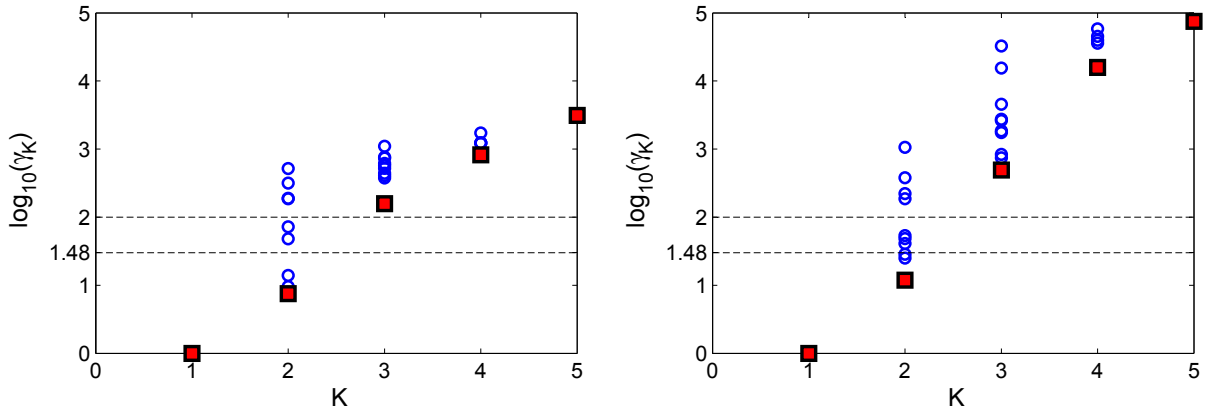

(a) Multiple experimental tests (b) Test case 3

Figure 3.4: Classification of parameters based on the γ_K collinearity index of the velocity output variable *w.r.t.* drag coefficient parameters $\mathbf{p}_D$ subsets

by square markers and the dotted lines represent the thresholds defined in (3.17). Here again, it can be observed that the collinearity index is smaller by taking into account multiple tests. It led to the outcome that all the remaining parameters describing C_{mq} are *a posteriori* identifiable from magnetometer signals, with a collinearity index equivalent to 185 by considering all the experimental conditions. This remark is confirmed by considering the parameter D_α describing the spline contribution in the pitch damping coefficient description. This parameter is considered only when α_t is greater than 10° and due to the experimental conditions of some test cases, this value is not always reached on the flight path. In that case, sensitivity analysis will concluded that D_α is not or less identifiable whereas it is just not defined on the flight envelope of these test cases. However, this parameter can be identified from additional tests with total angle of attack values greater than 10°. As this analysis takes into account experimental conditions, it is more convenient to cover a larger flight envelope, especially in terms of Mach number and total angle of attack.

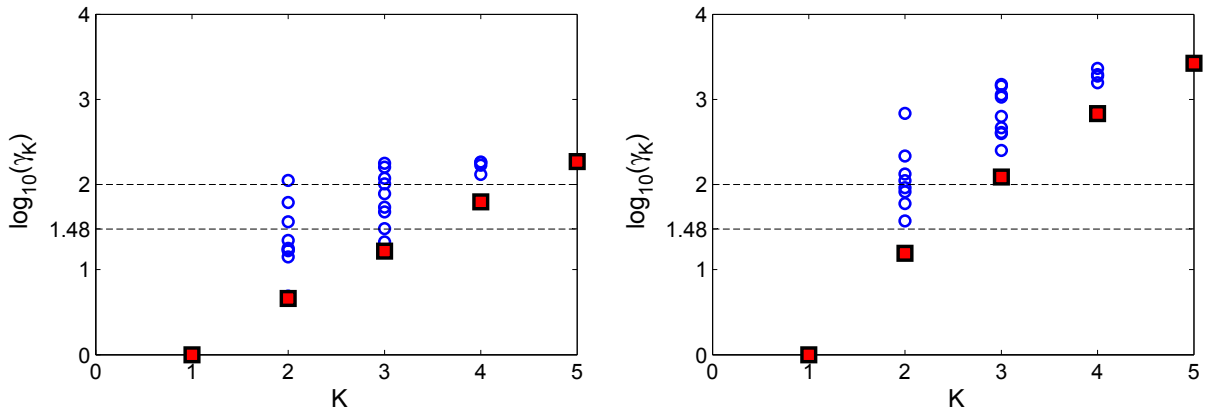

(a) Multiple experimental tests (b) Test case 3

Figure 3.5: Classification of parameters based on the γ_K collinearity index of the magnetometer output variables *w.r.t.* pitch damping coefficient parameters $\mathbf{p}_{mq}$ subsets

The identifiability analysis gives the parameters $\mathbf{p}_{a,2}$ as identifiable based on the outputs with

$$\mathbf{p}_{a,2} = [\mathbf{p}_{D,2}, \mathbf{p}_{mq,2}] = [C_{D0}, C_{D1}, C_{D2}, C_{mq0}, C_{mq1}, C_{mq2}, C_{mq3}, D_\alpha] \tag{3.24}$$

Therefore, identifiability analysis leads to the following main conclusions:

- the *a priori* identifiability analysis showed that all the parameters can be considered as locally identifiable. This implies that the model structure is well posed in the Hadamard sense;
- as the empirical Fisher Information Matrix was found to be rank deficient, two classification criteria were further used in order to select the *a posteriori* identifiable parameters and the initial conditions $\mathbf{x}_0$ and the model parameters were analyzed separately;
- with the integration of *a priori* knowledge, we obtain sensitivity functions *w.r.t.* $\mathbf{x}_0$ which are linearly independent and thus, all the initial conditions can be identified;
- all the model parameters, except the parameters C_{D4} and C_{mq4}, are sufficiently sensitive to influence at least one output variable and eight of them can be considered as being linearly independent;
- the sensitivity matrix computed based on multiple data series showed a better condition number and therefore improves the identifiability of the parameters;
- the identifiability results are coherent with *a priori* knowledge in the domain.

3.5 Estimation of aerodynamic parameters

This section details the employed strategy for the aerodynamic parameter estimation. A 6DOF code already exists at ISL for the aerodynamic coefficient determination but presents several limitations, especially concerning the aerodynamic coefficient representations. They are described in a tabular form, for fixed values of Mach numbers or total angles of attack α_t. For this reason and in order to improve the accuracy and the understanding of the estimated coefficients, a new inverse 6DOF code included several improvements was developed.

The parameter estimation is achieved through the use of the developed code, denoted as Inv6DoF, implemented under Matlab/ Simulink. The model implementation was presented in Section 3.3 and a Matlab code was developed and integrated into the tool to proceed to the aerodynamic parameter estimation from a single and/or a multiple fit strategy. The parameters are estimated by using a traditional iterative nonlinear Least Squares method. The *a posteriori* identifiability is meant to guide the estimation process. The identifiability analyses proposed to check the identifiability of the initial conditions $\mathbf{x}_0$ and the model parameters $\mathbf{p}_a$ in two stages. For the same reasons, an estimation procedure composed of two distinct steps and illustrated in Figure 3.1 was applied:

1. the first step, defined as a single fit estimation strategy, aims at determining the initial conditions $\mathbf{x}_{0,2}$ and the aerodynamic coefficients $\mathbf{C}[\mathbf{x}]$ for each data series i, with $i = 1, \cdots, n_s$. This step is considered as an intermediate phase to mainly determine the initial conditions of each trial. To obtain preliminary aerodynamic values, the coefficients $\mathbf{C}[\mathbf{x}]$ are estimated in a tabular form, for fixed Mach number or total angle of attack values.
2. the second step is dedicated to the estimation of the aerodynamic coefficients, described as polynomial functions dependent of the state variables and model parameters $\mathbf{p}_a$, based on several data series. To increase the probability that the coefficients define the vehicle's aerodynamics over the entire range of test conditions and to improve the accuracy of the estimated coefficients, a multiple fit strategy was considered. As all the free flight tests are conducted with the same vehicle, this strategy attempts to obtain meaningful aerodynamic coefficients evolution as a function of the Mach number and the total angle of attack which should be

valid for all test cases. Moreover, it allows to cover a larger envelope of variation of both variables and provides a common set of aerodynamic coefficients that are determined from multiple data series simultaneously analyzed, that gives a more complete spectrum of the vehicle's motion. As identifiability analysis based on a combination of data sets improves the number of identifiable parameters, this strategy will also improve the parameter estimation. The combination of multiple data series was already used to provide a better representation of the flight envelope and improve the estimated aerodynamic coefficients [Dupuis and Hathaway (1997)] but only in a tabular form for constant Mach numbers. Several techniques were presented in the literature [Leith et al. (1993)] by using superposition, concatenation or multiple cost approaches. The last one is the most adapted to the case of nonlinear systems and allows to preserve all the information revealed through single fit identification.

The multiple cost function approach was applied and the estimation criterion for the second step is then defined as follows:

$$\bar{\mathrm{J}}(\mathbf{p}_{a,2}) = \sum_{i=1}^{n_s} \mathrm{J}_i(\mathbf{p}_{a,2}) \tag{3.25}$$

where $\mathbf{p}_{a,2}$ are the *a posteriori* identifiable parameters describing aerodynamic coefficients.

3.6 Concluding remarks

In this chapter, the proposed grey-box model identification procedure for the aerodynamic parameter estimation has been presented. It is composed of six main steps, from the definition of the model structure to the parameter estimation issue. The intermediate steps are the model implementation and the identifiability analysis. The implemented model represents the kernel of the inverse 6DOF code developed in the frame of this study. As the structure of the model is nonlinear, the identifiability results are only local. Nevertheless, if the identifiability results are carefully interpreted, they allow to guide the estimation process. They brought to light the complexity of the analysis when initial conditions and model parameters are considered and when nonlinear dependency between parameters is observed. It was also shown that using multiple data sets for the sensitivity analysis allowed to increase the number of identifiable parameters. In this sense, the same strategy was used for the parametric estimation of the aerodynamic coefficients. The multiple fit strategy presents many advantages as covering a larger flight envelope, in terms of Mach numbers and total angles of attack, and obtaining meaningful aerodynamic coefficients valid for several test cases.
Even if the identifiability analyses were performed only for the space probe case, similar conclusions can be made for the projectile concerning the initial conditions. For the projectile aerodynamic coefficients, simplified descriptions were used due to the limited number of trials to validate polynomial descriptions. This is more widely explained in the next chapter dedicated to the application results for space probe and projectile cases.

Chapter 4

Application results and discussions

Free flight tests were performed for two different applications: an Earth re-entry space vehicle and a projectile. Guided by identifiability results, parameters describing the aerodynamic coefficients as well as the state variable initial conditions can be estimated based on free flight data. Application results that highlight the key features of both configurations are presented in this chapter. They mainly include the comparison between the measured and the simulated magnetometer signals, the evolutions of the simulated attitude angles and total angle of attack, as well as the estimated aerodynamic coefficients. The latter were at first determined for each single flight then improved by using a multiple fit strategy. Furthermore, in the case of the projectile, the axial position and the pitch angle obtained from radar data and on-board sensor technique respectively, are compared to those determined from images extracted from high speed video systems. Results are analyzed and discussed to compare the relevant variables influencing the behaviour in free flight of the space probe with the projectile. Aerodynamic coefficients determined during these studies are in good agreement with literature data.

During the different test campaigns, the measured data consist in the velocity obtained from a Doppler radar and the signals obtained from 3D magnetometer sensor. These signals are used for the parameter estimation by means of the Inv6DoF code, developed during this thesis.

4.1 Space probe

Several free flight tests were conducted at the ISL open range test site with re-entry space models, as summarized in Table 1.4. Initial launch Mach numbers were equal to 2.0 and 3.0 with initial angles of attack [1] of 0° and 3° . An example of typical measured signals are presented in Figure 4.1. Figure 4.1a presents raw signal data as a function of time obtained from the three magnetometers in combination with the velocity profile obtained from the radar data. Position A indicates the location of the muzzle exit and position B the location of the recovery system. An enlarged view of the magnetic signals between 40 and 160 ms is shown in Figure 4.1b in which very small perturbations of the signals can be observed as indicated by positions C and D. These discontinuities are due to the presence - along the fireline - of two sky screens, disturbing the Earth magnetic field in their vicinities. They are necessary for the corrections of the rotation velocities of the trajectory tracker mirrors. These perturbations of the magnetometer signals can be considered as negligible as they have very low amplitude and cover a time range of about 4 ms.

1. As a reminder, this initial angle of attack, denoted by $\alpha 0$, corresponds to the incidence angle into the sabot.

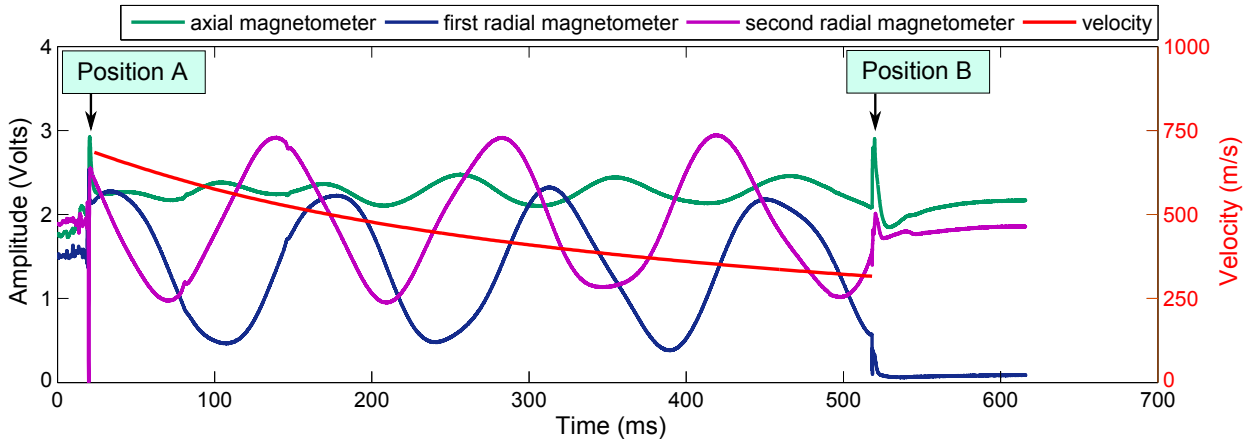

(a) Magnetometer and radar signals

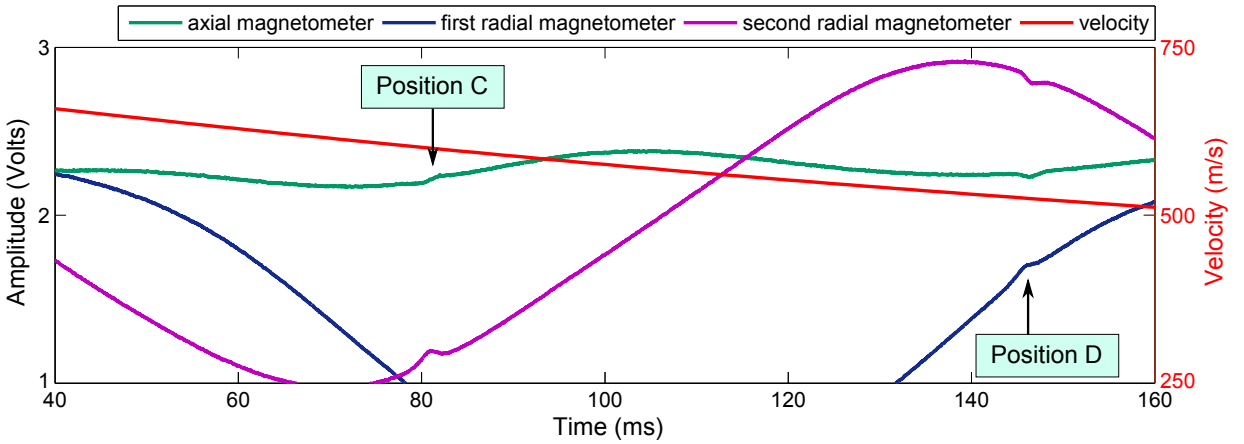

(b) Enlarged view of signals

Figure 4.1: Measured signals for the space probe at $M0 = 2.0$ and $\alpha 0 = 3°$

As mentioned previously, the vehicle will be considered in free flight only when the model is flying without anymore interaction with the sabots petals. Moreover, magnetic signals can be disturbed by the magnetic effects in the vicinity of the gun platform and the gun tube. It is therefore more convenient to process data after a position of about 10 meters of the flight path. In this sense, signals are considered from an initial time t_0 different from ignition time.
For illustrative purposes, only two test cases are presented in Figures 4.2 and 4.3. They consist of:

- test case 2: a spinning model with an initial Mach number of 2.0 and an initial angle of attack of 0°;
- test case 4: a spinning model with an initial Mach number of 3.0 and an initial angle of attack of 0°;

Figures 4.2 and 4.3 show the evolution of the velocity as well as the amplitude and frequency of the axial and the two radial magnetometer signals as a function of time for test case 2 and test case 4, respectively. In both cases, measurements were considered for model identification after $t = 30$ ms corresponding to the time-instant where the models are considered to be in free flight. The range of variation of the signal amplitude corresponds to supply voltage varying from 0 to 3.3 volts.

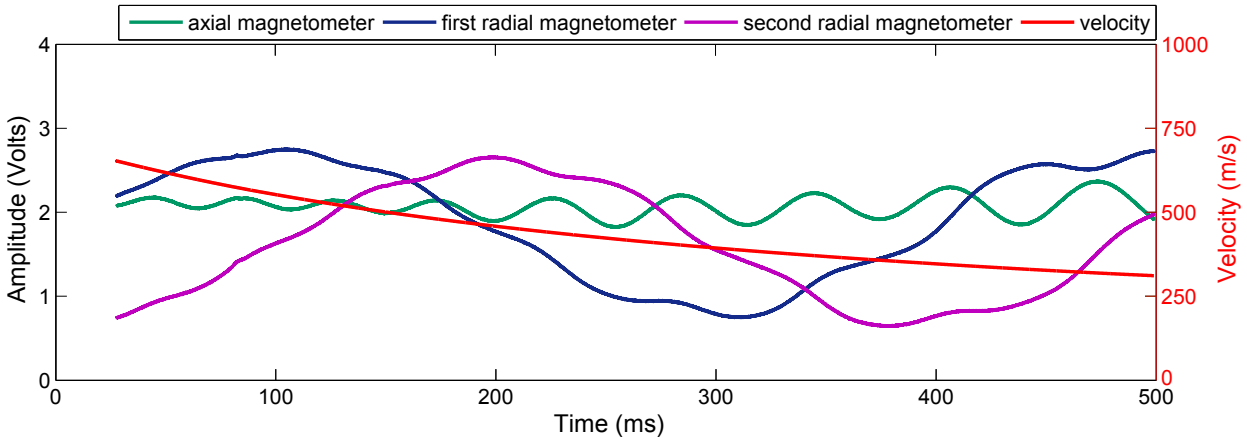

Figure 4.2: Evolution of magnetometer and radar signals of a spinning case at $M0 = 2.0$, $\alpha 0 = 0°$ (test case 2)

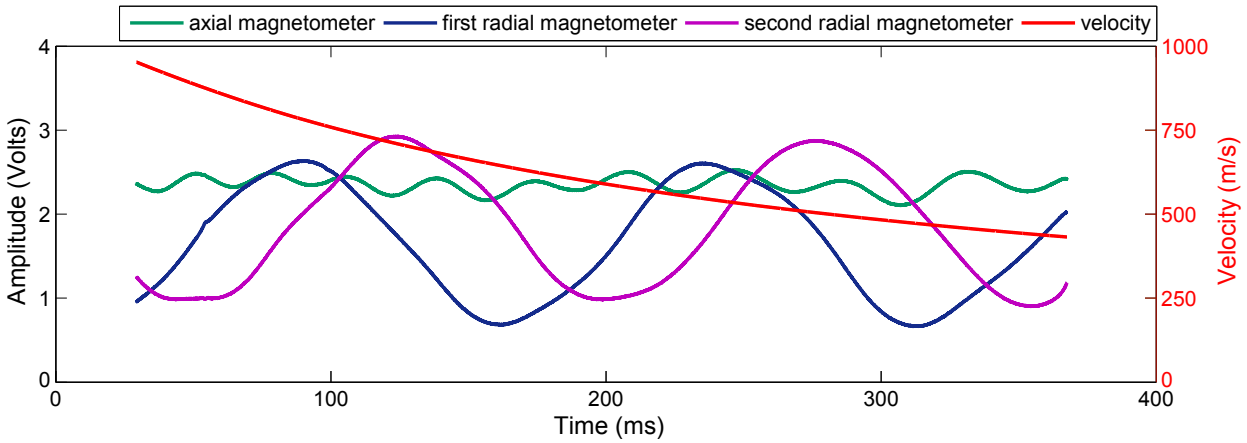

Figure 4.3: Evolution of magnetometer and radar signals of a spinning case at $M0 = 3.0$, $\alpha 0 = 0°$ (test case 4)

The velocity evolution shows a significant speed decrease of about 650 m/s to 310 m/s for test case 2 and of about 953 m/s to 430 m/s for test case 4. This decrease is due to the high vehicle drag generated by blunt bodies. The difference in flight time between the two test cases over an equal flight distance is due to the lower initial Mach number for test case 2. The axial magnetic signal gives the projection of the angle of attack in a plane defined by the flight direction and the orientation of the Earth magnetic field. The radial signals give primary an indication of the roll position and therefore of the spin rate. The curved shapes of the radial signals indicate that the model is spinning on at least one complete rotation as seen in Figure 4.2 whereas two complete rotations can be observed in Figure 4.3. The corresponding spin rate can be quantified by rotation per minute (rpm), deduced from the radial signals are equal to 143 rpm and 384 rpm, respectively.

4.1.1 Model's ability to reproduce the measured output signals

Based on the measured data and guided by the identifiability results, as explained in the previous chapter, the model parameters were estimated. The estimated parameters are then simulated in the full nonlinear model, presented in Section 3.3. The model outputs are compared to the measured outputs.

A comparison between the velocity model output and the radar measurement is presented in Figure 4.4 for test case 2. Radar data is mainly influenced by the initial velocity V_0 and the drag coefficient. In this sense, the simulated velocity is compared to the radar measurement after the estimation of the initial velocity for each trial and of the drag coefficient parameters based on a multiple fit strategy. To compare the performance, it is more relevant to present the cost function values than to plot the output residual [2] shown on top of Figure 4.4. As the velocity values have an order of magnitude of a few hundreds, the sum of output residuals at each time-instant can increase very quickly. Thus, the estimation criterion defined for the second step of the estimation stage is adapted from equation (3.25) and described as

$$\bar{J}_N(\mathbf{p}_D) = \sum_{i=1}^{n_s} \frac{\mathrm{J}_i(\mathbf{p}_D)}{N_i} \tag{4.1}$$

After the estimation of the parameters describing the drag coefficient by considering the five test cases, $\bar{J}_N(\mathbf{p}_D)$ is equal to 0.497. The cost function value for each test case are presented in Table 4.1. These errors between the measured and simulated velocities are considered as acceptable compared to the order of magnitude of the velocity.

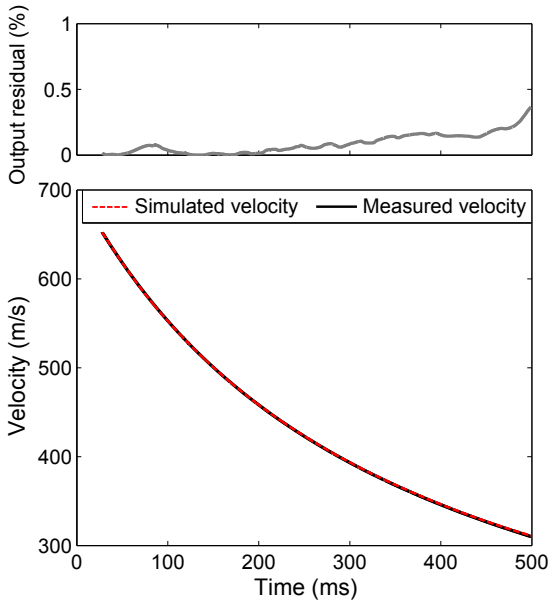

Figure 4.4: Simulated and measured velocity of a spinning case at $M0 = 2.0$, $\alpha 0 = 0°$ (test case 2) and the associated output residual

	test case 1	test case 2	test case 3	test case 4	test case 5
$\mathrm{J}_i(\mathbf{p}_D)/N_i$	0.158	0.108	0.119	0.031	0.081

Table 4.1: Cost function between simulated and measured velocity of the five test cases

The pitch damping coefficient was estimated based on a multiple fit strategy from magnetometer data. The comparison between the measured and the simulated magnetometer signals for test case 2, denoted y_2, y_3, y_4 in the previous chapters, is presented in Figure 4.5a for the axial signal and in Figure 4.5b for the first (solid line) and second (dashed line) radial ones.

2. In this chapter, the output residual is always drawn in terms of percentage error by which differs the simulated signal from the measured signal.

The same comparison between the measured and the simulated magnetometer signals, for test case 4 is presented in Figures 4.6. For both cases, their associated output residuals are shown on the top of these figures. The fit between the measured and the simulated signals can be considered as very good as shown by the output residuals between the two curves. This difference is small and quite sufficient for the determination of the angular motion history.

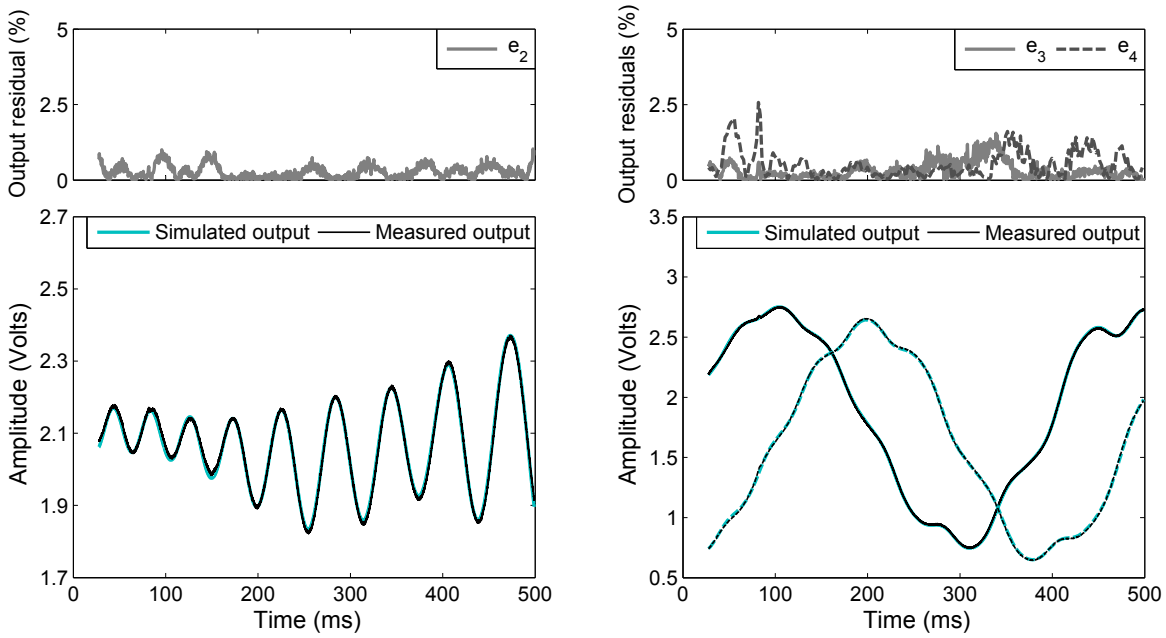

(a) Axial magnetometer (b) Radial magnetometers

Figure 4.5: Simulated and measured magnetometer signals of a spinning case at $M0 = 2.0$, $\alpha 0 = 0°$ (test case 2) and the associated output residuals

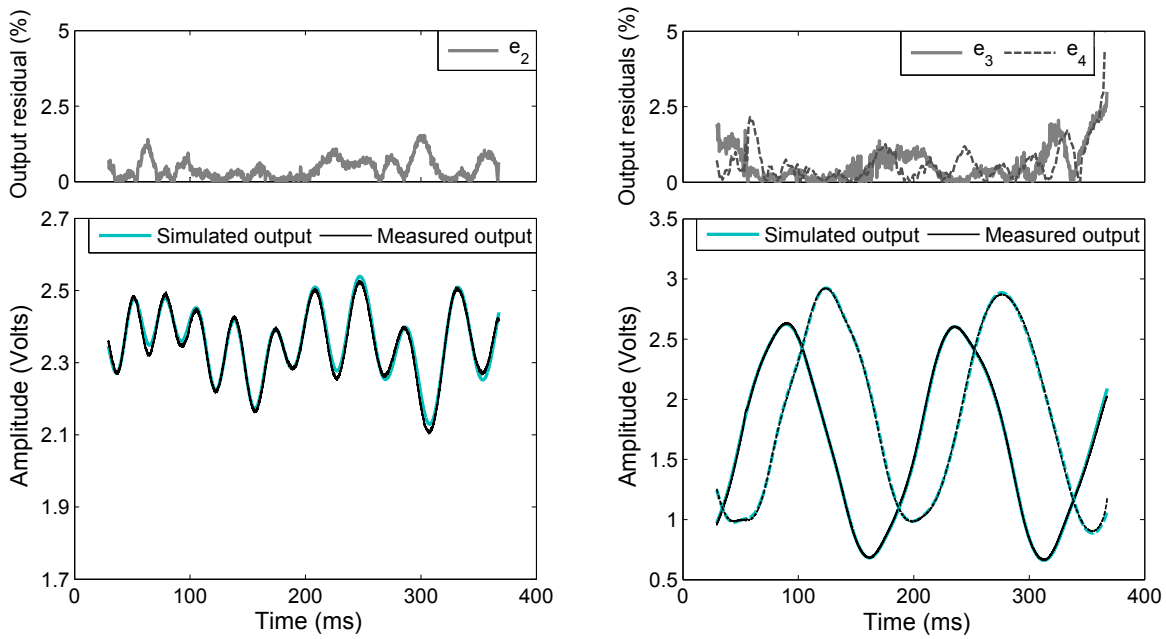

(a) Axial magnetometer (b) Radial magnetometers

Figure 4.6: Simulated and measured magnetometer signals of a spinning case at $M0 = 3.0$, $\alpha 0 = 0°$ (test case 4) and the associated output residuals

4.1.2 Evolution of the state variables

4.1.2.1 Total angle of attack and Mach number

The evolution of the total angle of attack α_t and the Mach number profile as a function of time are illustrated for test case 2 and test case 4 in Figures 4.7 and 4.8, respectively. As the Mach number and the incidence angles correspond to the variables of the aerodynamic coefficient descriptions, their variations during flight are significant of the vehicle behaviour.

One can observe that Mach numbers decrease from the supersonic regime at $M = 1.97$ to the transonic regime at $M = 0.94$ for test case 2 and from $M = 2.87$ to $M = 1.3$ for test case 4.

Concerning the total angle of attack, one can see an increase from $\alpha_t = 2.8°$ to $\alpha_t = 17.9°$ for test case 2 and from $\alpha_t = 1.6°$ to $\alpha_t = 14.6°$ for test case 4. This behaviour is representative of a statically stable model with an undamped linear motion or divergent oscillatory incidence motion that could be dynamically unstable. For the same initial angle of attack $\alpha 0 = 0°$, the higher angle of attack between test case 2 and for test case 4 is due to the different initial velocities.

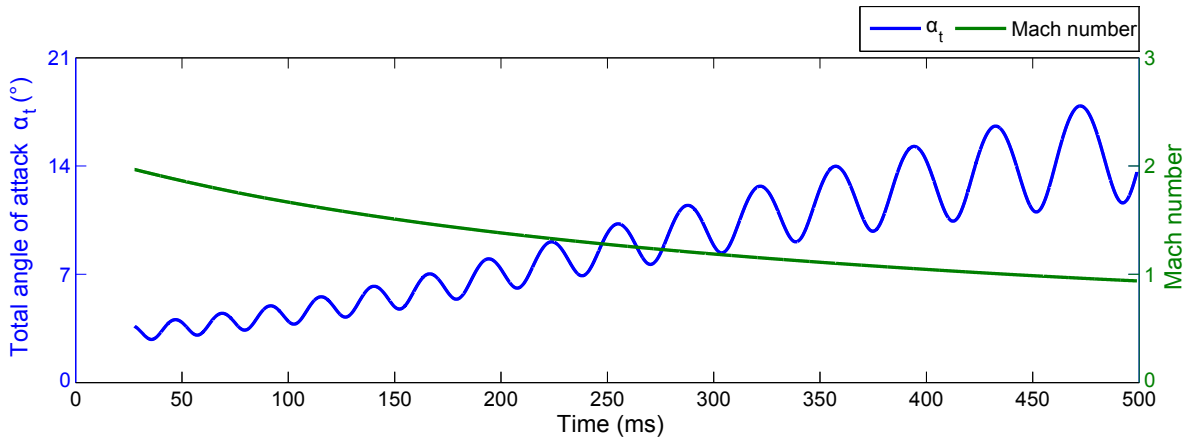

Figure 4.7: Evolution of the total angle of attack and the Mach number of a spinning case at $M0 = 2.0$, $\alpha 0 = 0°$ (test case 2)

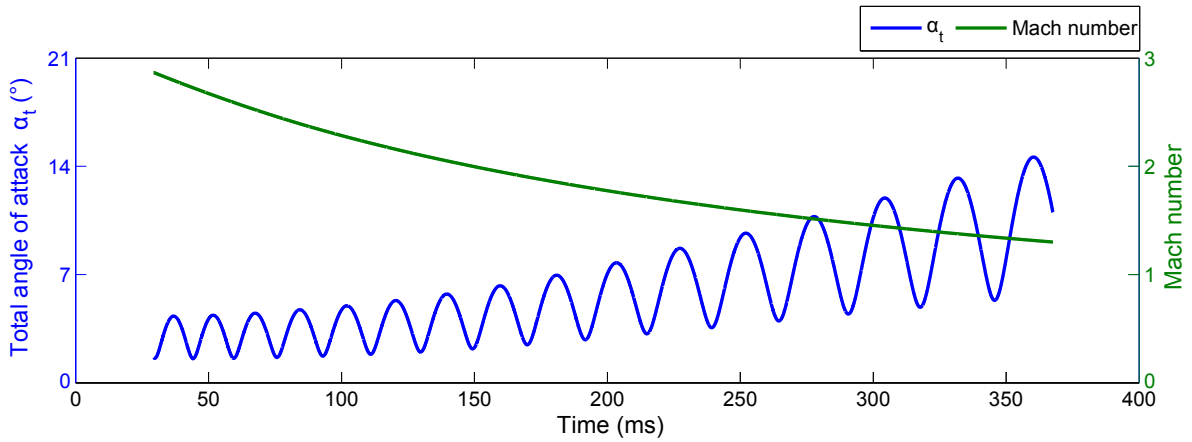

Figure 4.8: Evolution of the total angle of attack and the Mach number of a spinning case at $M0 = 3.0$, $\alpha 0 = 0°$ (test case 4)

4.1.2.2 Polar motion

Figures 4.9 and 4.10 show, in black, the three dimensional plots of the angular motion as a function of axial position x_E for test case 2 and test case 4, respectively. These motions can be compared to the motions observed from the movies obtained by the high speed video system. The attitude components, i.e. pitch and yaw angles, are shown by the blue and green lines, respectively. When moving downrange, the model exhibits a rapid growth of the pitch and yaw angles in both direction. This behaviour is confirmed by the two dimensional projection of the pitch and yaw, known as polar motion or polar diagram, is drawn in red.

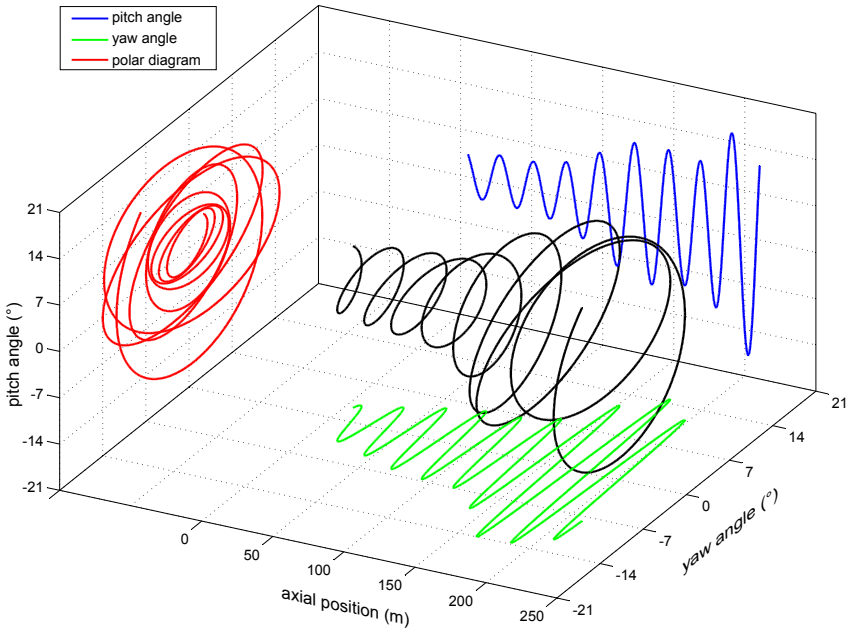

Figure 4.9: Evolution of Euler angles of a spinning case at $M0 = 2.0$, $\alpha 0 = 0°$ (test case 2)

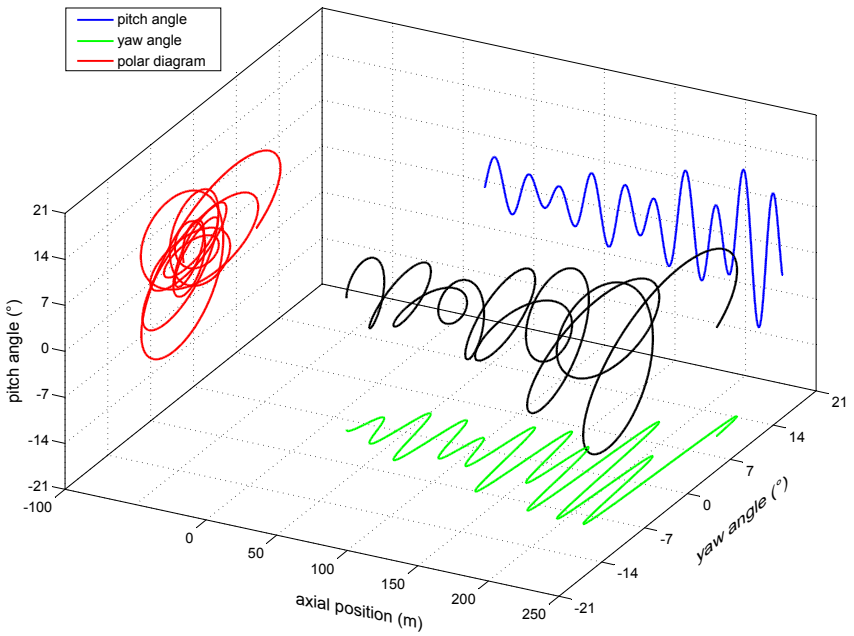

Figure 4.10: Evolution of Euler angles of a spinning case at $M0 = 3.0$, $\alpha 0 = 0°$ (test case 4)

For test case 2, the model starts to oscillate from small angles equal to about 3 degrees to larger angles equal to about 15 degrees at the end of the flight. The shape of the polar diagram can be compared to an undamped linear epicycles with loops over the origin that looks like an epitrochoid. For test case 4, the model seems to behave the same way as for test case 2, starting from small to large angles but more randomly. In this case the polar diagram looks more like an hypotrochoid. Usually, hypotrochoid motions are more representative of fin stabilized shells while spin stabilized shells behave more like epitrochoids.

4.1.3 Parametric estimation of the aerodynamic coefficients

As mentioned in Chapter 3 Section 3.4.3, the *a posteriori* identifiable vector $\mathbf{p}_2$ is composed of seven or nine initial conditions, depending on the used approach by integrating or not the *a priori* knowledge, and eight model parameters describing the drag and pitch damping coefficients, given as follows

$$\mathbf{p}_{a,2} = [\mathbf{p}_{D,2}, \mathbf{p}_{mq,2}] = [C_{D0}, C_{D1}, C_{D2}, C_{mq0}, C_{mq1}, C_{mq2}, C_{mq3}, D_\alpha] \tag{4.2}$$

One of the main objective of the present study was to identify of the aerodynamic coefficients based on multiple data series. Therefore, only the second step of the estimation task discussed in Section 3.5 will be presented and concerns the parametric estimation of the aerodynamic coefficients obtained through the multiple fit strategy. The aerodynamic characteristics are determined from five different experimental tests presented in Table 1.4 for a Mach number ranging between 0.9 and 3.0 with initial angles of attack $\alpha 0$ of 0° and 3°. The measurements obtained during these five trials have been used to estimate the *a posteriori* identifiable parameters $\mathbf{p}_{a,2}$ and validate the proposed polynomial descriptions of the aerodynamic coefficients.

4.1.3.1 Drag coefficient

The model parameters $\mathbf{p}_D$ describing the drag coefficient C_D in equation (2.34) can be estimated based on radar data. As a reminder of identifiability results, the parameter C_{D4} is not sensitive enough to influence the radar data and is fixed to zero. However, only the parameter set $[C_{D0}, C_{D1}, C_{D2}]$ verifies the second condition of the identifiability analysis and can be simultaneously estimated. As the radar data is also sensitive to the remaining parameters $[C_{D3}, C_{D5}]$, an iterative estimation was used to identify also parameters depending on the total angle of attack. That allows to refine the tendency of the drag coefficient *w.r.t.* the influential variable α_t.
The evolution of the drag coefficient C_D is represented in Figures 4.11. The estimated drag coefficient values, plotted in full lines, varying between 1.3 and 1.55, can be explained by the large velocity decrease during the flight as already observed in Figures 4.2 and 4.3. In Figure 4.11a, the drag coefficient is presented as a function of the Mach number, for constant total angles of attack. As expected, the drag coefficient is maximum for $\alpha_t = 0^\circ$ and tends to decrease with increasing total angle of attack. For each constant α_t, one can observe that C_D is roughly constant over the studied flow regimes with a maximum around M=2.0. The obtained results are compared to CFD predictions, displayed in dotted lines. One can see that CFD predictions indicate a shift at $M = 1.5$ whereas the estimated coefficient shows a variation in tendency at $M = 1.5$ but also around $M = 2.0$. Indeed, this can be explained by the fact that among all the test cases used for the multiple fit estimation only two test cases with an initial Mach number of 3.0 influence the drag coefficient in the Mach range between 2.0 and 3.0. Figure 4.11b represents the drag coefficient as a function of the total angle of attack for constant Mach numbers. The estimated drag coefficient is decreasing with increasing total angle of attack and the maximum drag values is observed for M=2.0. Despite a small difference in magnitude between CFD and the current results, the estimated coefficient has a similar tendency and results are consistent with *a priori*

knowledge. This means that the polynomial description of the drag coefficient is representative enough of the expected values.

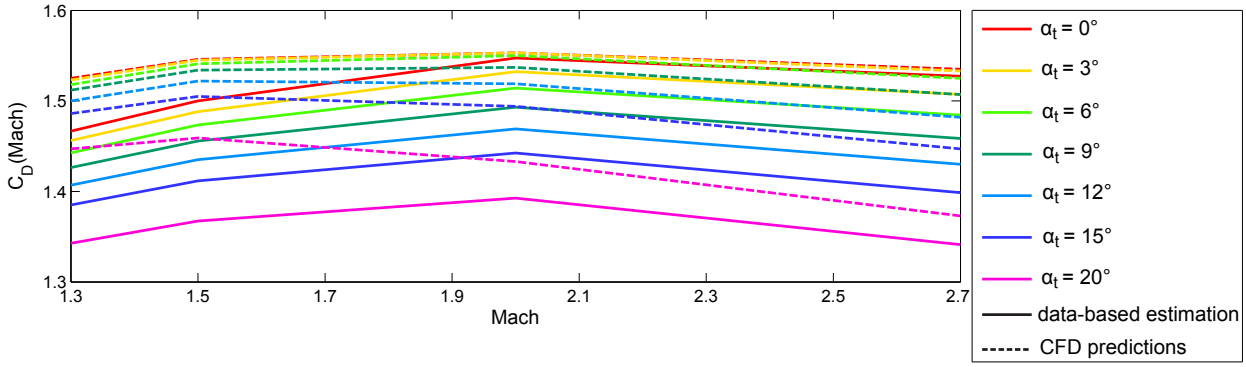

(a) C_D expressed as a function of M for constant α_t

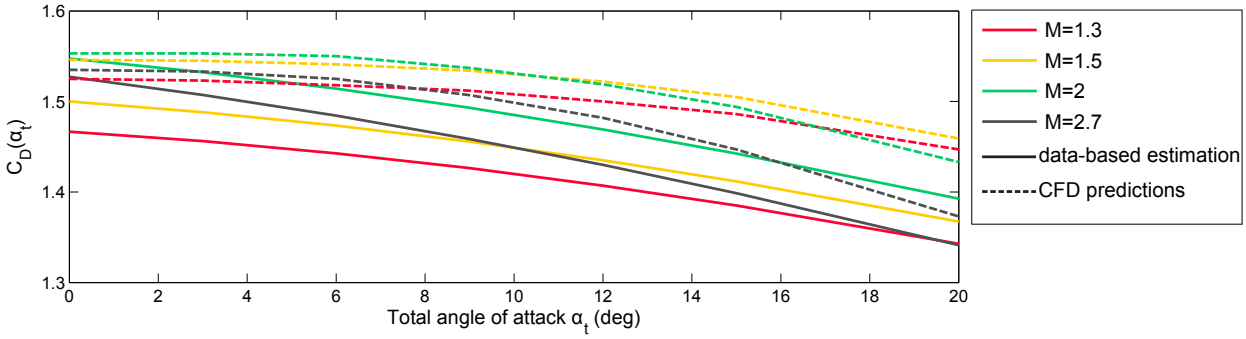

(b) C_D expressed as a function of α_t for constant M

Figure 4.11: Estimated drag coefficient C_D based on multiple data series compared to CFD predictions

4.1.3.2 Pitch damping coefficient

The model parameters $\mathbf{p}_{mq}$ describing the pitch damping coefficient C_{mq} in equation (2.37) can be estimated based on the 3D magnetometer data. As a reminder of identifiability results, C_{mq4} can be fixed to zero due to its negligible influence on the magnetometers as already explained in Chapter 3 Section 3.4.3.2. The remaining pitch damping coefficient parameters $[C_{mq0}, C_{mq1}, C_{mq2}, C_{mq3}, D_\alpha]$ are considered *a posteriori* identifiable from magnetometer data.

The estimated values of the pitch damping coefficient C_{mq} are represented in Figures 4.12. Such a representation of the pitch damping coefficient gives an indication on the dynamic stability of a vehicle in flight. Positive C_{mq} values indicate a dynamically unstable vehicle while negative values imply a dynamically stable vehicle.

It has to be noted that to estimate the pitch damping coefficient C_{mq}, several constraints were imposed on the values of the parameters $\mathbf{p}_{mq}$. This constraint envelope, displayed in dotted lines, is illustrated in Figures 4.12 and are considered sufficiently reasonable and representative of the expected values without being too restrictive. In Figure 4.12b, it may be noted a change in the envelope tendency at $M = 2.5$, mainly due to the variable $M^* = M - M_{ref}$ in the C_{mq} description in equation (2.37) that depends of the constant term $M_{ref} = 2.5$.

The evolution of the pitch damping coefficient C_{mq} shows that the dynamic instabilities are a complex function of Mach number and incidence. Indeed, in Figure 4.12a that shows the pitch damping coefficient plotted as a function of the total angle of attack for constant Mach numbers,

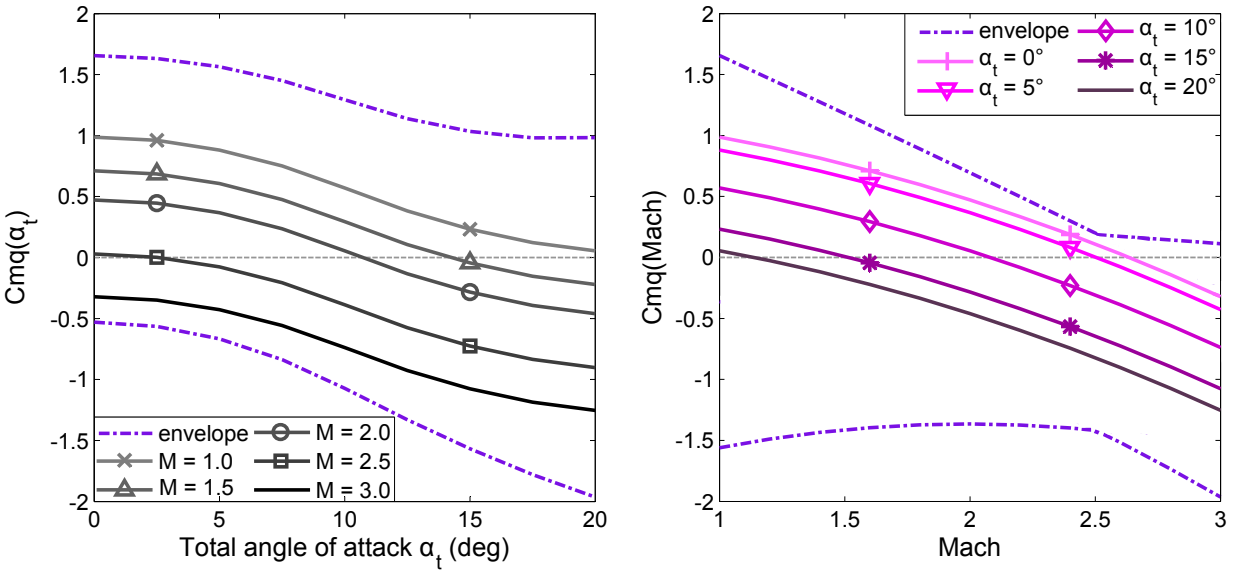

(a) C_{mq} expressed as a function of α_t for constant M

(b) C_{mq} expressed as a function of M for constant α_t

Figure 4.12: Estimated pitch damping coefficient C_{mq} based on multiple data series and the lower and upper curves of the constraint envelope

one can note that models are dynamically unstable at M=1.0 and for all angles of attack. With increasing the Mach number, dynamic stability is increasing and become neutrally or completely stable for M=2.5 and M=3.0. These results are confirmed in Figure 4.12b where the C_{mq} coefficient is plotted as a function of the Mach number for constant total angles of attack. Models stay dynamically unstable for Mach numbers smaller than 2.0 and for α_t less than 10 degrees. For $\alpha_t = 20°$, models are dynamically or neutrally stable except for $M \leq 1.15$. This behaviour is consistent with the expected tendency already observed during previous studies on the dynamic stability performed for different blunt atmospheric re-entry configurations [Schoenenberger et al. (2009), Winchenbach et al. (2002)].

4.2 Projectile

Several free flight tests were carried out at the ISL open range test site with the Basic Finner projectile, as summarized in Table 1.5. Initial Mach numbers were equal to 1.3, 1.8 and 2.6, with initial angles of attack $\alpha 0$ of 0° and 4°, fin cant angles of 0° and 2° and two different center of gravity positions X_{cg1} and X_{cg2}. The following results are presented in a similar manner than for the space probe. Five test cases were selected:

- test case 1: a non spinning projectile with $M0 = 2.6$, $\alpha 0 = 4°$, $\delta = 0°$ and X_{cg2};
- test case 2: a spinning projectile with $M0 = 2.6$, $\alpha 0 = 0°$, $\delta = 2°$ and X_{cg1};
- test case 3: a spinning projectile with $M0 = 2.6$, $\alpha 0 = 4°$, $\delta = 2°$ and X_{cg1};
- test case 4: a spinning projectile with $M0 = 1.8$, $\alpha 0 = 4°$, $\delta = 2°$ and X_{cg1};
- test case 5: a spinning projectile with $M0 = 1.8$, $\alpha 0 = 4°$, $\delta = 2°$ and X_{cg2};

Two examples of measured signals are presented. Figures 4.13 and 4.14 show the evolution of the velocity as well as the axial and two radial magnetometers signals as a function of time for test case 1 and test case 4, respectively. The range of variation of the signal amplitude corresponds to supply voltage varying from 0 to 3.3 volts in Figure 4.13 and from 0 to 5 volts in Figure 4.14.
In both cases, it can be observed that the velocity decrease is very small on the flight path time, and is of 93 m/s for test case 1 and of 95 m/s for test case 4. This decrease is due to the low drag that exhibits projectiles. The difference in flight time between the two test cases over an equal flight distance is due to the lower initial Mach number for test case 4.
The magnetic signals give exactly the same information as for the space probe. Figure 4.13 represents magnetometer signals of a non spinning projectile having a fin cant angle $\delta = 0°$. The small slope of the radial signals indicates that the model is rotating but at a very slow spin rate of about 143 rpm that could be induced by disturbances occurring during the phase of sabot separation. Figure 4.14 shows the magnetometer signals for a spinning case with fins canted at $\delta = 2°$. In this case, rotation of 6684 rpm is well indicated by the high frequency of the attitude of the radial output signals.

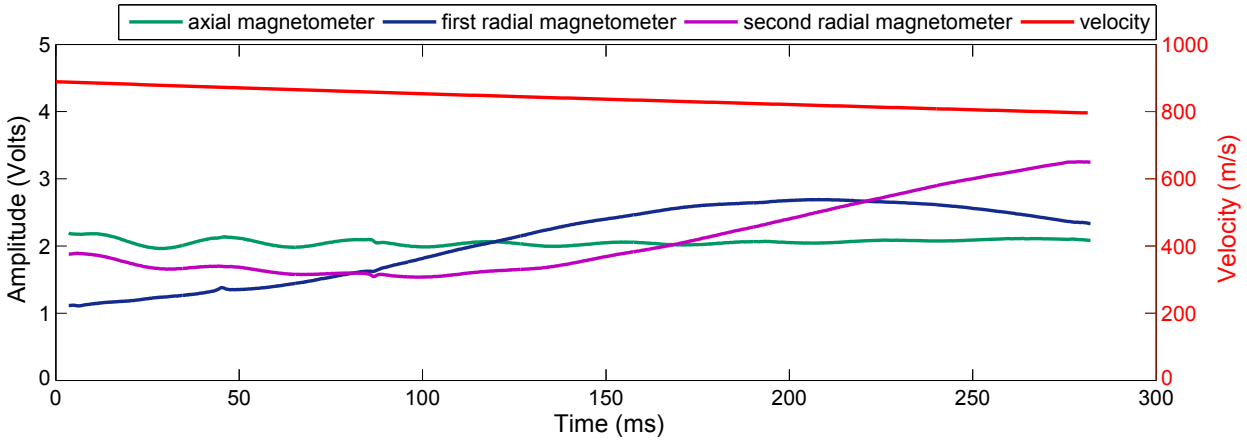

Figure 4.13: Evolution of magnetometer and radar signals of a non spinning projectile at $M0 = 2.6$, $\alpha 0 = 4°$, $\delta = 0°$, X_{cg2} (test case 1)

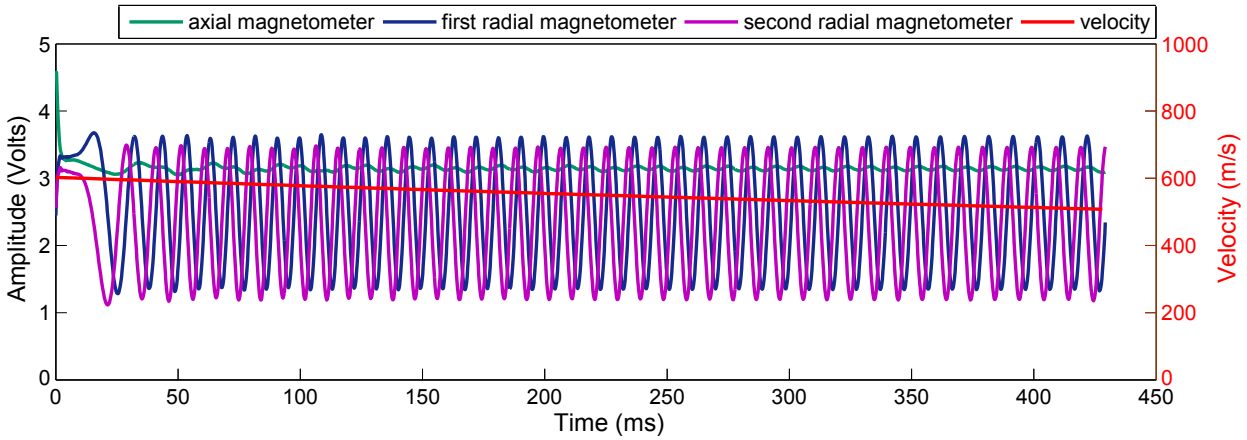

Figure 4.14: Evolution of magnetometer and radar signals of a spinning projectile at $M0 = 1.8$, $\alpha 0 = 4°$, $\delta = 2°$, X_{cg1} (test case 4)

4.2.1 Model's ability to reproduce the measured output signals

Based on the measured data, the estimated parameters are simulated in the nonlinear model and the model outputs are compared to the measured outputs.
Radar data is mainly influenced by the initial velocity V_0 and the drag coefficient. In this sense, the simulated velocity is compared to the radar measurement after the estimation of the initial velocity for each trial and of the drag coefficient parameters based on a multiple fit strategy. For illustrative purposes, a comparison between the velocity model output and the radar measurement is presented in Figure 4.15 for test case 2 with the associated output residual.

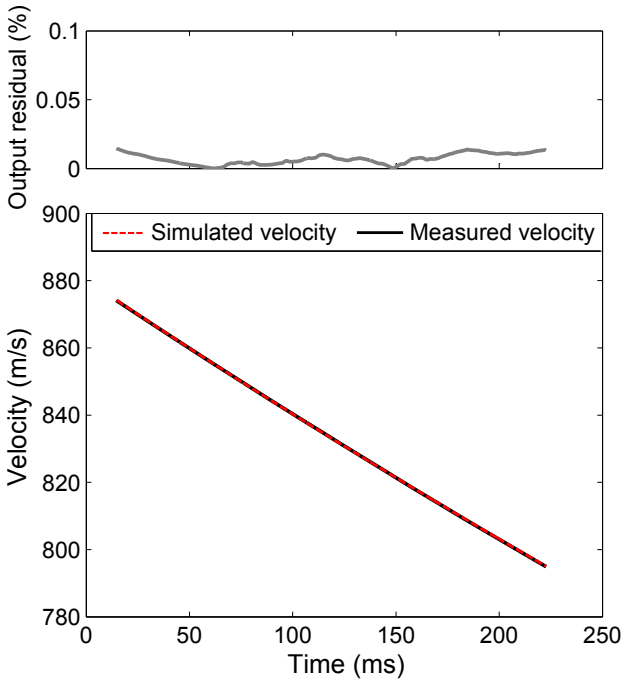

Figure 4.15: Simulated and measured velocity of a spinning case at $M0 = 2.6$, $\alpha 0 = 0°$, $\delta = 2°$, X_{cg1} (test case 2) and the associated output residual

By considering equation (4.1) and the four test cases with a fin cant angle of 2° (test cases 2 to 5), $\bar{J}_N(\mathbf{p}_D)$ is equal to 0.045. The cost function values for each test case are presented in Table 4.2.

These errors between the measured and simulated velocity are very small compared to the order of magnitude of the velocity.

	test case 2	test case 3	test case 4	test case 5
$J_i(\mathbf{p}_D)/N_i$	0.0035	0.0081	0.0151	0.0188

Table 4.2: Cost function between simulated and measured velocity of the four test cases

The comparison between the measured and the simulated magnetometer signals for test case 1 is presented as a function of time in Figure 4.16a for the axial magnetometer, in Figure 4.16b for the first radial magnetometer and in Figure 4.16c for the second radial magnetometer. The same comparison between the measured and the simulated magnetometer signals, for test cases 2 and 5 are presented in Figures 4.17 and 4.18, respectively. For the three test cases, their associated output residuals are shown on the top of these figures.

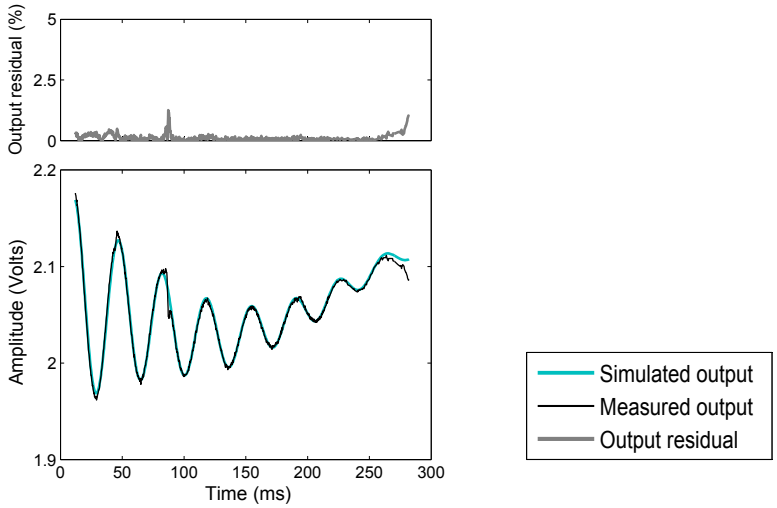

(a) Axial magnetometer

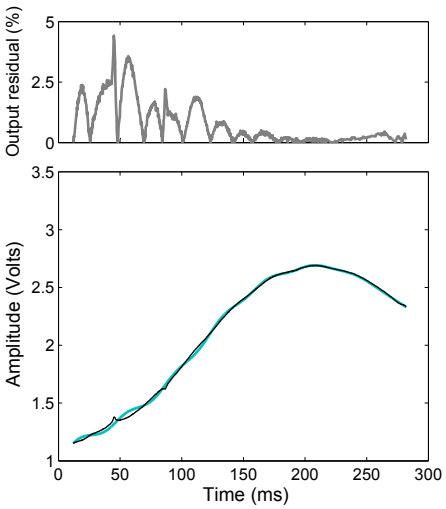

(b) First radial magnetometer

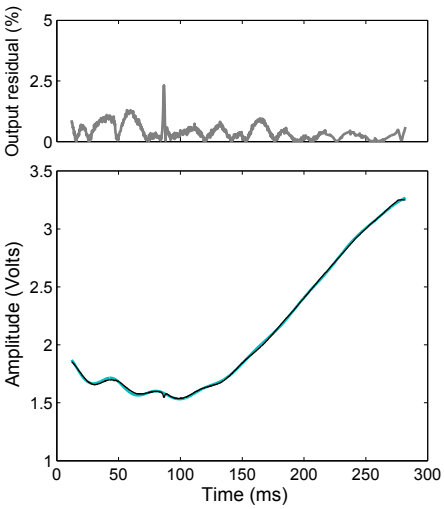

(c) Second radial magnetometer

Figure 4.16: Simulated and measured magnetometer signals of a non spinning case at $M0 = 2.6$, $\alpha 0 = 4°$, $\delta = 0°$, X_{cg2} (test case 1) and the associated output residuals

For the non spinning test case 1, the fit between the measured and the simulated axial signals in Figure 4.16a is very good except at the time where the measured signals are slightly disturbed by the presence of the sky screens and represented by small peaks. The output residuals between the measured and the simulated magnetometer signals are higher for the radial magnetometers than for the axial magnetometer, as observed in Figures 4.16b and 4.16c. Despite this difference, the agreement between the measured and the simulated radial magnetometers can be considered as very good.

For the spinning test case 2 shown in Figures 4.17, output residuals are a bit larger at the beginning of the flight. However, for all magnetometers the differences between measured and simulated signals remain very small, and the fits can also be considered as very good.

For the spinning test case 5 shown in Figures 4.18, the amplitude variations are larger than for test cases 1 and 2 due, in this case, to the maximum power supply voltage set at 5 volts. As for the previous test cases, output residuals are again very small and the fit is sufficient for the determination of the angular motion history.

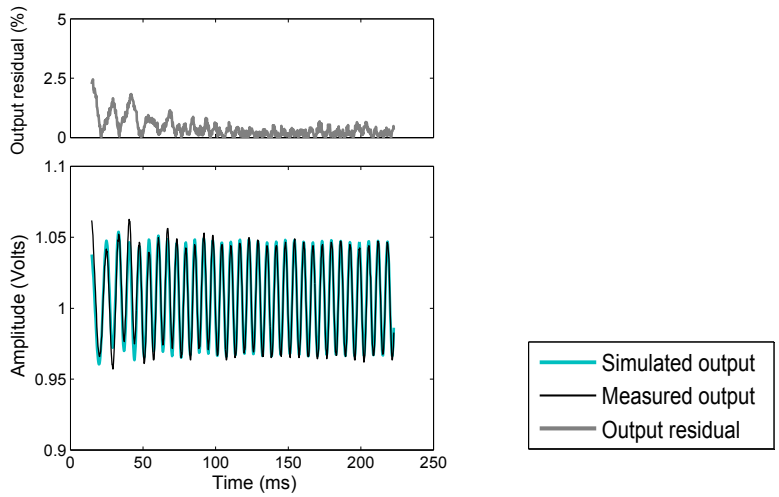

(a) Axial magnetometer

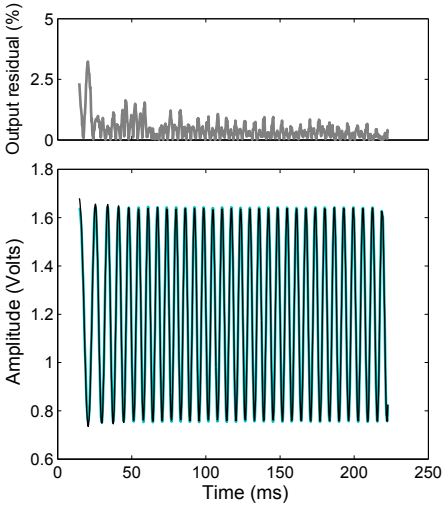

(b) First radial magnetometer

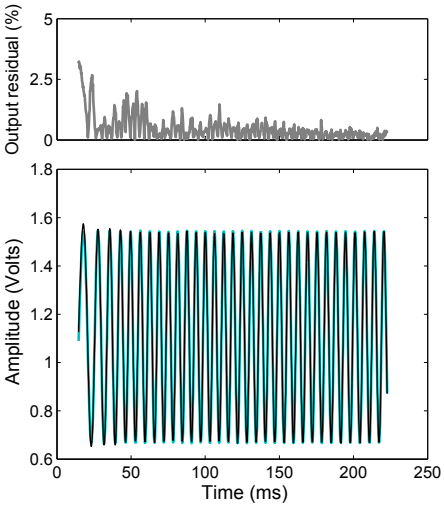

(c) Second radial magnetometer

Figure 4.17: Simulated and measured magnetometer signals of a spinning case at $M0 = 2.6$, $\alpha 0 = 0°$, $\delta = 2°$, X_{cg1} (test case 2) and the associated output residuals

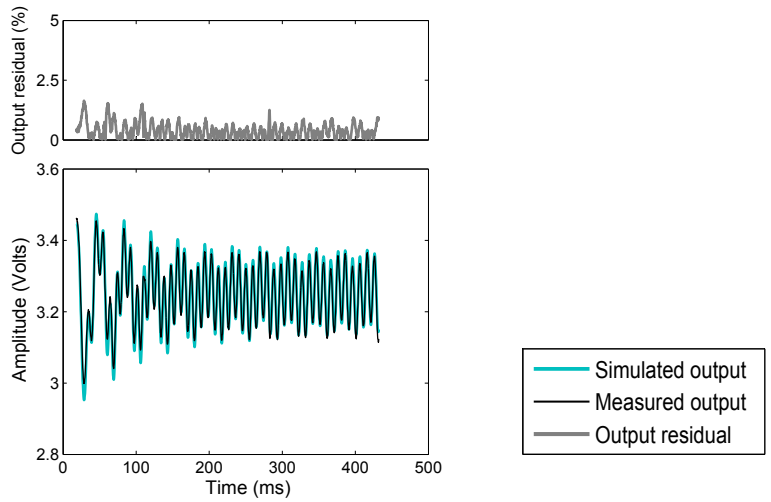

(a) Axial magnetometer

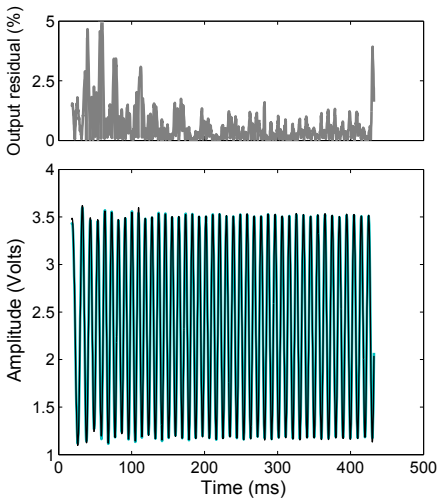

(b) First radial magnetometer

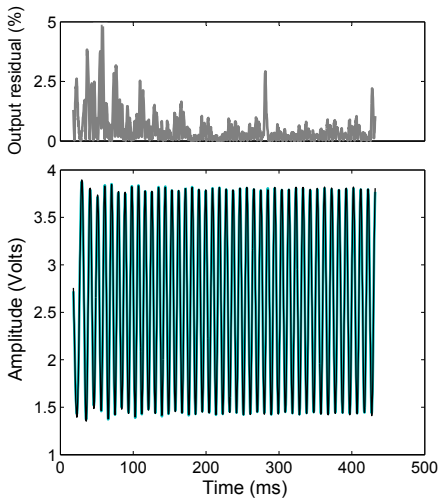

(c) Second radial magnetometer

Figure 4.18: Simulated and measured magnetometer signals of a spinning case at $M0 = 1.8$, $\alpha 0 = 4°$, $\delta = 2°$, X_{cg2} (test case 5) and the associated output residuals

4.2.2 Evolution of the state variables

4.2.2.1 Total angle of attack and Mach number

The evolution of the total angle of attack α_t and the Mach number profile as a function of time are illustrated for test cases 1, 2 and 5 in Figures 4.19, 4.20 and 4.21, respectively. For all three cases, one can observe a linear velocity decrease with a very small difference in Mach number that is equal in average to about 0.25.

By comparison of the three figures, evolution of the total angles of attack α_t indicates a fast damping and is decreasing along the flight path, from $\alpha_t = 6.71°$ to $\alpha_t = 0.38°$ for test case 1, from 1.35° to 0.03° for test case 2 and from 11.04° to 0.4° for test case 5.

These evolutions represent a behaviour of statically stable projectiles. The difference in the total angle of attack amplitude at the beginning of the flight between test case 1 and test case 2 is due to the initial angle of attack $\alpha 0$. The difference between test case 1 and test case 5 is due to the higher initial disturbances occurring at lower Mach numbers. Despite the different flight time between all cases, one can note that the frequency of the angle of attack is equivalent between the non spinning case and the spinning cases.

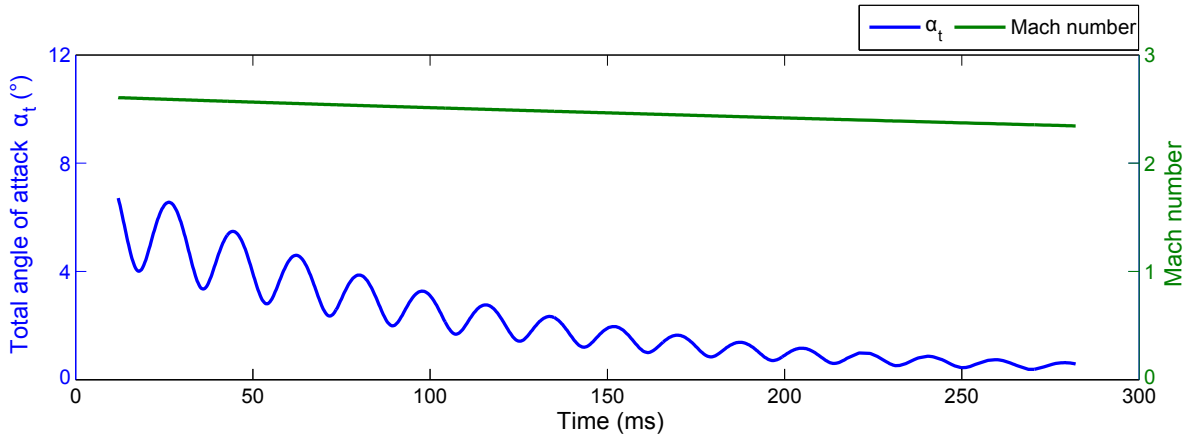

Figure 4.19: Evolution of the total angle of attack and the Mach number of a non spinning case at $M0 = 2.6$, $\alpha 0 = 4°$, $\delta = 0°$, X_{cg2} (test case 1)

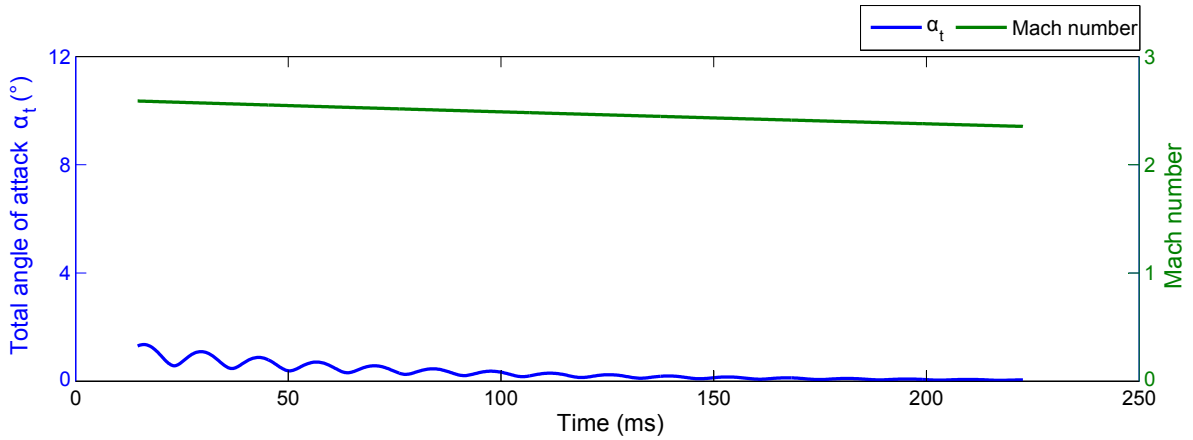

Figure 4.20: Evolution of the total angle of attack and the Mach number of a spinning case at $M0 = 2.6$, $\alpha 0 = 0°$, $\delta = 2°$, X_{cg1} (test case 2)

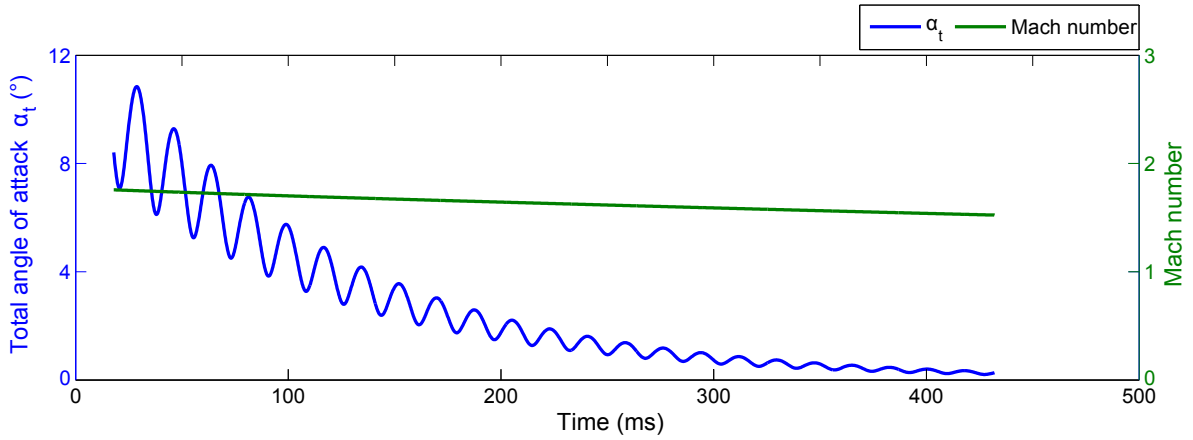

Figure 4.21: Evolution of the total angle of attack and the Mach number of a spinning case at $M0 = 1.8$, $\alpha 0 = 4°$, $\delta = 2°$, X_{cg2} (test case 5)

4.2.2.2 Polar motion

Figures 4.22, 4.23 and 4.24 show, in black, the three dimensional plots of the angular motion as a function of axial position x_E for test cases 1, 2 and 5, respectively. The attitude components, i.e. pitch and yaw angles, are displayed in blue and green lines, respectively. The two dimensional projection, known as polar motion or polar diagram, is shown in red.

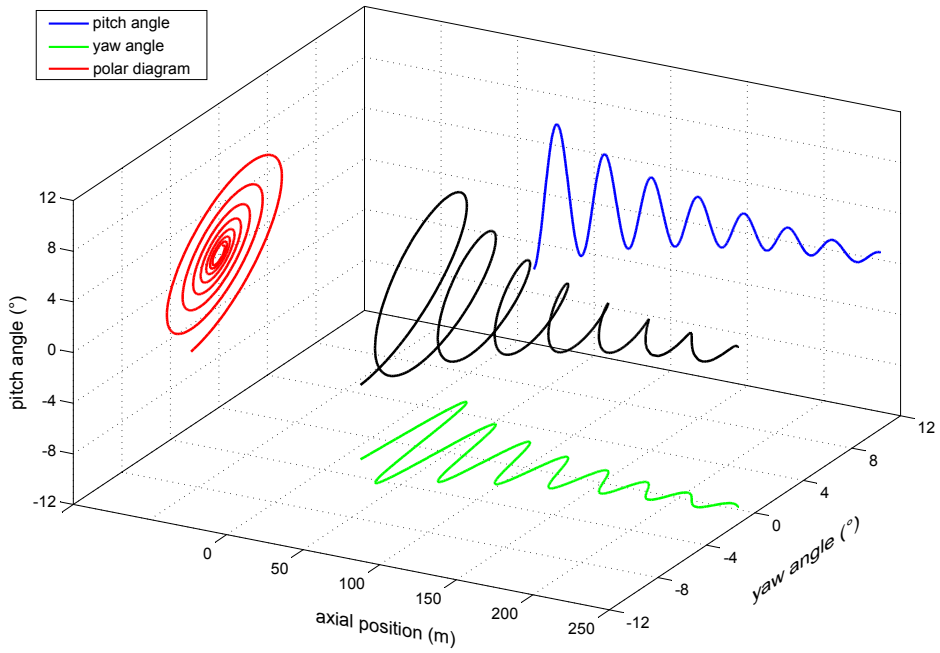

Figure 4.22: Evolution of Euler angles of a non spinning case at $M0 = 2.6$, $\alpha 0 = 4°$, $\delta = 0°$, X_{cg2} (test case 1)

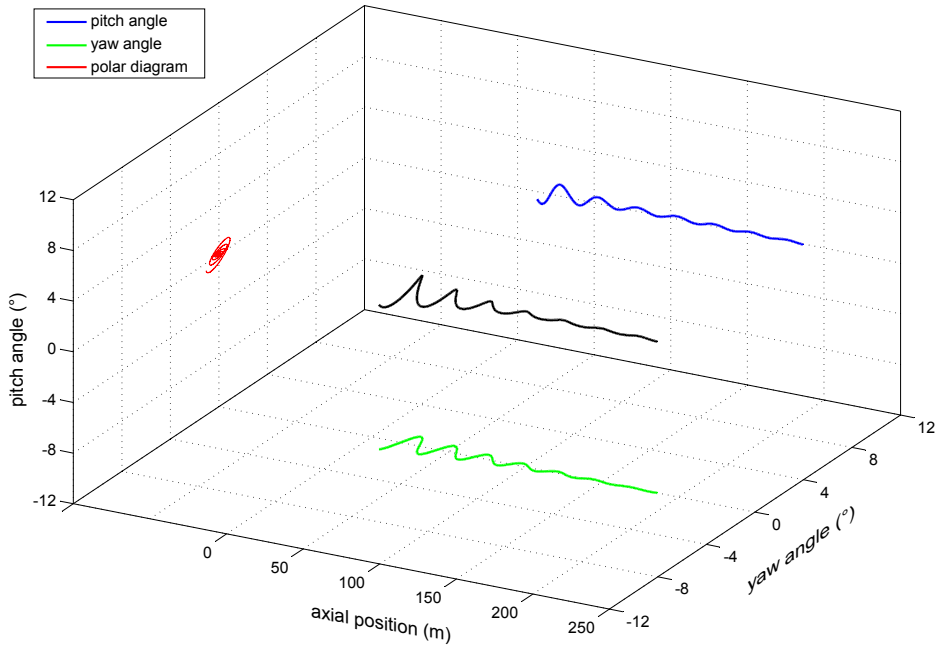

Figure 4.23: Evolution of Euler angles of a spinning case at $M0 = 2.6$, $\alpha 0 = 0°$, $\delta = 2°$, X_{cg1} (test case 2)

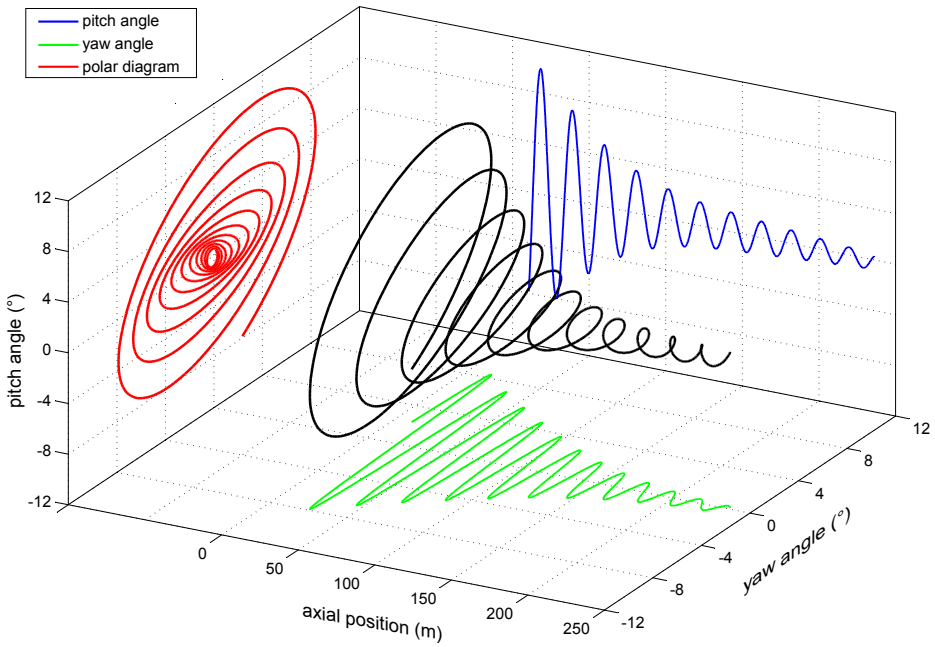

Figure 4.24: Evolution of Euler angles of a spinning case at $M0 = 1.8$, $\alpha 0 = 4°$, $\delta = 2°$, X_{cg2} (test case 5)

For the three test cases, the range of variation of the pitch and yaw angles are equivalent to their respective total angles of attack evolution. The polar motion is representative of a stable projectile with a fast damped circular conical motion around the origin of the Earth coordinate system. The same trend is observed for non spinning and spinning cases.

4.2.2.3 Comparison with complementary methods

For the projectile studies, the 3D high speed video system, presented in sub-section 1.4, was used. This system was designed and developed not only to determine the attitude but also the 3D position of the vehicle along the flight path. The principle is to simultaneously capture sequences of images from both trackers, analyzed afterwards by image processing. In this sense, the position and the attitude, i.e. Euler angles θ and ψ, of the projectile in free flight can be determined. This complementary knowledge about the projectile behaviour in flight makes it possible to validate the results obtained from the on-board sensor technique. By extracting the position, the flight path γ and heading ξ angles can be determined. Relations between these angles with incidence and Euler angles can be formulated as $\alpha = \theta - \gamma$ and $\beta = \xi - \psi$ [Stengel (2004)]. This simplification is valid only when no rotation is observed and then, ϕ near of zero. In this sense, the comparison is done for the non spinning case 1. Figure 4.25 shows snapshots of the sabot separation extracted from the two trajectory trackers and Figures 4.26 present an example of a picture extracted from a high speed video tracker, in Figure 4.26a before image processing and in Figure 4.26b after image processing. Details of the image processing procedure used for this application are given in [Portier (2014)].

Figures 4.27 show the axial position x_E obtained by image processing from the 3D high speed videos analysis and from radar signal. In Figure 4.27a, the axial position as a function of time is represented on the complete flight path while in Figure 4.27b, an enlarged view of the left bottom corner of Figure 4.27a is shown, indicated by the little square. A very good agreement is observed between the measured and determined position and the position determined from the two cameras can be considered as satisfactory.

Figure 4.25: Snapshots of sabot separation obtained from the two trajectory trackers

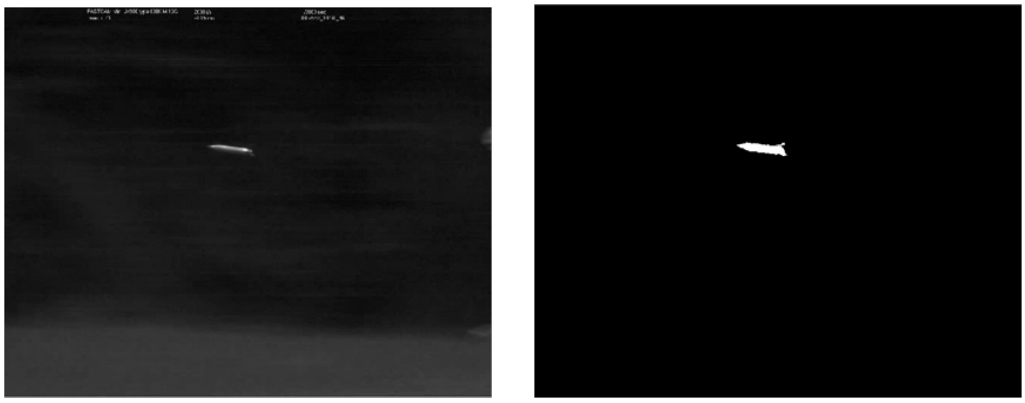

(a) Before image processing (b) After image processing

Figure 4.26: Example of a picture extracted from a high speed video tracker

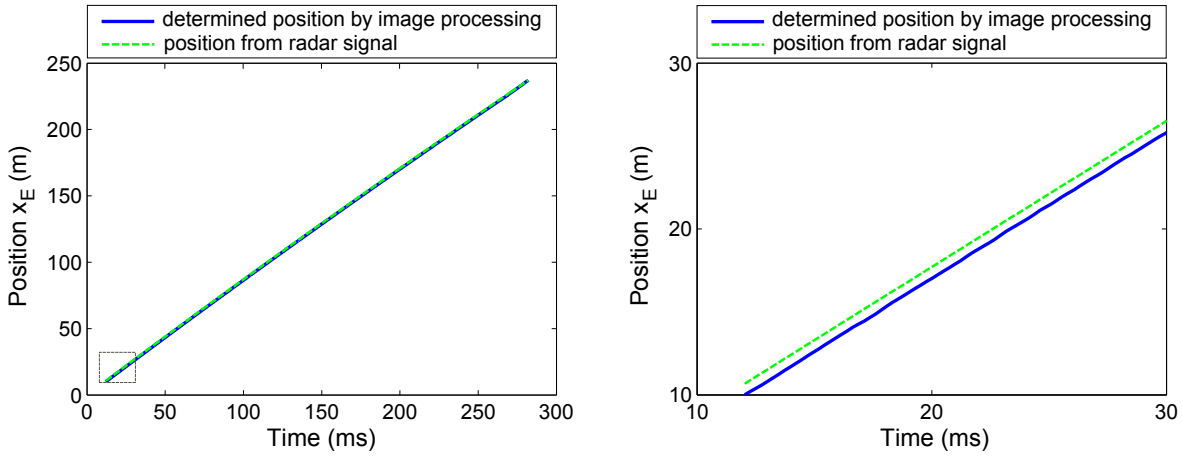

(a) Axial position (b) Enlarged view of the axial position

Figure 4.27: Comparison of the axial position determined by image processing and from radar signal

Figure 4.28 presents the comparison between the simulated pitch angle θ based on 3D magnetometer data and the results obtained by image processing of the 3D high speed videos. A small shift can be observed, mainly due to the difficulty to exactly synchronize the initial time of the cameras and the sensor signals. However, these results are coherent in phase and magnitude and confirm for the future that the two techniques are complementary.

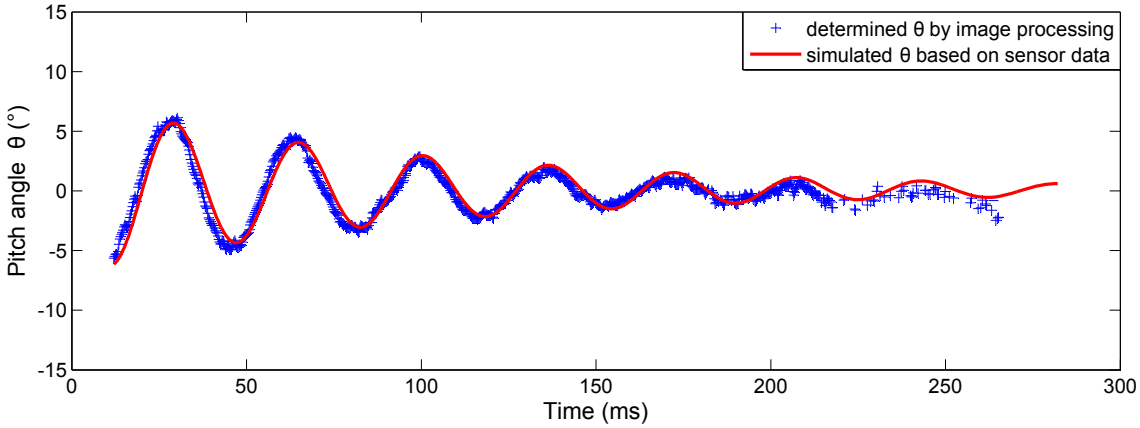

Figure 4.28: Comparison of the pitch angle determined by image processing and simulated from sensor data

4.2.3 Parametric estimation of the aerodynamic coefficients

The first results of aerodynamic coefficient estimation were presented in [Albisser et al. (2014)], based on the free flight data set available at the time. During the last year, additional trials, presented in Table 1.5, were carried out at the ISL open range test site to complete the test matrix and used for the aerodynamic coefficient estimation. Estimation results for projectiles with fins canted at 2° will only be presented in this sub-section.

The aerodynamic coefficients are described in a polynomial form as a function of the Mach number and the total angle of attack, as presented in equations (2.38-2.43). However, two main elements can be pointed out to query the use of a polynomial description and a multiple fit strategy for the aerodynamic coefficient estimation, based on the available test cases. Due to the very low velocity decrease already observed in Figures 4.13 and 4.14 on the flight path, a large amount of experiments for different initial Mach numbers should be conducted to increase the covered Mach number range and precisely determined the aerodynamic coefficients from a multiple fit estimation, especially in the transonic phase. In free flight it is well known that the transonic flow regime is characterized by highly nonlinear aerodynamic coefficients that can exhibit special features in the range of Mach numbers between 0.8 and 1.2. Therefore and in order to detect accurately some of the transonic phenomenon, if existing, multiple trials need to be performed in a domain as large as possible that covers the transonic Mach numbers. However, in the frame of this study, only experiments with three different initial Mach numbers of 1.3, 1.8, 2.6 were carried out and thus, the available test cases do not cover enough Mach number values to represent with enough accuracy the transonic phase. Moreover, as observed in Figures 4.19 to 4.21, the total angle of attack decreases quickly along the flight path and due to its small values, the impact of the terms dependent of this variable in the polynomial description can be neglected compared to those dependent on the Mach number.

Even if no identifiability studies were performed for the projectile case, the same conclusions as for the space probe can be done in terms of influential parameters, namely V_0 and C_D mainly influence the radar signal and the magnetometer signals are sensitive to the moment coefficients. Therefore, to analyze if the available data is sufficient for a multiple fit estimation based on a

polynomial description of the aerodynamic coefficients, it was in a first time tested and applied to the drag coefficient estimation from the radar data of test cases with $\delta = 2°$.

The other aerodynamic coefficients were estimated from the magnetometer data by considering each trial independently. Several free flight tests at $M0 = 1.3$, 1.8 and 2.6 and $\delta = 2°$ were considered for the aerodynamic coefficient estimation. Each coefficient was determined in a tabular form for fixed Mach numbers. As the Mach number decrease is very small over the full flight time, estimated coefficients of each free flight test case are given only for an averaged Mach number, representative enough of the entire flight. These results are presented in Table 4.3 and illustrated in Sections 4.2.3.2 to 4.2.3.5. A distinction is made between the estimated coefficients from test cases with a center of gravity position X_{cg1} defined by yellow markers and those with a center of gravity position X_{cg2} defined by blue markers. Comparisons are also made with previous free flight (FF) tests results from single and multiple fit [Dupuis and Hathaway (1997), Dupuis (2002)], wind tunnel tests (WT) [Dupuis (2002)], PRODAS and CFD predictions.

	Averaged Mach number	C_{lp}	$C_{l\delta}$	$C_{m\alpha}$	C_{mq}
Test cases with a c.g. position X_{cg1} (●)	1.25	-23.69	10.40	-36.70	-432.31
	1.77	-22.37	11.06	-24.93	-417.87
	1.79	-23.09	11.26	-23.40	-382.20
	2.59	-14.52	7.38	-11.98	-368.69
	2.61	-15.30	7.38	-12.12	-382.67
Test cases with a c.g. position X_{cg2} (●)	1.27	-24.54	10.91	-34.88	-316.25
	1.76	-22.70	11.43	-19.50	-303.36
	1.80	-21.61	10.83	-20.61	-211.32
	2.47	-18.29	8.69	-7.51	-239.20
	2.54	-14.43	7.62	-8.26	-313.30

Table 4.3: Estimation results of the moment aerodynamic coefficients

4.2.3.1 Drag coefficient

The drag coefficient was the subject of an estimation investigation based on a multiple fit strategy. As mentioned previously, the velocity decay is very small over the total flight time. Due to the lack of information in the transonic flow regime to accurately characterize the evolution of the drag coefficient from multiple free flight data, only test cases with initial Mach numbers of 1.8 and 2.6 were considered.
Therefore, to estimate and validate the proposed polynomial description of the drag coefficient, C_D was determined from four experimental tests, corresponding to test case 2 to test case 5, for Mach numbers ranging between 1.52 and 2.6, with initial angles of attack of 0° and 4° and with fin cant angles of 2°.
The drag coefficient parameters $\mathbf{p}_D$ in equation (2.38) are estimated from the radar data. One can note that the estimated parameter relative to $\sin^4 \alpha_t$ is negligible compared to the other parameters, and thus, was fixed to zero.
In Figure 4.29a, the drag coefficient is expressed as a function of the Mach number, for constant angles of attack. For all α_t, the estimated values are decreasing between 1.0 and 0.5 with increasing Mach number. As expected and in contrast to the space probe application, the lowest drag was

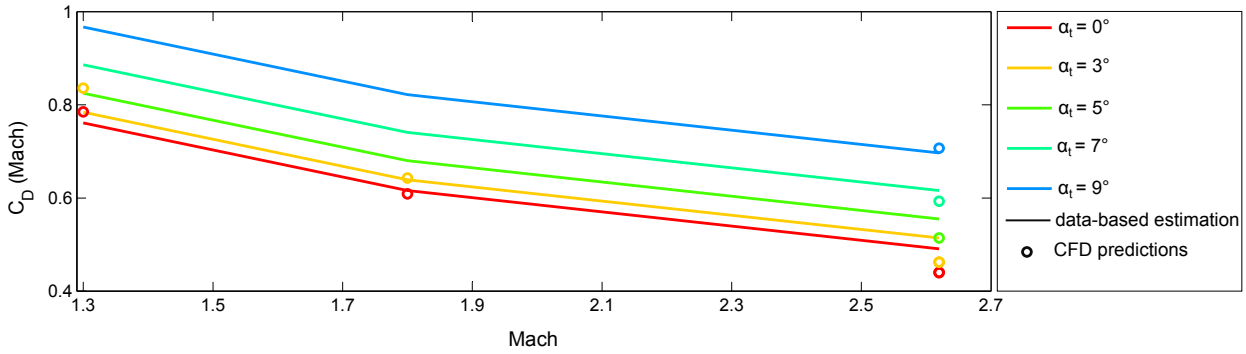

(a) C_D expressed as a function of M for constant α_t

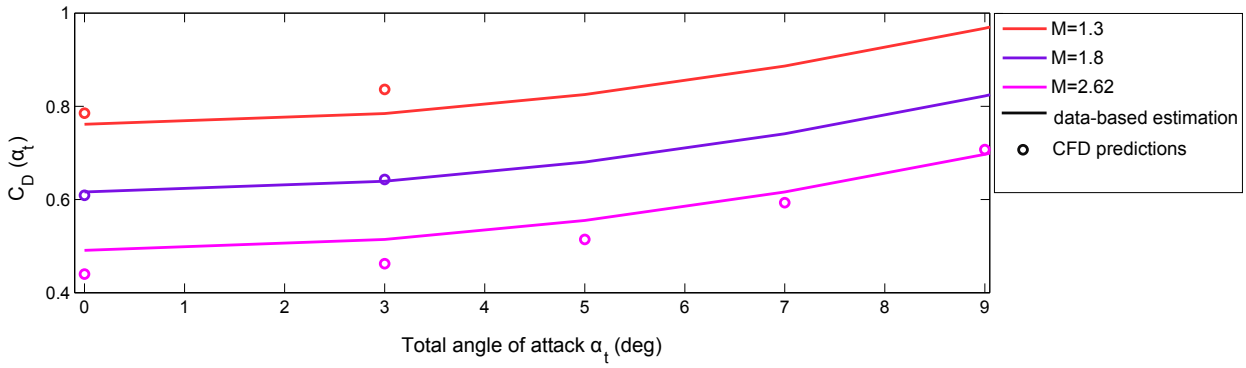

(b) C_D expressed as a function of α_t for constant M

Figure 4.29: Estimated drag coefficient C_D based on multiple data series compared to CFD predictions

obtained for $\alpha_t = 0°$. Results present a good agreement in tendency and only small differences in values can be observed compared to CFD predictions, especially for $M = 2.6$ and $\alpha_t = 0°$ and 3°. Indeed, all the theoretical cases cannot be experimented and these combinations are never represented in the experimental context.
In Figure 4.11b, the evolution of the drag coefficient is presented as a function of the total angle of attack for constant Mach numbers. For all constant M and as expected, the drag is increasing with increasing total angle of attack. For the same reasons as mentioned previously and despite a small difference in amplitude observed for M=2.62 and for α_t smaller than 5°, the comparison with the CFD predictions shows a similar tendency and a good coherence. For the selected test cases to proceed to the drag coefficient estimation based on a multiple fit strategy, the polynomial description in equation (2.38) is representative enough of the expected values in the supersonic regime.

4.2.3.2 Roll moment coefficient

The estimated roll damping coefficient C_{lp} is given in Figure 4.30 as a function of the Mach number. As expected, this coefficient is not sensitive to the center of gravity position. As already mentioned, the estimation from the free flight tests performed during this study cannot reveal the tendency described by PRODAS predictions in the transonic regime. Despite a bit of scattering around M=2.6, the present estimated values are coherent with PRODAS predictions and the single and multiple fit free flight (FF) data [Dupuis (2002)].

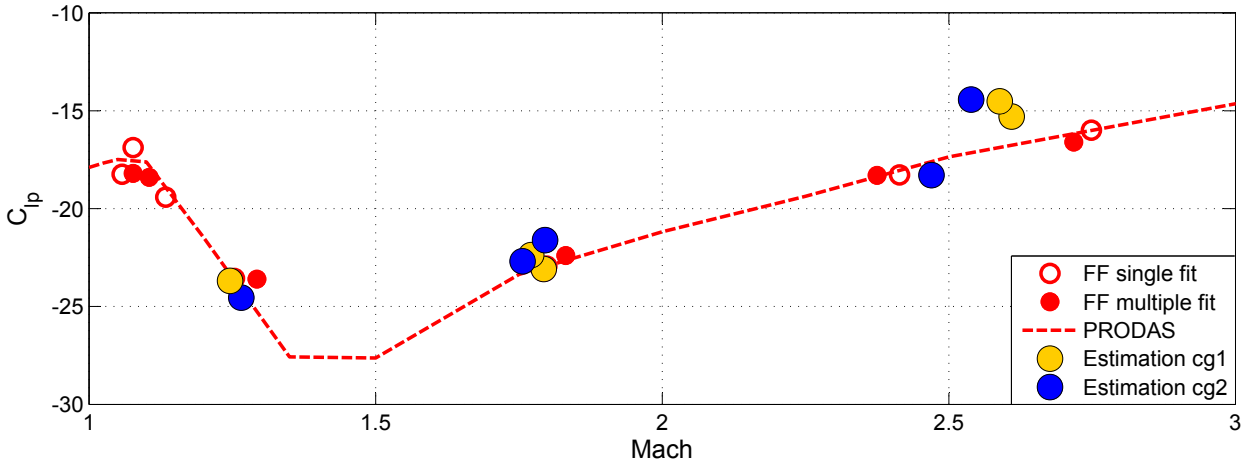

Figure 4.30: Roll damping coefficient C_{lp}

Figure 4.31 illustrates the roll moment coefficient due to fin cant $C_{l\delta}$ as a function of the Mach number. To compare the estimated results for different cant angles, $C_{l\delta}$ is given per radian. As for the roll damping coefficient, this coefficient is not sensitive to the center of gravity position. It was well determined and shows a very good agreement with results obtained from free flight and wind tunnel tests.

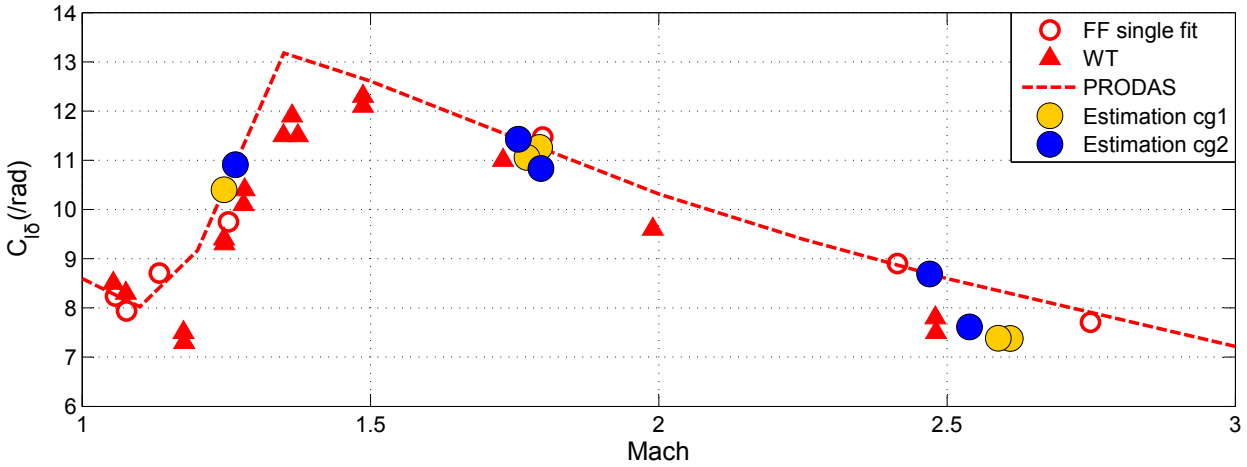

Figure 4.31: Roll moment due to fin cant $C_{l\delta}$

4.2.3.3 Pitch moment coefficient slope

The evolution of the estimated pitch moment coefficient slope $C_{m\alpha}$ *w.r.t.* the center of gravity positions X_{cg1} and X_{cg2} as a function of the Mach number is illustrated in Figure 4.32. This coefficient is representative of the static stability. Positive values reveal a statically unstable projectile while negative values imply a statically stable projectile. As expected, static stability is decreasing with increasing Mach number. This is an indication that fins become less effective for the higher Mach numbers. As it is known, this coefficient is very dependent on the center of gravity position. Indeed, a decreased stability is seen with moving the center of gravity position from 60%, corresponding to X_{cg1}, towards 65%, relative to X_{cg2}, from the nose. It is for this reason that the obtained results must be compared in values to previous one for the same center of gravity position. The available results already published in the literature are given for a center

of gravity position different of both considered in this study, and correspond to the red markers. However, they could be useful for a comparison in terms of tendency. The estimated $C_{m\alpha}$ for both center of gravity positions are coherent with PRODAS results predicted for the same center of gravity position and presents a good agreement in tendency compared to free flight and CFD results for a different center of gravity position. Differences in $C_{m\alpha}$ are well estimated and as expected decreased stability is seen with moving the c.g. position from X_{cg1} to X_{cg2}. The negative values confirm, as expected, that the projectile is statically stable for all Mach numbers.

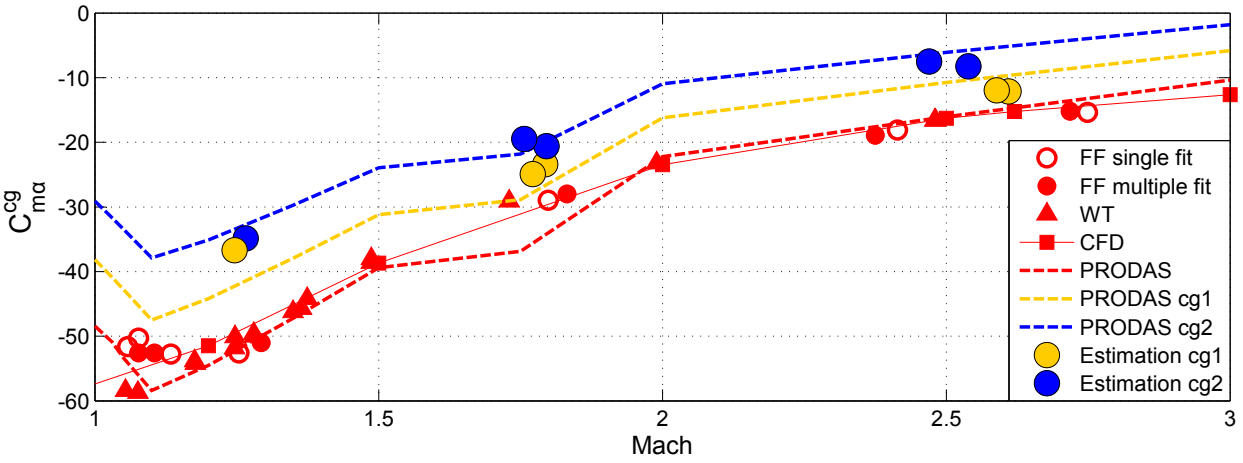

Figure 4.32: Pitch moment coefficient slope $C_{m\alpha}^{cg}$

4.2.3.4 Normal force coefficient

In exterior ballistic studies, it is more common to present the normal force coefficient slope, $C_{N\alpha} = \frac{C_N}{\sin\alpha}$ than the lift coefficient slope $C_{L\alpha}$. This is mainly due to the possibility to compare directly the results with the measured normal force from wind tunnels. For the determination of the normal force coefficient slope, two distinct methods can be used. The first one supposes its estimation based on the measurements of the forces acting on the body and that can be obtained by means of accelerometers. The second method is based on the pitching moment difference obtained from projectiles with two different center of gravity positions. As the accelerometer data were not processed in this study, the second approach was employed. In this sense, $C_{N\alpha}$ can be obtained for either rotating and/or non-rotating bodies based on the following equation

$$\frac{L}{d} \cdot C_{N\alpha} = \frac{(C_{m\alpha}^{cg1} - C_{m\alpha}^{cg2})}{(\frac{X_{cg1}}{L} - \frac{X_{cg2}}{L})} \tag{4.3}$$

where L represents the model length and d the model diameter.

Table 4.4 summarizes the normal force coefficient values determined with this method and Figure 4.33 shows the evolution of this coefficient as a function of the Mach number. As expected $C_{N\alpha}$ is decreasing with increasing Mach number. This tendency is due to the fins which become less effective when the Mach number increases. The scattering in the results at all velocities is very small and the determined coefficients agree very well with previous results obtained from free flight and wind tunnel tests, CFD and PRODAS predictions.

Mach number	1.1	1.59	1.72	2.45	2.5
$C_{N\alpha}$	21.04	13.03	11.13	9.01	10.17

Table 4.4: Determined normal force coefficient slope

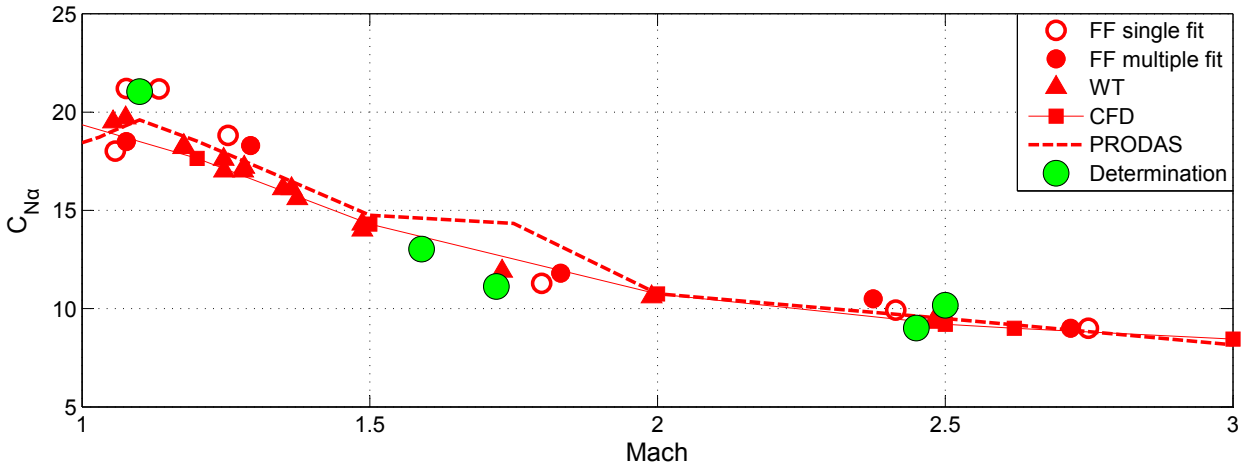

Figure 4.33: Normal force coefficient slope $C_{N\alpha}$ determined from $C_{m\alpha}^{cg1}$ and $C_{m\alpha}^{cg2}$

4.2.3.5 Pitch damping coefficient

Figure 4.34 presents the estimated pitch damping coefficient C_{mq} as a function of the Mach number. For this coefficient, dispersions are higher than for the other coefficients. This is mainly due to the fact that it is the most difficult coefficient to estimate due to its poor sensitivity to outputs. This coefficient is representative of the dynamic stability: a large negative value indicates that the projectile behaves as dynamically stable. Despite the higher scattering, the general trend can be observed. Projectiles are dynamically less stable with increasing the Mach number. As for $C_{m\alpha}$, the effect of the center of gravity position is not negligible. Indeed, projectiles are dynamically less stable when the center of gravity position is moving from 60% towards 65% from the nose. Here again, present results are consistent and agree well with already published results.

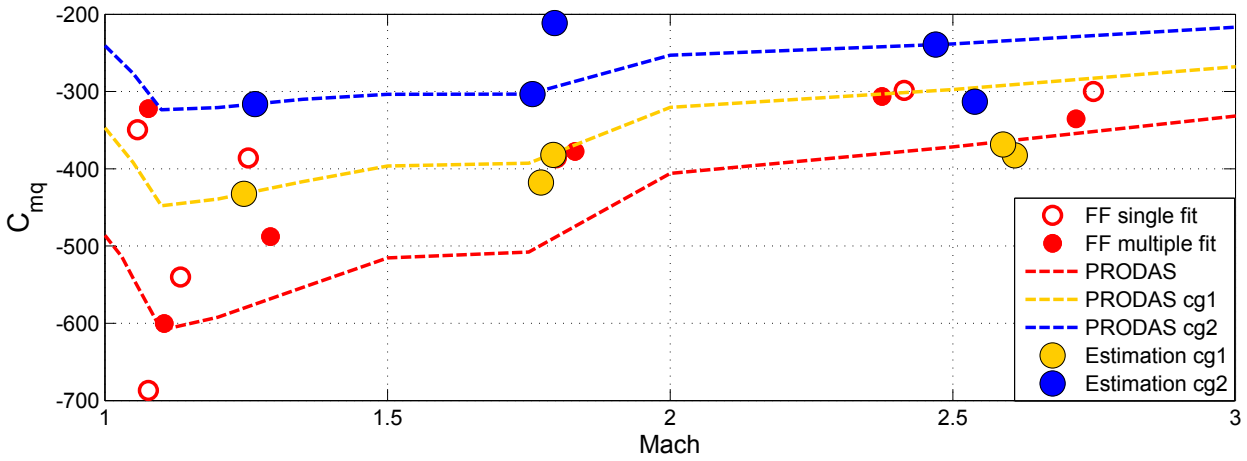

Figure 4.34: Pitch damping coefficient C_{mq}

4.3 Discussions

In this chapter, several results have been described for a space probe and a projectile. Comparisons between simulated and measured signals, parameter estimation results, as well as the evolution of state variables have been presented. The aerodynamic characteristics for the space probe and the projectile present several differences. Both architectures have their own behaviour in flight that can be highlighted:

- velocity and drag coefficient: the space vehicle velocity decreases very quickly along the flight path while the projectile velocity decay is very small. These results reveals higher drag values for the space probe than for the projectile, as seen in Sections 4.1.3.1 and 4.2.3.1. Indeed, the order of magnitude of the drag coefficient for the space probe is almost two to three times higher than for the projectile. Also for the space probe, the drag is decreasing with increasing total angle of attack while it is increasing for projectile;

- total angle of attack: for the space vehicle, the total angle of attack α_t is usually increasing along the flight path whereas α_t is decreasing for the projectile. For the first model, this variable can reach angles higher than 20° depending on the test case. For the second model, the order of magnitude of α_t is equivalent to the initial angle of attack $\alpha 0$ and it tends to decrease during the flight until values close to zero. These evolutions can be representative of the stability of both models;

- dynamic stability: the dynamic stability, represented by negative values of the pitch damping coefficient C_{mq}, is satisfied only for specific Mach numbers and total angles of attack as seen in Section 4.1.3.2. For projectiles, it is well-known that this model is perfectly stable dynamically and this was confirmed by the results shown in Figure 4.34.

- spin rate: for equivalent velocities, even if a spin is induced for the space probe, the roll rate is clearly not comparable to the projectile with canted fins;

The obtained results are perfectly coherent with *a priori* knowledge in the exterior ballistic domain and already published results in the literature, from wind tunnel measurements and/or aerodynamic predictions codes. Therefore, the developed code for the aerodynamic coefficient determination takes into account enough relevant effects to be representative of the real behaviour in flight and can be used for both architectures.
The proposed multiple fit strategy for the parameter estimation has improved the physical interpretability of the coefficients depending on Mach numbers and total angles of attack. The identified coefficients were validated for both architectures over a large range of variation of M and α_t. The aerodynamic coefficient estimation results based on a multiple fit strategy presented herein are consistent with the ones obtained previously for similar configurations. For the space probe, they essentially show that the drag coefficient is represented by a function of the Mach number and the total angle of attack with a coupling term in both variables. The pitch damping coefficient is a complex function not only of the total angle of attack, but also of the Mach number.
For the projectile, only the drag coefficient was the subject of a multiple fit strategy and C_D is mainly described as a function of the Mach number and slightly influenced by a term in α_t. For the remaining aerodynamic coefficients, a dependence only *w.r.t.* Mach numbers is representative enough of the coefficient evolution.

Conclusions and perspectives

The work presented in this thesis is associated to the exterior ballistic framework. This domain aims at studying and understanding the behaviour of a vehicle in flight through the aerodynamic coefficients characterizing it. Several complementary tools can be used to quantify the aerodynamic parameters. However, free flight tests are considered as reference because they allow to study the vehicle behaviour in flight under real conditions. This research subject deals with the identification of aerodynamic coefficients from free flight data. To bring this project to a successful end, the proposed approach consisted in a wise merging between the experimental context and the identification techniques. Thus, an identification procedure was defined to guide the aerodynamic parameter estimation, composed of several steps, from the modelling of the behaviour of a vehicle in free flight to the aerodynamic parameter estimation.

The determination of aerodynamic characteristics remains dependent of the quality and quantity of the data obtained experimentally. Therefore, the study choices are mainly guided by the experimental conditions and the available data. Chapter 1 described the experimental context from the design and conception of the two different model configurations, an Earth re-entry space vehicle and a fin-stabilized projectile, to the free flight tests. In terms of experimental conditions, only the initial Mach number and initial angle of attack can be defined. With the support of the skills at ISL, the expertise necessary for the experimental part is essential to obtain free flight data by means of different measurement techniques. In the present study, they are precisely the radar and three-axis magnetometer measurements, collected by using two different data acquisition approaches, depending on the studied vehicle.

The proposed identification procedure allows to define a guideline of the studies to manage. Chapter 2 presented the first step of the identification procedure that consists in the physical modelling. The behaviour of a vehicle in flight is expressed as a six degrees of freedom nonlinear state-space representation. The general model structure is obtained from flight mechanics laws. Our interest was mainly focused on the descriptions of the aerodynamic coefficients integrated in the model and adapted to each application. Some descriptions already exist in the literature and in order to keep a physical meaning of the parameters, polynomial descriptions as function of Mach numbers and total angles of attack were selected. However after multiple preliminary identification tests, we concluded that they do not reveal enough information of the aerodynamic coefficient evolution. With the purpose of keeping a physical meaning of the parameters, a modified aerodynamic coefficient model was suggested with coupled dependency in state variables and spline functions. In this sense, the model was constructed from a grey-box approach with the integration of parametrized functions describing the aerodynamic coefficients, where the parameters must be estimated from free flight data. The chosen model structure was implemented in the developed inverse 6DOF

code, where initial conditions of the state variables and parameters describing the aerodynamic coefficients can be estimated from free flight data.

The determination of aerodynamic parameters based on measured data is an inverse problem which can be impossible to solve if it is ill posed or difficult to solve if it is ill conditioned. That involves several identifiability tests of a unknown parameter set composed of the initial conditions and the model parameters, to ensure that they can be estimated from the chosen model structure and the available data. These studies correspond to the *a priori* and *a posteriori* identifiability analyses, respectively. They represent a major step of the identification procedure presented in Chapter 3. These analyses were performed for the space vehicle case and *a priori* identifiability concluded to a well-posed model structure. *A posteriori* identifiability analysis managed through sensitivity analysis allows to guide the parameter estimation, and mainly highlights the most relevant parameters which can be determined from free flight data. This task is not easy in the case of nonlinear models, where only local results can be obtained, hence the requirement of having a physical representation of the behaviour of a vehicle in free flight and *a priori* knowledge. Such information allows to know nonlinear functional relations between parameters, to impose initial guess of the parameters and interpret the obtain results. It was shown that using *a priori* knowledge of the system increases the number of identifiable initial conditions of the state variables. Concerning the *a posteriori* identifiability of the parameters describing the aerodynamic coefficients, it revealed that the number of identifiable parameters increases when several free flight tests are considered. This conclusion is coherent with the *a priori* knowledge, as free flight tests were managed for different initial experimental conditions in order to have distinct behaviours in flight, mainly in terms of total angle of attack evolution. Taking into account the identifiability results, the estimation was divided in two steps: the first one meant to determine essentially the state variable initial conditions for each test separately, while the second step proposed to estimate the aerodynamic coefficients through a multiple fit strategy. This approach, successfully applied to both applications, enabled to characterize the coefficients on a larger range of flight conditions.

Chapter 4 presented and discussed the main results of aerodynamic coefficient estimation based on single and/or multiple fit strategy, as well as the evolution of the output signals and the state variables. For the space probe case, the drag and pitch damping coefficients were described in a polynomial form as function of the Mach number and the total angle of attack. Guided by the identifiability analysis, the model parameters were estimated from a multiple fit strategy. For the projectile, the experimental conditions and available data are limited in terms of range of variation of the Mach number and the total angle of attack. Therefore, this makes it difficult to describe the aerodynamic coefficients in a polynomial form, analyze the identifiability and estimate the model parameters from multiple fit strategy. For this reason and as preliminary testing, only the drag coefficient was described as a function of the Mach number and the total angle of attack. The parameters were determined from a multiple fit strategy only in the supersonic flow regime. The other aerodynamic coefficients were estimated in a tabular form for constant Mach numbers and by considering each trial independently. For both applications, estimation results compare well with the results obtained previously for similar configurations. Moreover, simulated and measured output signals present a very good agreement after state variable initial conditions and aerodynamic coefficient estimation, that reinforces the employed procedure for the parameter identification and the ability of the model to reproduce the measured output signals. For projectiles, very good agreement is observed for results obtained from the different measurements techniques, namely the axial position and the pitch angle from radar data and on-board sensor technique, respectively, compared to high speed trajectory tracker system. This complementary measurement technique allows to validate our results by comparison with those obtained by image processing on 3D high speed videos. To justify the difference of behaviour in flight of these two

vehicles, a comparison between the Earth re-entry space vehicle and projectile was done, in terms of aerodynamic characteristics and their variable evolutions.

The different studies in the frame of this thesis mainly led to scientific contributions in the exterior ballistic domain through the development of an identification procedure. This allowed the implementation of a new inverse 6DOF code, Inv6DoF, to identify aerodynamic characteristics from free flight data, including:

- a model structure characterizing precisely the behaviour of a vehicle in free flight;
- a complete descriptions of the aerodynamic coefficients as a function of the Mach number and the total angle of attack, especially for the space probe where the drag and the pitch damping coefficients are described with coupled state variables and spline functions, respectively;
- the sensitivity functions to evaluate the parameter identifiability from single or multiple data series;
- an estimation code to determine the aerodynamic coefficients from a single or a multiple fit strategy.

Perspectives

In the continuity of the present investigations, future works can be suggested.

It could be useful to extend the works dealing with the identification procedure, so far only tested for two configurations. It could also be adapted to other architectures, such as gyro-stabilised projectiles.

An interesting area of study would be the analysis of the behaviour of a vehicle in flight in the transonic flow regimes, especially for the Basic Finner projectile. It is characterized by highly nonlinear aerodynamic coefficients that can exhibit special features in the range of Mach numbers between 0.8 and 1.2. Moreover, the assumption of negligible aerodynamic coefficients, for example the Magnus moment coefficient slope, is generally no longer valid in transonic regime and these coefficients should be integrated in the modelling step.

Concerning the measurement techniques, the use of accelerometers will enable to have access to information about the forces acting on the vehicle. In addition, the promising results obtained by image processing from 3D high speed video encourage us to continue our studies, especially in terms of lateral position and yaw angle determination.

The longer term objective of this work is to combine the identification techniques with control tools. In that respect, we are currently exploring several descriptions of the nonlinear dynamics system of a vehicle in flight such as a Linear Parameter Varying (LPV) model [Marcos (2001), Fujimori and Ljung (2006), Tóth (2010), Theodoulis et al. (2010)]. This choice of modelling is motivated by the fact that the use of LPV design techniques could ease the integration of LPV controller in the case of guided vehicle. Taking into account that the parameters have a physical interpretation, it would be interesting to use an LPV state-space representation.This would require the use of more complex identification method [Mercère (2012), Laroche et al. (2011), Wills and Ninness (2011), Verdult et al. (2004)] but several issues are still open.

Appendix A

Modelling - complementary information

This appendix provides basic background for transformation matrices from a frame to another, rotational kinematic equations development or vehicle attitude representations. These following details complete the modelling part, presented in Chapter 2.

A.1 Transformation matrices

The most common method to proceed to a transformation from a frame to another is the application of a sequence of attitude angle rotations. From Earth to body axes, the purpose is to bring O_{x_E,y_E,z_E} into coincidence with $O_{x,y,z}$. Attitude angles are a particular application of Euler angles, by considering rotations about each axis through ϕ, θ and ψ successively, as described in Figure A.1. This procedure is composed of the following steps [Cook (2012)]:

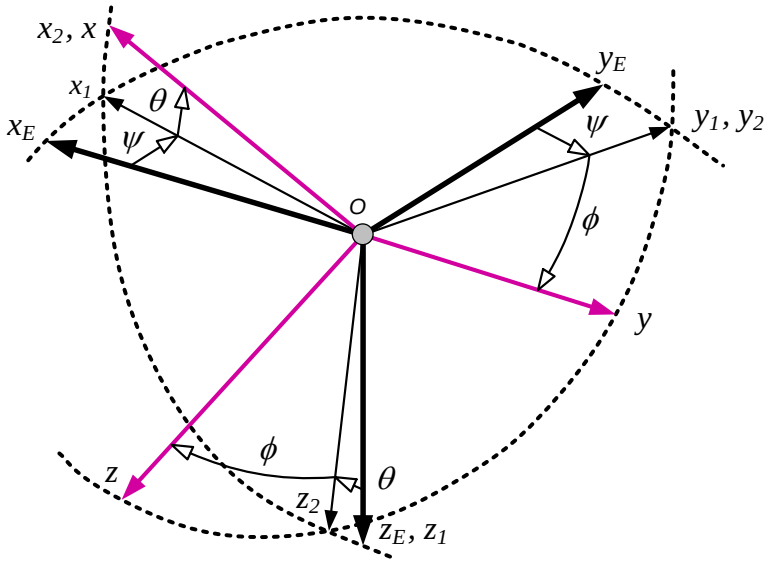

Figure A.1: Euler angles

The first movement is a roll angle rotation ϕ about O_x axis, as

$$\begin{aligned} O_x &= O_{x_2} \\ O_y &= O_{y_2}\cos\phi + O_{z_2}\sin\phi \\ O_z &= -\ O_{y_2}\sin\phi + O_{z_2}\cos\phi \end{aligned}$$

where O_{x_2,y_2,z_2} represents an intermediate frame. In a matrix form, these equations are written

$$\begin{bmatrix} O_x \\ O_y \\ O_z \end{bmatrix} = \begin{bmatrix} 1 & 0 & 0 \\ 0 & \cos\phi & \sin\phi \\ 0 & -\sin\phi & \cos\phi \end{bmatrix} \begin{bmatrix} O_{x_2} \\ O_{y_2} \\ O_{z_3} \end{bmatrix} \tag{A.1}$$

In the same way as previously, a pitch angle rotation θ about O_{y_2} axis is performed

$$\begin{bmatrix} O_{x_2} \\ O_{y_2} \\ O_{z_2} \end{bmatrix} = \begin{bmatrix} \cos\theta & 0 & -\sin\theta \\ 0 & 1 & 0 \\ \sin\theta & 0 & \cos\theta \end{bmatrix} \begin{bmatrix} O_{x_1} \\ O_{y_1} \\ O_{z_1} \end{bmatrix} \tag{A.2}$$

where O_{x_1,y_1,z_1} is a second intermediate frame.
The sequence is completed by a yaw angle rotation ψ about O_{z_1} axis

$$\begin{bmatrix} O_{x_1} \\ O_{y_1} \\ O_{z_1} \end{bmatrix} = \begin{bmatrix} \cos\psi & \sin\psi & 0 \\ -\sin\psi & \cos\psi & 0 \\ 0 & 0 & 1 \end{bmatrix} \begin{bmatrix} O_{x_E} \\ O_{y_E} \\ O_{z_E} \end{bmatrix} \tag{A.3}$$

By successive substitutions of equations (A.1), (A.2) and (A.3), the transformation from Earth to body axis components is given by

$$\begin{bmatrix} O_x \\ O_y \\ O_z \end{bmatrix} = \underbrace{\begin{bmatrix} 1 & 0 & 0 \\ 0 & \cos\phi & \sin\phi \\ 0 & -\sin\phi & \cos\phi \end{bmatrix}}_{\mathbf{R}_1(\phi)} \underbrace{\begin{bmatrix} \cos\theta & 0 & -\sin\theta \\ 0 & 1 & 0 \\ \sin\theta & 0 & \cos\theta \end{bmatrix}}_{\mathbf{R}_2(\theta)} \underbrace{\begin{bmatrix} \cos\psi & \sin\psi & 0 \\ -\sin\psi & \cos\psi & 0 \\ 0 & 0 & 1 \end{bmatrix}}_{\mathbf{R}_3(\psi)} \begin{bmatrix} O_{x_E} \\ O_{y_E} \\ O_{z_E} \end{bmatrix} \tag{A.4}$$

and can be noted

$$O_{x,y,z} = \mathbf{R}_1(\phi)\mathbf{R}_2(\theta)\mathbf{R}_3(\psi)O_{x_E,y_E,z_E} \tag{A.5}$$

The sequence $\mathbf{R}_1(\phi)\mathbf{R}_2(\theta)\mathbf{R}_3(\psi)$ is often used and is named a "3-2-1" sequence due to the order of the successive rotations.
A matrix $\mathbf{T}^{BE}$ is then defined to describe the transformation from Earth to body axes, parametrized by the attitude angles, and given by

$$\begin{aligned} \mathbf{T}^{BE}(\phi,\theta,\psi) &= \mathbf{R}_1(\phi)\mathbf{R}_2(\theta)\mathbf{R}_3(\psi) \\ &= \begin{bmatrix} \cos\theta\cos\psi & \cos\theta\sin\psi & -\sin\theta \\ \sin\phi\sin\theta\cos\psi - \cos\phi\sin\psi & \sin\phi\sin\theta\sin\psi + \cos\phi\cos\psi & \sin\phi\cos\theta \\ \cos\phi\sin\theta\cos\psi + \sin\phi\sin\psi & \cos\phi\sin\theta\sin\psi - \sin\phi\cos\psi & \cos\phi\cos\theta \end{bmatrix} \end{aligned} \tag{A.6}$$

By inverting the matrix in (A.6), the matrix transformation from body to Earth axes is obtained and is defined by

$$\mathbf{T}^{EB}(\phi,\theta,\psi) = \begin{bmatrix} \cos\theta\cos\psi & \sin\phi\sin\theta\cos\psi - \sin\psi\cos\phi & \cos\phi\sin\theta\cos\psi + \sin\phi\sin\psi \\ \cos\theta\sin\psi & \sin\phi\sin\theta\sin\psi + \cos\phi\cos\psi & \cos\phi\sin\theta\sin\psi - \sin\phi\cos\psi \\ -\sin\theta & \sin\phi\cos\theta & \cos\phi\cos\theta \end{bmatrix} \tag{A.7}$$

A.1.1 Gravity vector in body axes

The gravity acting along O_{z_E} is assumed constant in Earth axes. The gravity vector in Earth frame is then defined by

$$\begin{bmatrix} g_x \\ g_y \\ g_z \end{bmatrix}_E = \begin{bmatrix} 0 \\ 0 \\ g \end{bmatrix}_E \tag{A.8}$$

However, the components of the gravity vector in body axes are not considered constant anymore because it takes into account the vehicle orientation *w.r.t.* the Earth axes. By using the transformation matrix from Earth to body axes $\mathbf{T}^{BE}$ in (A.6), the gravity vector in body axes can be written as

$$\begin{bmatrix} g_x \\ g_y \\ g_z \end{bmatrix}_B = \mathbf{T}^{BE} \begin{bmatrix} 0 \\ 0 \\ g \end{bmatrix}_E = \begin{bmatrix} -g\sin\theta \\ g\sin\phi\cos\theta \\ g\cos\phi\cos\theta \end{bmatrix}_B \tag{A.9}$$

Consequently, the gravity force in body axes is

$$\mathbf{F}_G = m \begin{bmatrix} g_x \\ g_y \\ g_z \end{bmatrix}_B = m \begin{bmatrix} -g\sin\theta \\ g\sin\phi\cos\theta \\ g\cos\phi\cos\theta \end{bmatrix}_B \tag{A.10}$$

A.2 Rotational kinematic equations

The rotational kinematic equations relate the rate of change of the Euler angles to the body axis components of angular velocity. For easier understanding, extracted from [Hall (2003)], some notations are introduced. Let $\boldsymbol{\omega}_K^{I,J}$ be the angular velocity of the I frame *w.r.t.* the J frame expressed in the K frame, where I, J, K are equivalent to $B, 1, 2$ or E representing the body frame, both intermediate frames, defined in Appendix A.1, and the Earth frame, respectively.
The angular velocity can then be defined by considering the Euler angle sequence "3-2-1" in Appendix A.1 that lead to

$$\boldsymbol{\omega}_1^{1,E} = \boldsymbol{\omega}_E^{1,E} = [0 \;\; 0 \;\; \dot{\psi}]^T \tag{A.11a}$$

$$\boldsymbol{\omega}_2^{2,1} = \boldsymbol{\omega}_1^{2,1} = [0 \;\; \dot{\theta} \;\; 0]^T \tag{A.11b}$$

$$\boldsymbol{\omega}_B^{B,2} = \boldsymbol{\omega}_2^{B,2} = [\dot{\phi} \;\; 0 \;\; 0]^T \tag{A.11c}$$

The angular velocity of the body frame *w.r.t.* Earth frame is the sum of the angular velocity of the body frame *w.r.t.* the intermediate frame O_{x_2,y_2,z_2}, the angular velocity of O_{x_2,y_2,z_2} *w.r.t.* the second intermediate frame O_{x_1,y_1,z_1} and the angular velocity of O_{x_1,y_1,z_1} *w.r.t.* the Earth frame, noted by

$$\boldsymbol{\omega}^{B,E} = \boldsymbol{\omega}^{B,2} + \boldsymbol{\omega}^{2,1} + \boldsymbol{\omega}^{1,E} \tag{A.12}$$

However, all the vectors in (A.11) are defined in different frames. In order to apply the equation (A.12), all the vectors must be transformed to the same frame, in this case, the body frame.
For the equation (A.11c), the angular velocity is already expressed in the body frame. For equations (A.11a-A.11b), the transformation matrices defined in (A.4) are used to convert these vectors to the body frame. In this sense, they can be written

$$\boldsymbol{\omega}_B^{2,1} = \mathbf{T}^{B2}\boldsymbol{\omega}_2^{2,1} = \mathbf{R}_1(\phi)\boldsymbol{\omega}_2^{2,1} = \begin{bmatrix} 1 & 0 & 0 \\ 0 & \cos\phi & \sin\phi \\ 0 & -\sin\phi & \cos\phi \end{bmatrix} \begin{bmatrix} 0 \\ \dot{\theta} \\ 0 \end{bmatrix} \tag{A.13}$$

and

$$\boldsymbol{\omega}_B^{1,E} = \mathbf{T}^{B1}\boldsymbol{\omega}_1^{1,E} = \mathbf{R}_1(\phi)\mathbf{R}_2(\theta)\boldsymbol{\omega}_1^{1,E} = \begin{bmatrix} 1 & 0 & 0 \\ 0 & \cos\phi & \sin\phi \\ 0 & -\sin\phi & \cos\phi \end{bmatrix} \begin{bmatrix} \cos\theta & 0 & -\sin\theta \\ 0 & 1 & 0 \\ \sin\theta & 0 & \cos\theta \end{bmatrix} \begin{bmatrix} 0 \\ 0 \\ \dot{\psi} \end{bmatrix} \quad \text{(A.14)}$$

Consequently, the relation (A.12) can be developed as

$$\begin{bmatrix} \omega_x \\ \omega_y \\ \omega_z \end{bmatrix} = \begin{bmatrix} \dot{\phi} \\ 0 \\ 0 \end{bmatrix} + \begin{bmatrix} 1 & 0 & 0 \\ 0 & \cos\phi & \sin\phi \\ 0 & -\sin\phi & \cos\phi \end{bmatrix} \begin{bmatrix} 0 \\ \dot{\theta} \\ 0 \end{bmatrix} + \begin{bmatrix} 1 & 0 & 0 \\ 0 & \cos\phi & \sin\phi \\ 0 & -\sin\phi & \cos\phi \end{bmatrix} \begin{bmatrix} \cos\theta & 0 & -\sin\theta \\ 0 & 1 & 0 \\ \sin\theta & 0 & \cos\theta \end{bmatrix} \begin{bmatrix} 0 \\ 0 \\ \dot{\psi} \end{bmatrix}$$

which leads to

$$\begin{bmatrix} \omega_x \\ \omega_y \\ \omega_z \end{bmatrix} = \begin{bmatrix} 1 & 0 & -\sin\theta \\ 0 & \cos\phi & \sin\phi\cos\theta \\ 0 & -\sin\phi & \cos\phi\cos\theta \end{bmatrix} \begin{bmatrix} \dot{\phi} \\ \dot{\theta} \\ \dot{\psi} \end{bmatrix}$$

Inverting the last relationship gives differential equations for the Euler angles, which describe the rotational kinematics expressed in equations (2.22).

A.3 Attitude representations

Several approaches exist to characterize the attitude. Euler angles are often employed to represent the attitude of an object, due to their simplicity of use. Nevertheless, to overcome the problem of singularities of the solution arising from gimbal lock [Diebel (2006)], the rotational kinematic equations can also be expressed thanks to four quaternions instead of three Euler angles. The quaternions, also named Euler parameters, are related to Euler angles thanks to the relations

$$q_0 = \cos(\psi/2)\cdot\cos(\theta/2)\cdot\cos(\phi/2) + \sin(\psi/2)\cdot\sin(\theta/2)\cdot\sin(\phi/2) \quad \text{(A.15a)}$$

$$q_1 = \cos(\psi/2)\cdot\cos(\theta/2)\cdot\sin(\phi/2) - \sin(\psi/2)\cdot\sin(\theta/2)\cdot\cos(\phi/2) \quad \text{(A.15b)}$$

$$q_2 = \cos(\psi/2)\cdot\sin(\theta/2)\cdot\cos(\phi/2) + \sin(\psi/2)\cdot\cos(\theta/2)\cdot\sin(\phi/2) \quad \text{(A.15c)}$$

$$q_3 = \sin(\psi/2)\cdot\cos(\theta/2)\cdot\cos(\phi/2) - \cos(\psi/2)\cdot\sin(\theta/2)\cdot\sin(\phi/2) \quad \text{(A.15d)}$$

Appendix B

Static and dynamic stability

This appendix defines the static and dynamic stability in an aeroballistic sense in order to link these notions to the stability as defined in automatic control.

The static and dynamic stability are defined as follows:
Static stability refers to whether the initial tendency of the vehicle response to a perturbation is toward a restoration of equilibrium. For example, if the response to an infinitesimal increase in angle of attack α generates a pitching moment C_m that reduces the angle of attack, the configuration is said to be statically stable to such perturbations. Without static stability, a small perturbation from the trimmed (steady state) angle of attack would continue to increase in magnitude and could induce the tumbling of the vehicle [Strickland (2010)]. The static stability is associated to the pitch moment coefficient slope $C_{m\alpha} = \partial C_m/\partial\alpha$. This derivative describes the rate of change of the pitching moment coefficient with angle of attack and static stability is ensured with negative values of $C_{m\alpha}$.

Dynamic stability refers to whether the vehicle ultimately returns to the initial equilibrium state after some infinitesimal perturbations. Consideration of dynamic stability makes sense only for vehicles that are statically stable. But a vehicle can be statically stable and dynamically unstable (for example, if the initial tendency to return toward equilibrium leads to an overshoot, it is possible to have a oscillatory divergence of continuously increasing amplitude) [Caughey (2011)]. The dynamic stability is associated to the pitch damping coefficient $C_{mq} = \partial C_m/\partial(\frac{\omega_y d}{2V})$. This derivatives represents the rate of change of the pitching moment coefficient with angular velocity in pitch ω_y with constant angle of attack and dynamic stability is ensured with negative values of C_{mq}. More precisely, the pitch damping coefficient has been treated as the sum of two individual coefficients, C_{mq} and $C_{m\dot{\alpha}}$, that produce an aerodynamic moment proportional to the angular rate associated with the angle of attack. In fact, these two individual coefficients represent moments proportional to two different angular rates, $\dot{\alpha}$ and ω_y, that are associated with the angle of attack α and the the angular displacement of the longitudinal axis of the body *w.r.t.* the Earth-fixed axis system denoted by θ, respectively. For many nonmaneuvering flight trajectories, including those flown in ballistic aerodynamic ranges and for rectilinear flight path, the angular rates $\dot{\alpha}$ and ω_y are equal and the moment expansion can be simplified by combining the two damping coefficient into a single coefficient sum, which is proportional to a single angular rate [Weinacht (1998), McCoy (1999)].

To investigate the stability of a vehicle, the linearisation of the equations of motion allows to take advantage of linear stability criteria. Supposing the following linearized flight dynamic model

$\dot{x} = \mathbf{A}x$ obtained from equations (2.19b) and (2.21b), where $\mathbf{A}$ represents the stability matrix:

$$\begin{bmatrix} \dot{\alpha} \\ \dot{\omega}_y \end{bmatrix} = \underbrace{\begin{bmatrix} -F_\alpha & 1 \\ M_\alpha & M_q \end{bmatrix}}_{\mathbf{A}} \begin{bmatrix} \alpha \\ \omega_y \end{bmatrix} \tag{B.1}$$

where F_α is a function of the force coefficients dependent of the angle of attack α, M_α and M_q are functions of the aerodynamic coefficients $C_{m\alpha}$ and C_{mq}, respectively. In the present case, F_α is fixed to zero.

To define the stability for a linear automatic control system described by ordinary differential equations, it is necessary and sufficient that all the poles of the transfer function have negative real parts. Thus, it can be evaluated through the determination of the roots of the system's characteristic equation defined as:

$$det[s \cdot \mathbf{I}_2 - \mathbf{A}] = 0 \Rightarrow s^2 - M_q \cdot s - M_\alpha = 0 \tag{B.2}$$

where s are the pole locations (natural frequencies) of the system and $\mathbf{I}_2$ is the identity matrix of size 2. The stability is dependent of the sign of the root real part, directly relied to M_α and M_q values. The pole locations are conveniently parametrized in terms of the natural frequency ω_n and damping ratio ζ [Trumper and Dubowsky (2005)] [1]. Let us consider the characteristic equation

$$ms^2 + bs + k = 0 \tag{B.3}$$

with the assumption that m and k are greater than zero to maintain the system order. The natural frequency and the damping ratio are defined by

$$\omega_n = \frac{k}{m} \tag{B.4}$$

and

$$\zeta = \frac{b}{2\sqrt{km}} \tag{B.5}$$

The natural frequency ω_n is the frequency at which the system would oscillate if the damping b were zero. In this case, $k = -M_\alpha$, with $M_\alpha < 0$ to satisfy the previous made assumption. Then we suppose that the system is statically stable in an aeroballistic sense. However, to satisfy the stability of an automatic control system, both static and dynamic stability are required.

The damping ratio ζ is the ratio of the actual damping b to the critical damping $b_c = 2\sqrt{km}$. In this case, $b = -M_q$.

In terms of these parameters, the equation (B.2) takes the form

$$s^2 + 2\zeta\omega_n \cdot s + \omega_n^2 = 0 \tag{B.6}$$

Let us study the pole location possibilities:

- if $2\zeta\omega_n = 0 \Rightarrow M_q = 0$ (system dynamically unstable), it corresponds to $\zeta = 0$ and is referred to as the *undamped* case.

  The discriminant is equal to $4M_\alpha$. The system is statically stable if $M_\alpha < 0$ and the poles are equal to $s_{1,2} = \pm j\sqrt{|M_\alpha|}$ and contain no real part.

  Otherwise, if $M_\alpha > 0$, the system would be statically unstable and the poles $s_{1,2} = \pm\sqrt{M_\alpha}$ cannot have both negative real parts. Thus, the system is unstable.

1. The following explanations are extracted from [Trumper and Dubowsky (2005)].

- if the discriminant $4\zeta^2\omega_n^2 - 4\omega_n^2 = 4\omega_n^2(\zeta^2 - 1) < 0 \Rightarrow M_q^2 + 4M_\alpha < 0$, it corresponds to $0 < \zeta < 1$ and is referred to as the *underdamped* case. The system is statically stable and the poles are equal to

$$s_{1,2} = -\zeta\omega_n \pm (\omega_n\sqrt{1-\zeta^2})j \tag{B.7}$$
$$-v \pm \omega_d j \tag{B.8}$$

  where v is the attenuation and ω_d the damped natural frequency. The system is stable if $Re\{s_{1,2}\} < 0 \Rightarrow -v < 0 \Rightarrow M_q < 0$. This implies the dynamic stability of the system.

- if the discriminant $4\omega_n^2(\zeta^2 - 1) = 0 \Rightarrow M_q^2 + 4M_\alpha = 0$, it corresponds to $\zeta = 1$ and is referred to as the *critically damped* case. The system is statically stable and the double real pole is equal to

$$s_1 = -\zeta\omega_n = M_q/2 \tag{B.9}$$

  The system is stable if $Re\{s_1\} < 0 \Rightarrow M_q < 0$. This implies the dynamic stability of the system.

- if the discriminant $4\omega_n^2(\zeta^2 - 1) > 0 \Rightarrow M_q^2 + 4M_\alpha > 0$, it corresponds to $\zeta > 1$ and is referred to as the *overdamped* case. The poles are equal to

$$s_{1,2} = -(\zeta \pm \sqrt{\zeta^2 - 1})\omega_n = \frac{M_q \pm \sqrt{M_q^2 + 4M_\alpha}}{2} \tag{B.10}$$

  The system is stable if $Re\{s_{1,2}\} < 0 \Rightarrow s_{1,2} < 0$.

Appendix C

Sedoglavic algorithm

Sedoglavic has developed an algorithm for testing local observability, relied on the differential algebra and based on the existence of algebraic relations between state variables and successive derivations of the inputs and the outputs [Sedoglavic (2002)]. By considering that the parameters $\mathbf{p}$ *of the model are a special kind of state variables satisfying* $\dot{\mathbf{p}} = 0$*, the local theoretical identifiability problem is defined as a particular case of observability. It was implemented under the symbolic computation software MAPLE and can be downloaded on the personal page of Alexandre Sedoglavic* [1].
This appendix, extracted from Sedoglavic personal page, presents a brief description of this tool, as well as a simple example to illustrate the observability test to determine observable variables (observability) and model parameters (theoretical or a priori identifiability).

C.1 Algorithm description

Calling Sequence: `observabilityTest(F,X,G,Theta,U)`

where	F	-	a list of algebraic expressions representing a vector field
	X	-	a list of names such that `diff(X[i],t) = F[i]`
	G	-	a list of algebraic expressions representing outputs
	Theta	-	a list of the names of the parameters
	U	-	a list of the names of the inputs

This procedure returns a list composed of:

1. the dimension of the non observable variables and parameters;
2. the list of non observable variables and parameters;
3. the list of observable variables and parameters;
4. an integer representing the least number of row in the Jacobian matrix necessary to determine its kernel.

The model is of the following kind:

```
diff(Theta,t)  =   0            ,
diff(  X  ,t)  =   F(X,Theta,U) ,
       Y       =   G(X,Theta,U) .
```

where F and G are rational expressions.

1. Available at www.lifl.fr/∽sedoglav.

C.2 Example

```
> # Considered system is x'=x (a - b x) - c x, a'=b'=c'=0 and x is measured
> F := x*(a-b*x)-c*x ;
```

$$F := x\ (a - b\ x) - c\ x$$

```
> Y := x ;
```

$$Y := x$$

```
> infolevel[observabilityTest] := 1; % for printing details
```

$$infolevel_{observabilityTest} := 1$$

```
> observabilityTest([F],[x],[Y],[a,b,c],[]) ;
observabilityTest:  Modular computation with version 0.0
observabilityTest:  Some informations about the system
observabilityTest:  Nb Inputs U : 0
observabilityTest:  Nb Outputs Y : 1
observabilityTest:  Nb Variables X : 1
observabilityTest:  Nb Parameters Theta:  3
observabilityTest:  The computation are done modulo the following prime number
10000000000037
observabilityTest:  System treatment
observabilityTest:  End of system treatment .39e-1
observabilityTest:  Power series expansion at order 4
observabilityTest:  -> Order 2
observabilityTest:  -> Computation time .30e-1
observabilityTest:  -> Order 4
observabilityTest:  -> Computation time .49e-1
observabilityTest:  End of integration
observabilityTest:  Evaluation of output system
observabilityTest:  End of evaluation of output system
ObservabilityAnalysis:  The transcendence degree of k(U,Y) --> k(U,Y,X,Theta) is
1
ObservabilityAnalysis:  [a, c] are not observable.
ObservabilityAnalysis:  least number of equations needed to determine the group
of symetries 2
observabilityTest:  Total used time .109
```

```
[1, [a, c], [b, x], 2]
```

As listed in Section C.1, the outputs represent respectively the least number of row in the Jacobian matrix necessary to determine its kernel (equal to `1`), the non observable parameters and variables (the parameters `a` and `c` are *a priori* not identifiable knowing `x`), the observable parameters and variables (the parameter `b` is *a priori* identifiable and the variable `x` is observable) and the dimension of the non-observable parameters and variables (dim(`[a, c]`) equal to `2`).
In fact, the one-parameter group of translation

```
a -> a + lambda
c -> c + lambda
```

are composed of symmetries of the considered model letting its inputs and outputs invariant.

List of Figures

List of Tables

References

Albisser, M., Berner, C., Dobre, S., Thomassin, M., and Garnier, H. (2014). Aerodynamic coefficients identification procedure of a finned projectile using magnetometers and videos free flight data. In *28th ISB International Symposium on Ballistics, Atlanta, Georgia*.

Albisser, M., Dobre, S., Berner, C., Thomassin, M., and Garnier, H. (2013). Identifiability investigation of the aerodynamic coefficients from free flight tests. In *AIAA Atmospheric Flight Mechanics Conference, Boston, Massachusetts*.

Audoly, S., Bellu, G., D'Angio, L., Saccomani, M., and Cobelli, C. (2001). Global identifiability of nonlinear models of biological systems. *IEEE Transactions on Biomedical Engineering*, 48(1):55–65.

Banks, H., Cintrón-Arias, A., and Kappel, F. (2013). Parameter selection methods in inverse problem formulation. pages 43–73. Springer.

Banks, H., Dediu, S., and Ernstberger, S. (2007). Sensitivity functions and their uses in inverse problems. *Journal of Inverse and Ill-posed Problems*, 15(7):683–708.

Bastogne, T. (2008). *Modélisation Expérimentale des Systèmes Dynamiques-Applications en Biologie Systémique*. HDR, Université Henri Poincaré-Nancy I, France.

Belsley, D. A., Kuh, E., and Welsch, R. E. (2005). *Regression diagnostics: Identifying influential data and sources of collinearity*, volume 571. John Wiley & Sons.

Berner, C., Brinker, S., and Sommer, E. (2009). Exomars phase B1 - Extension ISL Open Range Free Flight Tests Final Report/ Phase 1 - Baseline Tests. Technical report, ISL FV-304/2009.

Berner, C., Dobre, S., Brinker, S., and Bernard, L. (2012). Exomars phase CD - ISL Open Range Free Flight Tests - Final Report/ Test Campaign 1. Technical report, ISL FV-315/2012.

Bhagwandin, V. and Sahu, J. (2013). Numerical prediction of dynamic stability derivatives for finned projectiles. In *27th International Symposium on Ballistics, Freiburg, Germany*.

Bieber, E., Adam, R., and Junod, E. (2014). CalibrateMagnetometer, a software for magnetometer calibration. Technical report, ISL-R 112/2014.

Bohlin, T. (2006). *Practical grey-box process identification. Theory and applications*. Springer-Verlag.

Brun, R., Kühni, M., Siegrist, H., Gujer, W., and Reichert, P. (2002). Practical identifiability of ASM2d parameters - systematic selection and tuning of parameter subsets. *Water Research*, 36(16):4113–4127.

Caughey, D. (2011). *Introduction to Aircraft Stability and Control*. Sibley School of Mechanical and Aerospace Engineering, Cornell University courses.

Chen, Y., Wen, C., Dou, H., and Sun, M. (1997). Iterative learning identification of aerodynamic drag curve from tracking radar measurements. *Control Engineering Practice*, 5(11):1543–1553.

Cook, M. V. (2012). *Flight dynamics principles: a linear systems approach to aircraft stability and control*. Butterworth-Heinemann.

de Divitiis, N. and Vitale, A. (2010). Fully structured aerodynamic model for parameter identification of a re-entry experimental vehicle. *Journal of Spacecraft and Rockets*, 47:113–124.

Defranoux, C. (2001). *Intégration de connaissances a priori pour l'estimation de paramètres physiques de modèles à temps continu*. PhD thesis, Université Henri Poincaré-Nancy I, France.

Diebel, J. (2006). Representing attitude: Euler angles, unit quaternions, and rotation vectors. *Citeseer, Matrix*.

Dobre, S. (2010). *Analyses de sensibilité et d'identifiabilité globales. Application à l'estimation de paramètres photophysiques en thérapie photodynamique*. PhD thesis, Université Henri Poincaré-Nancy I, France.

Dobre, S., Bastogne, T., Barberi-Heyob, M., Bechet, D., Didelon, J., and Richard, A. (2008). System identification of the intracellular photoreaction process induced by photodynamic therapy. In *16th Mediterranean Conference on Control and Automation, Ajaccio, France*.

Dobre, S., Berner, C., Albisser, M., Saada, F., Clopeau, E., Ferracina, L., and Marraffa, L. (2015). MarcoPolo-R ERC dynamic stability characterization. Open Range Free Flight Tests. In *8th European Symposium on Aerothermodynamics for Space Vehicles, Lisbon, Portugal*.

Dochain, D., Vanrolleghem, P., and Van Daele, M. (1995). Structural identifiability of biokinetic models of activated sludge respiration. *Water Research*, 29(11):2571–2578.

Dorrzapft, J. (2010). La balistique des projectiles. Analyse - Aspects théoriques et pratiques. In *3ème Congrès de Balistisque Lésionnelle, Ecully, France*.

Dunn, A. (1989). *Aeropredictive methods for missile analysis*. PhD thesis, Naval postgraduate school, Monterey, California.

Dupuis, A. (2002). Aeroballistic range and wind tunnel tests of the Basic Finner reference projectile from subsonic to high supersonic velocities. Technical report, Defence Research Establishment, Valcartier, Quebec.

Dupuis, A. and Hathaway, W. (1997). Aeroballistic range tests of the Basic Finner reference projectile at supersonic velocities. Technical report, Defence Research Establishment, Valcartier, Quebec.

Dutta, G., Singhal, A., Kushari, A., and Ghosh, A. (2008). Estimation of drag coefficient from radar-tracked flight data of a cargo shell. *Defence Science Journal*, 58(3):377–389.

Fleck, V. (1998). *Introduction à la balistique extérieure*. Institut Franco-Allemand de Recherche de Saint-Louis, France.

Fleck, V. (2000). Determination of the angular motion and of the aerodynamic aerodynamic coefficients from 3D magnetic sensor signal. In *Proceedings of European Forum on Ballistics of projectiles*, Saint-Louis, France.

Franceschini, G. and Macchietto, S. (2008). Model-based design of experiments for parameter precision: State of the art. *Chemical Engineering Science*, 63(19):4846–4872.

Fujimori, A. and Ljung, L. (2006). Model identification of linear parameter varying aircraft systems. *Proceedings of the Institution of Mechanical Engineers, Part G: Journal of Aerospace Engineering*, 220(4):337–346.

Gülhan, A., Klevanski, J., and Willems, S. (2011). Experimental study of the dynamic stability of the Exomars capsule. In *7th European Symposium on Aerothermodynamics, ESA Special Publication, Brugge, Belgium.*

Hadamard, J. (1902). *Sur les problèmes aux dérivées partielles et leur signification physique*, volume 13. Princeton University Bulletin.

Hall, C. (2003). *Spacecraft Attitude Dynamics and Control.* Virginia Tech, Aerospace and Ocean Engineering courses.

Hathaway, W. (1976). *Analysis of the free flight aerodynamics on non-symmetric bodies from ballistic spark range data.* PhD thesis, The faculty of the Graduate College of the University of Vermont.

Jategaonkar, R. (2006). *Flight vehicle system identification: a time domain methodology.* American Institute of Aeronautics and Astronautics.

Klein, V. and Morelli, E. (2006). *Aircraft system identification: theory and practice.* American Institute of Aeronautics and Astronautics.

Laroche, E., Mercere, G., and Halalchi, H. (2011). Modélisation et identification LPV d'un manipulateur flexible. In *Journées identification et modélisation expérimentale. Douai, France.*

Leith, D., Murray-Smith, D., and Bradley, R. (1993). Combination of data sets for system identification. In *IEEE Proceedings D (Control Theory and Applications)*, volume 140, pages 11–18.

Li, R., Henson, M., and Kurtz, M. (2004). Selection of model parameters for off-line parameter estimation. *IEEE Transactions on Control Systems Technology journal*, 12(3):402–412.

Lieske, R. and al. (August 1972). Determination of aerodynamic drag from radar data. *Ballistic Research Laboratories Report.*

Ljung, L. and Glad, T. (1994). On global identifiability for arbitrary model parametrizations. *Automatica*, 30(2):265–276.

Marcos, A. (2001). *A linear parameter varying model of the Boeing 747-100/200 longitudinal motion.* PhD thesis, University of Minnesota, USA.

McCoy, R. (1999). *Modern exterior ballistics: the launch and flight dynamics of symmetric projectiles.* Schiffer.

Mercère, G. (2012). *Identification of Multi-Input Multi-Output State-Space Systems: from Linear Time-Invariant Models to Linear Parameter-Varying Ones*. HDR, Poitiers University.

Murman, S. M. and Aftosmis, M. J. (2007). Dynamic analysis of atmospheric-entry probes and capsules. In *45th AIAA Aerospace Sciences Meeting, Reno, NV*, number AIAA No. 2007-0074.

Murphy, C. (1954). Data reduction for the free flight spark ranges. Technical report, Ballistic Research Laboratories.

Murphy, C. (1963). Free flight motion of symmetric missiles. Technical report, Ballistic Research Laboratories.

Oussar, Y. and Dreyfus, G. (2001). How to be a gray box: dynamic semi-physical modeling. *Neural networks*, 14(9):1161–1172.

Peeters, R. and Hanzon, B. (2005). Identifiability of homogeneous systems using the state isomorphism approach. *Automatica*, 41:513–529.

Perasso, A. (2009). *Identifiabilité de paramètres pour des systèmes décrits par des équations aux dérivées partielles. Application à la dynamique des populations*. PhD thesis, Université Paris-Sud XI, France.

Portier, S. (2014). 3D position and attitude determination of a vehicle in free flight based on 3D high-speed videos. Internship report, French-German Research Institute of Saint-Louis, France.

Saccomani, M. P., Audoly, S., and D'Angio, L. (2003). Parameter identifiability of nonlinear systems: the role of initial conditions. *Automatica*, 39:619–632.

Sammonds, R. (1970). Transonic static and dynamic stability characteristics of two large angle spherically blunted high drag cones. In *AIAA Atmospheric Flight Mechanics Conference, Tullahoma, TN*.

Schoenenberger, M., Hathaway, W., Yates, L., and Desai, P. (2005). Ballistic range testing of the Mars exploration rover entry capsule. In *43rd AIAA Aerospace Sciences Meeting and Exhibit, Reno, NV*, number AIAA No. 2005-0055.

Schoenenberger, M., Yates, L., and Hathaway, W. (2009). Dynamic stability testing of the Mars science laboratory entry capsule. In *41st AIAA Thermophysics Conference, San Antonio, TX*.

Sedoglavic, A. (2002). A probabilistic algorithm to test local algebraic observability in polynomial time. *Journal of Symbolic Computation*, 33(5):735–755.

Shantz, L. and Groves, R. (1960). Dynamic and static stability measurements of the Basic Finner at supersonic speeds. Technical report, U.S. Naval Ordnance Laboratory, Maryland.

Sjöberg, J., Zhang, Q., Ljung, L., Beneviste, A., Delyon, B., Glorennec, P., Hjalmarsson, H., and Juditsky, A. (1995). Nonlinear black-box modelling in system identification: a unified overview. *Automatica*, 31:1691–1724.

Stengel, R. (2004). *Flight dynamics*. Princeton University Press.

Strickland, J. (2010). *Missile Flight Simulation: Surface-to-Air Missiles*. Lulu, Inc.

Theodoulis, S., Gassmann, V., Brunner, T., and Wernert, P. (2013). Robust bank-to-turn autopilot design for a class of 155mm spin-stabilized canard-guided projectiles. In *AIAA Atmospheric Flight Mechanics Conference, Boston, Massachusetts*.

Theodoulis, S., Morel, Y., Wernert, P., and Tzes, A. (2010). LPV modeling of guided projectiles for terminal guidance. In *18th IEEE Mediterranean Conference on Control and Automation, Marrakech, Morocco*.

Thomassin, M. (2005). *Estimation de retard dans des conditions expérimentales passives: Application à l'identification de bief de rivière*. PhD thesis, Université Henri Poincaré-Nancy I, France.

Titterton, D. (2004). *Strapdown inertial navigation technology*, volume 17. Institution of Engineering and Technology.

Tóth, R. (2010). *Modeling and identification of linear parameter-varying systems*, volume 403. Springer Verlag.

Trumper, D. and Dubowsky, S. (2005). *Modeling Dynamics and Control I*. Massachusetts Institute of Technology, MIT courses.

Vanrolleghem, P., Daele, M., and Dochain, D. (1995). Practical identifiability of a biokinetic model of activated sludge respiration. *Water Research*, 29(11):2561–2570.

Verdult, V., Lovera, M., and Verhaegen, M. (2004). Identification of linear parameter-varying state-space models with application to helicopter rotor dynamics. *Taylor & Francis, International Journal of Control*, 77(13):1149–1159.

Vitale, A. and Corraro, F. (2012). Identification from flight data of the Italian unmanned space vehicle. In *16th IFAC Symposium on System Identification, Brussels, Belgium*.

Walter, E. and Pronzato, L. (1997). *Identification of parametric models from experimental data*. Springer-Verlag.

Weijers, S. and Vanrolleghem, P. (1997). A procedure for selecting best identifiable parameters in calibrating activated sludge model no.1 to full-scale plant data. *Water Science and Technology*, 36(5):69–79.

Weinacht, P. (1998). Navier-stokes predictions of the individual components of the pitch-damping sum. *Journal of spacecraft and rockets*, 35(5):598–605.

Wey, P. (2014). Compte rendu d'avancement du projet BALCO. Technical report, ISL-CR/RV 485/2010.

Wills, A. and Ninness, B. (2011). System identification of linear parameter varying state-space models. *Linear Parameter-Varying System Identification: New Developments and Trends, World Scientific Publishing, Singapore*, pages 295–313.

Winchenbach, G. (1997). Aerodynamic testing in a free-flight spark range. Technical report, Wright Laboratory.

Winchenbach, G., Chapman, G., Hathaway, W., Ramsey, A., and Berner, C. (2002). Dynamic stability of blunt atmospheric entry configurations. *Journal of spacecraft and rockets*, 39(1):49–55.

Winchenbach, G., Krieger, J., Hathaway, W. H., and Whyte, R. (1998). EFP Free Flight Test Aerodynamic Results. Technical report, Arrow Tech.

Worden, K., Wong, C., Parlitz, U., Hornstein, A., Engster, D., Tjahjowidodo, T., Al-Bender, F., Rizos, D., and Fassois, S. (2007). Identification of pre-sliding and sliding friction dynamics: grey-box and black-box models. *Mechanical Systems and Signal Processing*, (21):514–534.

Yao, K., Shaw, B., Kou, B., McAuley, K., and Bacon, D. (2003). Modeling ethylene/butene copolymerization with multi-site catalysts: parameter estimability and experimental design. *Taylor & Francis, Polymer Reaction Engineering*, 11(3):563–588.

Zipfel, P. (2000). *Modeling and simulation of aerospace vehicle dynamics.* American Institute of Aeronautics and Astronautics.

L'utilisation des coefficients aérodynamiques pour caractériser le comportement d'un objet en vol libre demeure un sujet de recherche parmi les plus complexes et les plus étudiés dans le domaine de la balistique extérieure. Actuellement, plusieurs méthodes expérimentales ou théoriques permettent de quantifier les coefficients aérodynamiques d'objets. La présente étude analyse l'identification des coefficients aérodynamiques à partir de données obtenues lors d'essais en vol libre.
La détermination des coefficients aérodynamiques basée sur des mesures de vol libre et des techniques d'identification de systèmes demeure une tâche complexe et ambitieuse pour des objets en vol tels que des corps de rentrée dans l'atmosphère, des drones ou des munitions. Ceci est principalement causé par la structure non linéaire du modèle mathématique décrivant le comportement de l'objet en vol, l'absence de signal d'entrée, les conditions initiales des variables d'état inconnues et la dépendance non linéaire des coefficients aérodynamiques en plusieurs variables d'état. Dans ces conditions, l'estimation de paramètres doit être menée avec rigueur. Cette étude vise à modéliser, définir ainsi que maîtriser les techniques d'identification de paramètres les plus adaptées au problème qu'est la détermination des coefficients aérodynamiques.
Le travail de thèse a été dédié au développement d'une procédure d'identification pour la détermination des coefficients aérodynamiques à partir de mesures de vol libre et a été testée pour deux cas d'application : un corps de rentrée dans l'atmosphère et un projectile stabilisé par empennage. Cette procédure nécessite plusieurs étapes telles que la description du comportement d'un objet en vol libre sous la forme d'un modèle non linéaire en représentation d'état, la description polynomiale des coefficients aérodynamiques en fonction du nombre de Mach et de l'incidence, les analyses d'identifiabilité *a priori* et *a posteriori* suivies de l'estimation des paramètres. De plus, dans le but d'augmenter la probabilité que les coefficients caractérisent l'aérodynamique de l'objet pour l'ensemble des conditions d'essais et d'améliorer la précision des coefficients estimés, une stratégie "multiple fit" a été appliquée. Cette approche fournit une base de données de coefficients aérodynamiques, qui sont déterminés à partir de plusieurs séries de mesures analysées simultanément, afin de décrire le spectre le plus complet du mouvement de l'objet.

Mots-clés : Coefficients aérodynamiques, données de vol libre, modèle non linéaire, identification, identifiabilité, stratégie "multiple fit"

The use of aerodynamic coefficients for the characterization of the behaviour of an object in flight remains one of the oldest and most emergent research project in the field of exterior ballistic. Currently, there exist several methods able to quantify the aerodynamic coefficients of vehicles. The present study investigates the identification of the aerodynamic coefficients based on measured data, gathered during free flight tests from different measurement techniques.
The determination of the aerodynamic coefficients from free flight measurements and system identification techniques remains a complex and challenging task for vehicles in flight like Earth re-entry space vehicles, Unmanned Aerial Vehicles or ammunition. This is mainly due to the nonlinear structure of the mathematical model describing the behaviour of the vehicle in flight, the absence of an input signal, the unknown initial conditions of the state variables and the nonlinear dependence of the aerodynamic coefficients on several state variables. In these conditions, the parameter estimation stage must be processed with caution. This project deals with topics as modelling, defining and mastering parameter identification techniques best suited to the problem of the aerodynamic coefficients determination.
In the frame of this study, an identification procedure was developed for the aerodynamic coefficients determination based on free flight measurements and was tested for two application cases: a re-entry space vehicle and a fin stabilized reference projectile. This procedure requires several steps such as the description of the behaviour of the vehicle in free flight as a nonlinear state-space model representation, the polynomial descriptions of the aerodynamic coefficients as function of Mach number and incidence, the *a priori* and *a posteriori* identifiability analyses, followed by the estimation of the parameters from free flight measurements. Moreover, to increase the probability that the coefficients define the vehicle's aerodynamics over the entire range of test conditions and to improve the accuracy of the estimated coefficients, a multiple fit strategy was considered. This approach provides a common set of aerodynamic coefficients that are determined from multiple data series simultaneously analyzed, and gives a more complete spectrum of the vehicle's motion.

Keywords: Aerodynamic coefficients, free flight data, nonlinear model, identification, identifiability, multiple fit strategy